LOW REYNOLDS NUMBER SETTLING OF CYLINDRICAL RODS WITH VARIOUS GEOMETRIES IN A QUIESCENT FLUID

AMIRHOSSEIN HAMIDI

A DISSERTATION SUBMITTED TO THE FACULTY OF GRADUATE STUDIES
IN PARTIAL FULFILMENT OF THE REQUIREMENTS
FOR THE DEGREE OF
DOCTOR OF PHILOSOPHY

GRADUATE PROGRAM IN MECHANICAL ENGINEERING
YORK UNIVERSITY
TORONTO, ONTARIO

JUNE 2025

Abstract

This dissertation is motivated by the atmospheric transport of microplastic fibres, a growing environmental concern. The atmosphere is recognized as a major pathway for the long-range transport of microfibres. However, many atmospheric simulations simplify fibre geometry, often representing them as volume-equivalent spheres or straight cylinders, despite the more complex shapes observed in microfibre samples from atmospheric deposits. This research aims to enhance our understanding of the settling behavior of curved, V-shaped, U-shaped, and S-shaped cylindrical rods within the Reynolds number and aspect ratio range associated with the atmospheric transport of microfibres.

A series of experiments were conducted using millimeter-scale metal rods with aspect ratios ranging from 10 to 120, settling in a quiescent water-glycerin chamber to replicate Reynolds numbers below 7. A stereo-PTV system was employed, with two side cameras tracking terminal settling velocities and orientations, while a bottom camera captured potential spinning motions. Using a three-dimensional calibration algorithm, the terminal velocities and orientations of the rods were determined in real-life space.

Results demonstrate that curved and V-shaped rods settle faster than straight rods of the same dimensions, with V-shaped rods settling only slightly faster than curved rods of equivalent projected length. U-shaped rods exhibit a transition in orientation from vertical to oblique above a critical Reynolds number or below a critical middle arm length ratio. They consistently settle faster than straight rods because of their non-zero inclination angle. Furthermore, their terminal velocity either peaks at a specific aspect ratio or remains constant due to a trade-off between side arm length and rod inclination. S-shaped rods exhibit spinning motions at a constant rate while settling at the same velocity as the straight rods of identical dimensions. Their spinning rate peaks at an intermediate middle arm length ratio, which was experimentally and theoretically investigated. New models were developed to estimate the terminal velocity of rods with these geometries, which can also be applied to predict the terminal velocity and the horizontal travel distance of microfibres of various shapes. This study highlights the crucial role of fibre morphology in determining vertical terminal velocity and, consequently, horizontal dispersion in the atmosphere.

Acknowledgements

I am sincerely grateful to Professor Hanson, my supervisor, for his invaluable guidance and support throughout this research. I also thank Professor Gordon, my co-supervisor, for his insightful feedback and encouragement. My thanks extend to Professors Rezai and Chen, the members of my examination committee, for their time, thoughtful comments, and suggestions. Lastly, I deeply appreciate my family and friends for their unwavering love and support during this journey.

Table of Contents

List of Tables

List of Figures

List of Symbols

Symbol	Description
F_B	buoyancy force
F_D	drag force
F_G	gravitational force
ρ_f	fluid density
μ_f	fluid dynamic viscosity
ν_f	fluid kinematic viscosity
ρ_P	particle density
V_P	particle volume
A_P	projected area
ρ'	particle-to-fluid density ratio
g	gravitational acceleration
Re	Reynolds number
C_D	drag coefficient
V_S	total terminal velocity
V_V	vertical component of terminal velocity
V_H	horizontal component of terminal velocity
V_∞	terminal velocity in unbounded medium
V_T	tip velocity of S-shaped rod
D_C	rod diameter
L_C	rod length
AR	rod aspect ratio
L_P	rod projected length
β	projected length-to-total length ratio
D_{eq}	volume-equivalent diameter
D_a	aerodynamic diameter
L_1	side arm length of U- and S-shaped rod
L_2	middle arm length of U- and S-shaped rod
ROC	curvature radius of curved rod
θ_0	central angle of curved rod
α_0	bend angle of V-shaped rod
α	middle arm length ratio of U- and S-shaped rod

Symbol	Description
γ	orientation angle of S-shaped rod
K_1	Stokes' shape factor
K_2	Newton's shape factor
ϕ	sphericity
S	projected area ratio of volume-equivalent sphere to particle
f	particle flatness
e	particle elongation
θ	inclination angle
$\bar{\zeta}$	mean inclination angle of curved rod
α_0'	mean inclination angle of V-shaped rod
λ	flow angle for U-shaped rod
γ'	Euler's constant
β_E	elasto-gravitational number
Ga	Galilei number
C	curvature index
F	element of the calibration mapping matrix
ΔX, ΔZ	horizontal pixel displacement
Δx, Δz	horizontal millimeter displacement
ΔY	vertical pixel displacement
Δy	vertical millimeter displacement
T	temperature
σ_R	uncertainty of dependent variable
R^2	coefficient of determination
ω	spinning rate of S-shaped rod
T_{Total}	total torque

Chapter 1

Introduction

Microplastics (MPs) are plastic particles smaller than five millimeters. They can be intentionally manufactured within this size range, such as nurdles used in plastic production and microbeads found in personal care products [1–3]. These are known as primary MPs. In contrast, secondary MPs form when larger plastic debris breaks down into smaller fragments due to weathering effects and mechanical abrasion [2, 4, 5]. The environmental transport of MPs has raised widespread concerns [6–8]. Marine and atmospheric pathways are two key routes through which MPs travel [9, 10]. They move from land to sea via rivers and return to land through storms, tides, and flooding. Additionally, MPs can become airborne, highlighting a complex and interconnected transport cycle [1, 3, 11].

The atmosphere has a pivotal role in the long-range transport of MPs. MP samples have been collected from atmospheric depositions in various regions of the world, ranging from major population centers, such as London, UK [12], and Kuala Nerus and Bangi, Malaysia [13], to highly remote mountainous areas, such as the French Pyrenees [14], and Arctic snow [15]. Evangeliou *et al.* [16] simulated the atmospheric transport of MPs originating from tire and brake wear particles and found that these particles exhibit a high transport efficiency to remote areas. The Arctic is one of the remote destinations for MP depositions. Zhang *et al.* [17] provided an overview of the distribution of MPs in Arctic environments, including Arctic snow, sea ice, seawater, rivers, and sediments. This information is utilized to identify

potential sources, transport routes, and patterns of storage and release. They discovered that the long-range transport of MPs from terrestrial sources through the atmosphere plays a significant role in their deposition in Arctic snow, sea ice, and the surface waters of the ocean.

Microplastics (MPs) found in atmospheric deposition exhibit a range of geometries, including fibres, fragments, spheres, films, and foams [3, 18]. Numerous studies report that fibres are the most abundant type of MPs recovered from atmospheric samples [11, 12, 19–25]. While atmospheric transport of MPs has been modeled in several studies [12, 16, 26, 27], many have simplified the geometry by assuming spherical shapes [14, 16] or used generalized models [12, 27, 28] to estimate key parameters such as terminal velocity. However, Ward *et al.* [29] showed that treating microfibres larger than 6 μm as equivalent spheres can significantly underestimate their transport range. Similarly, Xiao *et al.* [30] demonstrated substantial differences in terminal velocity between fibres and their spherical equivalents. To better capture the effects of fibre geometry on settling, Tatsii *et al.* [28] used the generalized model developed by Bagheri and Bonadonna [31], which accounts for both regular and irregular particle shapes, the particle-to-fluid density ratio, and the maximum projected area during settling. Microfibres collected from atmospheric deposition exhibit diverse morphologies beyond simply straight and have included curved, V-shaped, U-shaped, and S-shaped features, or combinations of these curves and bends resulting in other complex shapes (see for example the images of [15, 30, 32–34]). Despite this morphological diversity, only a limited number of studies have investigated the influence of non-straight geometries on fibre settling, with most focusing exclusively on curved fibres [35–37].

A significant gap remains concerning the settling dynamics of individual microplastic fibres necessary to predict their atmospheric transport. Existing aerodynamic models for non-spherical particle settling are often insufficiently accurate for fibres or are restricted to specific aspect ratios and Reynolds number ranges [38–42]. Furthermore, the influence of fibre morphology, including bends and curvature, on settling behaviour remains largely unexplored, further complicating efforts to develop comprehensive predictive models. In this study, an

experimental investigation is conducted using metal rods falling in a chamber filled with a quiescent highly viscous water-glycerin mixture. These experiments replicate a range of low Reynolds numbers associated with the atmospheric settling of microplastic fibres, within the Stokes regime, while enabling detailed analysis of rod orientation, trajectory, and velocity, and minimizing uncertainties related to geometry and materials. A set of idealized fibre geometries is considered in this research, which includes (a) straight, (b) curved, (c) V-shaped, (d) U-shaped, and (e) S-shaped rods, representing common geometries or features of the shapes of microplastic fibres observed from atmospheric deposition studies. In addition to the transport of microplastics, the settling of cylindrical fibres or rods at low Reynolds numbers is also crucial in various industrial and biomedical processes, including paper manufacturing [36, 43, 44], fibre-reinforced composites [45, 46], tissue engineering [47], and drug delivery [48]. The core objectives of the present dissertation are summarized below.

1. Characterize the aerodynamic behavior of individual rods with complex geometries in quiescent fluid within the Stokes regime, focusing on terminal velocity, orientation, and rotational dynamics, while accounting for the influence of morphology on their settling patterns.

2. Expand and refine (semi-)empirical models to determine the terminal velocities of the rods with complex geometries under quiescent conditions.

3. Assess the influence of fibre morphology on aerodynamic characteristics and its potential impact on long-range transport.

The structure of the present thesis is as follows. In Chapter 2, a summary of the literature review and previous work in this field is provided. Chapter 3 outlines the experimental setup and the analysis methods utilized. Chapter 4 presents the results of V-shaped rods settling in a quiescent water-glycerin mixture, compares them with curved rods of the same dimensions and projected area, and introduces a new model for predicting the terminal velocity of straight, curved, and V-shaped rods. In Chapters 5 and 6, the low Reynolds number settling

of U-shaped and S-shaped rods is discussed, respectively, with new models developed to estimate the terminal velocity of U-shaped rods and the spinning rate of S-shaped rods. Finally, the main conclusions of this thesis and recommendations for future work in this field are included in Chapter 7.

Note that part of the data for straight and curved rods were obtained by Daramsing [49] and can be found in his M.A.Sc. thesis. As part of this Ph.D. research, additional cases of straight and curved rods were included to extend the range of Reynolds numbers for both geometries, as well as the range of the curvature index for curved rods. Part of Chapter 4, on the settling of straight and curved rods (Section 4.4.1), as well as Chapter 5, on the settling of U-shaped rods, have already been published in two different journal papers [50, 51]. Furthermore, a comparison of the terminal velocities of rods with various geometries studied in this research has also been published [52]. Detailed results on the settling of V-shaped rods and their comparison with curved rods (Chapter 4), as well as the results of S-shaped rods (Chapter 6), have been discussed in two other journal manuscripts, which are at various stages in the peer-review process at the time of submission of this dissertation.

Chapter 2

Background

In this chapter, a comprehensive review of the literature regarding microplastic particles, the main motivation for this research, and the settling behavior of spherical and non-spherical particles is provided. The transport of microplastics in the environment, as well as their shapes, dimensions, and properties, is discussed. In addition to microplastic transport, the role of fibre settling at low Reynolds numbers in various industrial and biomedical processes is also briefly discussed. A detailed understanding of particle settling dynamics is required to improve the modeling and prediction of microplastic transport. Therefore, the settling behavior of spherical and non-spherical particles, along with the models used to predict their settling, is reviewed. Finally, past studies on the settling of straight, curved, and bent cylindrical rods and fibres, the impact of asymmetry in rod geometry on settling, and the effects of rotation on rod settling are reviewed and discussed.

2.1 Microplastics Review

Microplastics (MPs) are a subset of plastic particles that are smaller than 5 mm. MPs intentionally manufactured to be smaller than 5 mm are classified as primary MPs [2, 53]. This type of MP is used in the production of other plastic products and healthcare items [1, 3]. However, secondary MPs are formed by the degradation of primary MPs in the environment due to weathering effects [4, 5, 54]. Among all these sources, one of the primary contributors

to environmental MPs is vehicle tire wear, which is driven by the rapid worldwide rise in vehicle numbers [55]. According to the results of Brahney *et al.* [56], MPs originating from tire and brake emissions account for 84% of the total MPs released into the atmosphere in the Western United States, followed by ocean emissions (11%) and agricultural soil dust (5%) [57]. The microfibres coming from synthetic textiles during laundering are another major source of MPs released into the environment [20, 58, 59]. The study by Acharya *et al.* [58] underscores the role of wastewater treatment plants in reducing microfibre release, while also addressing the challenges associated with the rise in synthetic textile use and the need for standardized research methods to better understand and tackle this escalating environmental concern. The risks that MPs present to both human health and ecosystems highlight the importance of investigating their transport and fate. For example, inhalation of MP, particularly those mixed with compounds like monomers, various chemicals, dyes, and additives, can result in respiratory diseases [60–62]. The presence of MPs in Arctic glaciers can lower surface reflectivity (albedo), which accelerates ice melting and disrupts climate patterns [63, 64]. Furthermore, MPs can impact the carbon cycle in the environment by creating new niches for aquatic microorganisms as they undergo physical degradation [65]. MPs may also influence greenhouse gas emissions from fertilized soils [66]. During ice and snow melt, organic carbon stored in glaciers can be released, affecting carbon fluxes in both terrestrial and aquatic ecosystems [67]. The following subsections discuss the transport of MPs in the atmosphere and their characteristics.

2.1.1 Transport of Microplastics in the Atmosphere

The borderless and global distribution of MPs has raised widespread concerns [6–8]. MPs are distributed globally by marine and atmospheric pathways [9, 10]. The transport of MPs can also be described as an interconnected cycle [1, 3, 11]. They transition from land to sea through rivers and return to land through storms, tides, and flooding events. They can ultimately be released into the air. The atmosphere has a pivotal role in the long-range

transport of MPs. Figure 2.1 provides an overview of the atmospheric transport of MPs. According to this figure, MPs are dispersed into the atmosphere from local emission sources and travel long distances through a series of surrounding air systems. They return to the marine environments through both dry and wet deposition and can be released back into the atmosphere through water evaporation and wind [11].

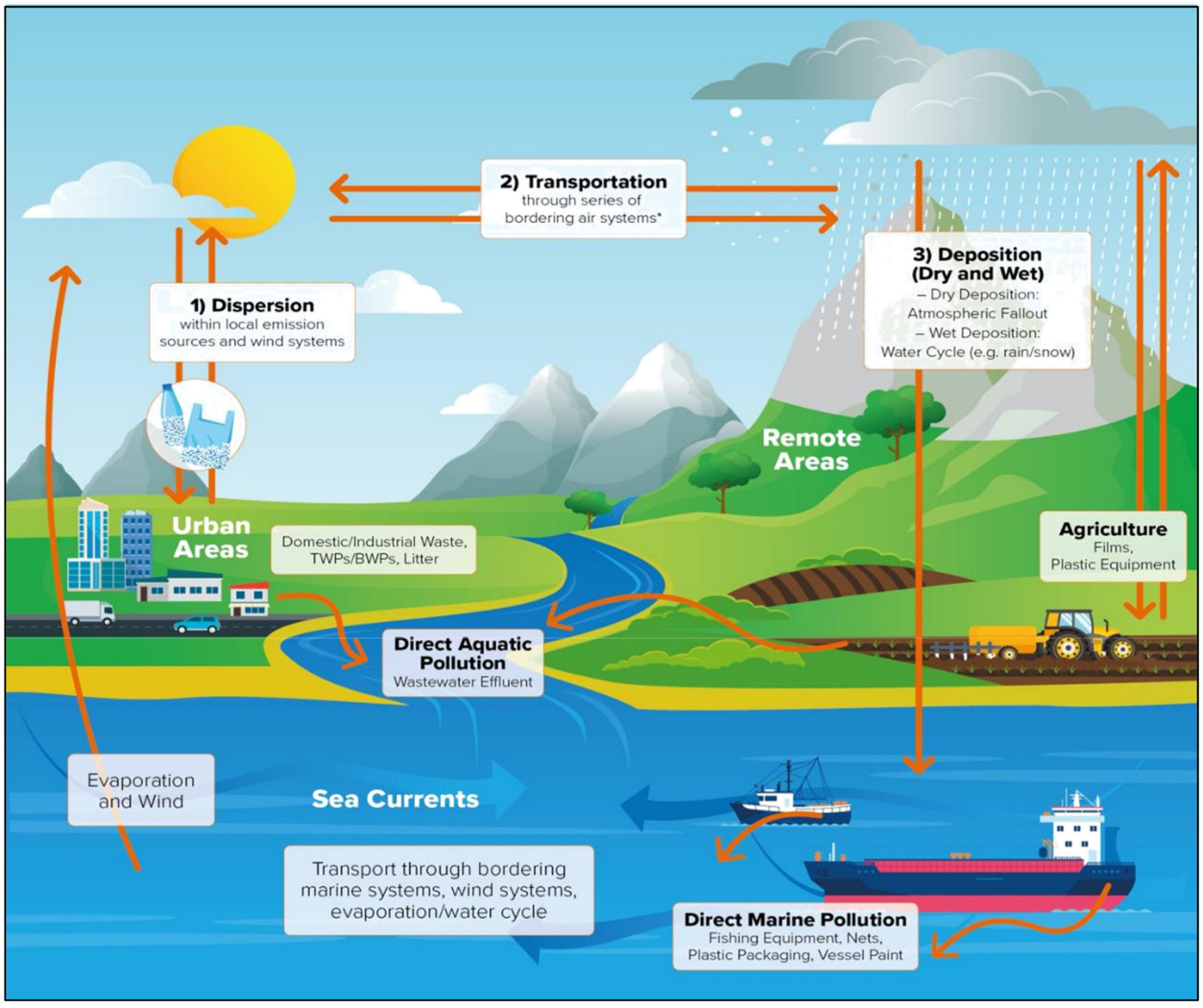

Figure 2.1: Atmospheric transport of MPs. Reprinted with permission from Fox *et al.* [11].

Several studies have examined MP samples from different regions, highlighting their potential for long-range atmospheric transport and deposition in remote areas far from their sources. Allen *et al.* [14] investigated the atmospheric deposition of microplastics (MPs)

over a five-month period. They reported an average daily deposition rate of 365 MPs per square meter, indicating significant accumulation even in remote environments. While the research suggests that MP sources may extend beyond local areas up to 95 km from the site, with potential influences from precipitation and wind patterns, it does not confirm long-range transport from densely populated regions. The settling velocity of MPs in this study was calculated using Dust Entrainment and Deposition (DEAD) model [68], assuming an equivalent sphere for all MPs. Bergmann *et al.* [15] investigated whether atmospheric transport contributes to the presence pf MPs in the arctic snow. They analyzed samples from the Arctic, the Swiss Alps, and populated areas in Europe. While Arctic snow had significantly lower MP concentrations than European snow, the presence of MPs in such isolated areas suggests their long-range transport. These findings indicate that atmospheric transport can carry MPs over vast distances, highlighting the need for further research into their long-range transport and deposition. The study by Wright *et al.* [12] investigates the deposition of MPs in urban London, revealing their ubiquitous presence in the atmosphere with deposition rates ranging from 575 to 1008 microplastics per square meter per day. They performed a backward trajectory analysis utilizing Hybrid Single-Particle Lagrangian Integrated Trajectory (HYSPLIT) to identify potential sources of MPs. Their modeling results revealed that local sources in the urban environment, such as foot traffic and construction activities, significantly influenced MP deposition in central London, rather than meteorological factors. The settling model used in their study was Henn's model [69], which was developed to estimate the settling of long cylinders at low Reynolds numbers. Brahney *et al.* [56] utilized the Community Earth System Model (CESM) to simulate the transport and deposition of MPs over a four-year period (2015-2019) in the western United States. The model incorporates various particle sizes and sources to estimate deposition rates. Sensitivity analyses in their study highlighted the significance of temporal and spatial resolution in data collection. Their findings underscore significant uncertainties, particularly regarding oceanic contributions, and emphasizes the need for more comprehensive data on MP concentrations and their environmental impacts

to enhance understanding of their role in the atmospheric component of the plastic cycle. Spehrical shapes were assumed for the MPs in this study. Depending on the length of the fibres, their aerodynamic sizes were classified into three categories: small, medium, and large. Evangeliou *et al.* [16] simulated the atmospheric transport of MPs originating from tire and brake wear particles and found that these particles exhibit high transport efficiency to remote areas, including the Arctic, where their absorption may lead to expedited melting of glaciers. They also found that the deposition rate of atmospheric MPs from tire and brake wear into the world's oceans was comparable in magnitude to the total amount transported by rivers. To model the settling of MPs, they assumed spherical shapes, involving some uncertainties in their size distribution. In another study, Evangeliou *et al.* [26] utilized data from deposition measurements in the Western USA, along with Bayesian inverse modeling and Lagrangian particle dispersion models, to estimate the emissions of MPs on a global scale. Key findings indicate significant annual emissions from multiple sources, such as agriculture, road dust, and oceanic contributions, as well as a significant presence of these pollutants in urban and coastal areas. Martina and Castelli [70] used the Lagrangian particle dispersion model MILORD in backward mode to simulate the potential long-range transport pathways of MPs to remote sites. They based their case study on Allen *et al.* [14] who found that the MPs collected in a remote prisitne site in the French Pyrenees likely traveled from over 100 km away due to low local population density. MILORD modeling demonstrated that the long-range transport of MPs occurs when particles travel in the free atmosphere. Moreover, larger MPs with higher settling velocities are less likely to undergo long-range transport. They considered four different settling velocities for the MPs reported in previous studied [12, 14, 71]. Tatsii *et al.* [28] observed that microplastic fibres settle up to 76% more slowly than spheres of the same volume. Considering this reduced settling velocity in an atmospheric model, they demonstrated that microplastic fibres, especially around 1 mm in length, released in urban areas are likely to reach distant regions, including the Arctic. However, fibres as small as 100 μm can rise into the stratosphere, where exposure to ultraviolet radioation may lead to

degradation of the microfibres and release chlorine and bromine, potentially harming the ozone layer. They found that the model proposed by Bagheri and Bonadonna [31] is among the most accurate when validated against experimental data. Ward *et al.* [29] simulated the trajectory of a set of MPs in the atmosphere using HYSPLIT model. they found that shape has a notable effect on transport for MPs larger than 6 μm, whereas for smaller particles, the differences are minimal. Long fibres, in particular, were found to spread over a 32% larger area than spherical MPs at the largest equivalent size of 23.5 μm. The shape of MPs influences their transport within the 6–10 μm range, highlighting that particle shape is essential for understanding their global distribution and impact. Ganser model [40] was utilized to predict the settling velocity of MPs in this study, accounting for a variety of both spherical and non-spherical particles. In a recent study, Reininger *et al.* [72] investigated the effects of shape on the settling velocity and atmospheric transport of microplastic glitters and fibres. Their Results show that glitters and fibres settle 42%–78% slower than volume-equivalent spheres, leading to 12%–261% greater transport distances. Using the FLEXPART Lagrangian transport model along with the model by Bagheri and Bonadonna for gravitational settling of the particles [31], the study demonstrates that reduced settling velocities increase atmospheric residence time, allowing smaller glitters to travel up to 33 km. These findings highlight the need to consider shape effects in transport models and address the environmental risks of airborne microplastics.

2.1.2 Characteristics of Atmospheric Microplastics

MPs are found in various geometries in atmospheric deposits, including fibres, fragments, spheres, films, and foam [3, 18]. Several studies have reported fibres as the most abundant type of MPs in collected samples [11, 12, 19–25]. Therefore, this study focuses only on microfibres. The characteristics of microfibres vary significantly depending on the location from which they were collected. Table 2.1 summarizes the characteristics of MPs collected from the samples, including fibres, based on several studies. As can be found from this table,

the size and type of the atmospheric microfibres highly depend on the location where they are collected. In most of these studies, only the length of the fibres is reported, and there is less information on their diameter. However, based on the microfibre diameter ranges reported in Wright *et al.* and [12] and Dris *et al.* [21], the aspect ratio of the atmospheric microfibres ranges between one and about a hundred. Furthermore, based on the most abundant type of the microfibres reported in the literature, a range of microfibre density between 900 kg/m^3 (density of Polypropylene) and 1400 kg/m^3 (density of Polyethylene terephthalate) and a range of microfibre length between 100 μm and 700 μm can be considered.

Table 2.1: The characteristics of the atmospheric microplastic samples, including fibres, reported in the literature.

Location	Sample Type	Polymer Type [a]	Size (μm)	Shape	Reference
Paris, France	Urban outdoor air deposition	N/A	100-5000	Fibre ($< 90\%$), fragments ($\sim 10\%$)	Dris *et al.* (2015) [73]
Paris, France	Urban outdoor air deposition	N/A	50-5000	Fibre	Dris *et al.* (2016) [21]
Dongguan, China	Urban outdoor air deposition	PE, PP, PS	200-4200	Fibre (80%), foam, film, fragment	Cai *et al.* (2017) [32]
Yantai, China	Urban outdoor air deposition	PET, PVC, PE, PS	50-1000	Fibre (95.1%), fragment (4%), film (0.7%), foam (0.2%)	Zhou *et al.* (2017) [74]
Shanghai, China	Suspended outdoor dust	PET, PE, PES, PAN, PAA, RY, EVA, EP, ALK	23.07-9555	Fibre (67%), fragment (30%), granule (3%)	Liu *et al.* (2019) [75]
Asaluyeh, Iran	Urban dust	N/A	2-100	Fibre, fragment, film	Abbasi *et al.* (2019) [76]
Nottingham, UK	Urban outdoor air deposition	PA, PET, PE	N/A	Fibre	Stanton *et al.* (2019) [77]

Location	Sample Type	Polymer Type [a]	Size (μm)	Shape	Reference
Hamburg, Germany	Urban and rural outdoor air deposition	PE, EVA, PTFE, PVA, PET	$< 63 - 5000$	Fragment 95%, fibre: 5%	Klein and Fischer (2019) [78]
London, UK	Urban outdoor air deposition	PAN, PES, PP, PVC, PET, PUR, PS	75-1080	Fragment, film, foam, granule	Wright *et al.* (2020) [12]
Guangzhou, China	Urban outdoor wet and dry deposition	PET, PE	50-5000	Fibre, fragment, film, microbead	Huang *et al.* (2021) [79]
Nam Co Basin, China	Remote outdoor air deposition	PP	50-300	Fibre, film	Dong *et al.* (2021) [80]
Ontario, Canada	Urban outdoor air deposition	PET, PA	20-4980	Fibre, fragment	Welsh *et al.* (2022) [81]
Mexico City, Mexico	Urban outdoor wet and dry deposition	PET, PE, PA, RY	39-5000	Fibre	Shruti *et al.* (2022) [82]
Ahvaz, Iran	Industrial and urban outdoor air deposition	PET, Nylon, PP	$< 100 - 1000$	Fibre	Abbasi *et al.* (2023) [83]
Chagar Hutang, Kuala Nerus, and Bangi, Malaysia	Remote and urban outdoor air deposition	PA, PP, PES, Nylon	5-50 (85%), 50-5000 (15%)	Fibre (40%), fragment (60%)	Hee *et al.* (2023) [13]
Kassel, Germany	Urban outdoor wet and dry depositions	PP, PE, PBT, PVC	$> 11\mu$ m (average size 50μm in wet and 45 μm in dry depositions)	Fibre, fragment	Kernchen *et al.* (2024) [84]

Location	Sample Type	Polymer Type [(a)]	Size (μm)	Shape	Reference
Shaanxi, China	Urban outdoor deposition	PP, PE, PAN, PET, PVC, PS	< 5 μm (94% of fibres are smaller than 5 μm)	Fibre (92%), films	Wang *et al.* (2024) [85]

[(a)] PA: polyamide; PAA: polyacrylic acid; PAN: polyacrylonitrile; PBD: polybutadiene; PBT: polybutylene terephthalate; PE: polyethylene; PES: polyester; PET: polyethylene terephthalate; PMMA: poly(methyl methacrylate); PP: polypropylene; PS: polystyrene; PTFE: Poly-tetra-fluoro-ethylene; PUR: polyurethane; PVA: polyvinyl alcohol; PVC: polyvinyl chloride; ALK: alkyd; EP: ethylene propylene; EVA: ethylene-vinyl acetate; RY: rayon.

2.2 Other Applications

The settling of cylindrical particles at low Reynolds numbers is also significant in various industrial processes. In paper manufacturing, for example, the settling of fibres in the pulp slurry must be controlled to achieve desired paper properties, such as strength, texture, and opacity, and to ensure their even distribution [36, 43, 44]. As another example, the settling dynamics of fibres during mixing and pouring in the production of fibre-reinforced polymer composites directly impact the material structural integrity [45, 46]. Furthermore, controlling the settling of fibres plays a crucial role in various biomedical processes, including tissue engineering and drug delivery. In tissue engineering, fibre scaffolds serve as a structural framework that supports cell growth and facilitates the regeneration of damaged tissues [47]. In drug delivery, fibres act as carriers, allowing for the controlled and targeted release of therapeutic agents to specific sites in the body [48].

2.3 Settling of Particles

Modeling the settling of microfibres is crucial for accurately simulating their long-distance transport [12, 14, 27, 28]. In this study, the settling of cylindrical rods is investigated under a force balance condition, where the sum of vertical forces acting on the rod is zero, resulting in zero acceleration. In general, during particle settling, gravity acts as the downward force, while drag and buoyancy forces act upwards. Figure 2.2 illustrates a schematic of the forces acting on a particle settling in a fluid. The force balance is given by:

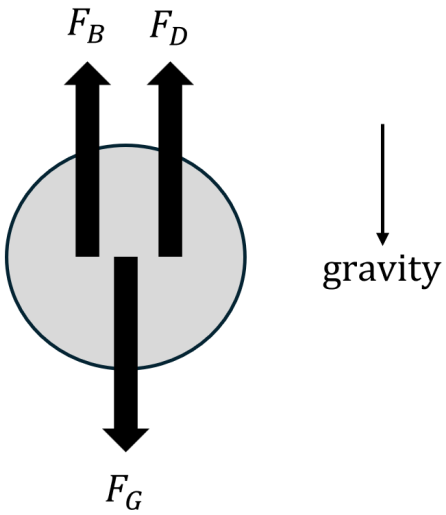

Figure 2.2: A schematic of the forces applied to a particle settling in a fluid.

$$F_B + F_D - F_G = 0 \tag{2.1}$$

where F_B, F_D, and F_G represent the buoyancy, drag, and gravity forces, respectively, and are calculated from

$$F_B = \rho_f g V_P, \tag{2.2}$$

$$F_D = \frac{1}{2}\rho_f V_S^2 A_P C_D, \tag{2.3}$$

and

$$F_G = \rho_P g V_P. \tag{2.4}$$

In equations 2.2, 2.3, and 2.4, ρ_f, g, V_P, V_S, A_P, and C_D represent the surrounding fluid density, gravitational acceleration, particle volume, particle terminal velocity, projected area, and drag coefficient. If $\rho_P >> \rho_f$, the buoyancy force (F_B) is much smaller than the gravity force (F_G) and can be neglected in the force balance equation (equation 2.1). For instance, in the case of plastic particles settling in air, $\rho_P \approx 1000\rho_f$, resulting in a negligible buoyancy force compared to the gravitational force. However, the buoyancy force cannot be ignored when studying the settling of brass or aluminum rods in water, as the rod densities are approximately 8 and 3 times that of the fluid, respectively. This section reviews models from the literature for estimating the drag coefficient and terminal velocity of spherical and non-spherical particles at low Reynolds numbers.

2.3.1 Settling of Spheres

Various theoretical and empirical correlations have been developed to estimate the drag coefficient and settling velocity of spherical particles, referred to as the simplest particle geometry [86]. Stokes' law ($C_D = 24/\mathrm{Re}$) can be applied to determine the settling velocity of a sphere falling at Reynolds numbers smaller than one [87]. For Reynolds numbers greater than one, the results begin to deviate from Stokes' law, as anticipated given the assumptions made during its derivation. A standard C_D versus Re curve for a sphere is provided by Clift *et al.* [88], covering a broad range of Reynolds numbers beyond the applicability of Stokes' law. Cheng [89] derived a general correlation for the drag force applied to a falling sphere, which is valid for the entire subcritical regime ($\mathrm{Re} < 2 \times 10^5$). Their model for a sphere drag coefficient is

$$C_D = \frac{24}{\mathrm{Re}} \left(1 + 0.27\mathrm{Re}\right)^{0.43} + 0.47 \left[1 - \exp\left(-0.04\mathrm{Re}^{0.38}\right)\right], \tag{2.5}$$

where The right-hand side consists of two terms. The first term represents an extended form of Stokes' law, valid for Re < 100. The second term is an exponential function that accounts for higher Reynolds numbers within the subcritical regime. In another example, Hartman *et al.* [90] developed empirical correlations to predict the settling velocity of spheres in a fluid, focusing on the relationship between Reynolds number and Archimedes number. Archimedes number (Ar) represents the ratio of the buoyant force to viscous force and is given by

$$Ar = \frac{D_P^3 g \rho_f (\rho_P - \rho_f)}{\mu_f^3}, \tag{2.6}$$

where D_P and μ_f denote the sphere diameter and fluid dynamic viscosity, respectively. They validated the accuracy of their model using experimental data by dropping glass spheres in dimethyl phthalate ester, covering a Reynolds number range of 5.2 to 78.2. Terfous *et al.* [91] discussed the impact of particle characteristics and fluid properties on the settling behavior of spherical particles, evaluated different models for calculating drag coefficients and settling velocities, and proposed a model that demonstrated superior accuracy compared to previous methods. To validate their model, they conducted experiments by releasing glass and PVC spheres into water–petroleum mixtures, covering a range of low Reynolds numbers from 2×10^{-4} to 0.3. The model's reliability was confirmed through the agreement with the experimental results. Barati *et al.* [92] presented another correlation for the drag coefficient of spherical particles utilizing "Multi-gene Genetic Programming" approach within the subcritical range of Reynolds number ($10^{-3} <$ Re $< 2 \times 10^5$). Kalman and Matana [86] presented three correlations based on their experiments with falling spheres within $10^{-2} <$ Re $< 10^4$. They proposed a correlation between Reynolds and Archimedes numbers to calculate the settling velocity, a correlation between Reynolds and Haider number (a non-dimensional number including the terminal velocity and not the particle size) to calculate the spherical particle size, and another correlation between drag coefficient and Reynolds number. They stated that using the Reynolds-Archimedes correlation is a simpler method for calculating the settling velocity.

2.3.2 Settling of Non-Spherical Particles

The settling velocity and behavior of non-spherical particles have been studied in several examples in the literature. The deviation of non-spherical particle geometry from a perfect sphere, characterized by shape factor, plays a significant role in the settling behavior of these particles [93, 94]. In a sample study, Ganser [40] derived a model for the drag coefficient of both isometric and nonisometric particles. In their model, the drag coefficient applied to the particle is predicted using a function of only generalized Reynolds number ($\mathrm{Re}K_1K_2$), where K_1 and K_2 are Stokes' and Newton's shape factors, respectively. Their model is given by

$$C_D = \frac{24}{\mathrm{Re}K_1}(1 + 0.1118(\mathrm{Re}K_1K_2)^{0.6567}) + \frac{0.4305}{1 + \frac{3305}{\mathrm{Re}K_1K_2}}. \tag{2.7}$$

For the settling of nonisometric particles in an infinite medium, K_1 and K_2 can be determined from

$$K_1 = (\frac{1}{3}\frac{d_n}{d_v} + \frac{2}{3}\phi^{-0.5})^{-1}, \tag{2.8}$$

$$K_2 = 10^{1.8148(-log\phi)^{0.5743}}, \tag{2.9}$$

where ϕ is the sphericity of the particle, defined as the ratio of the surface area of a volume-equivalent sphere to that of the particle. d_n and d_v represent the diameter of a sphere with identical volume and projected area, respectively. In another study, Song *et al.* [38] conducted experiments by dropping individual spheres, cubes, and cylinders of varying sizes and aspect ratios into water-glycerin mixtures to investigate the relationship between the drag coefficient and Reynolds number. The Reynolds number based on a volume-equivalent diameter ranges between 0.001 and 100 in their study. Furthermore, The aspect ratios of the cylindrical rods in their research varied from 0.1 to 5. Sphericity and the projected area ratio (the ratio of the projected area of a volume-equivalent sphere to that of the particle) were the two shape factors introduced in their proposed correlation between the drag coefficient and Reynolds

number. They demonstrated that their model aligned well with the experimental data points, with a discrepancy of less than 3.52%. The model by Song *et al.* [38] is given as

$$C_D = \frac{24}{\mathrm{Re}\phi^{c'} S^{d'}}(1 + a'Re)^{b'}, \tag{2.10}$$

where Re is calculated based on the diameter of a volume-equivalent sphere, and ϕ and S are the particle sphericity and projected area ratio, respectively. Additionally, a', b', c', and d' are the coefficients of the equation. The terminal velocity of the particle can be calculated through an iterative solution starting with an initial guess for Re. The solution is repeated until convergence is achieved for Re, C_D, and the particle terminal velocity [38]. This iterative solution can be applied to all other models for the drag coefficient in which C_D is expressed as a function of Re and other geometric parameters. Bagheri and Bonadonna [31] studied the settling of a wide range of particle geometries including irregular geometries, as shown in figure 2.3, below the sub-critical particle Reynolds number ($\mathrm{Re} < 3 \times 10^5$). Two shape factors were employed to establish a model for the drag coefficient of the particles: flatness, which is the ratio of the shortest length to the intermediate length, and elongation, which is the ratio of the intermediate length to the longest length.

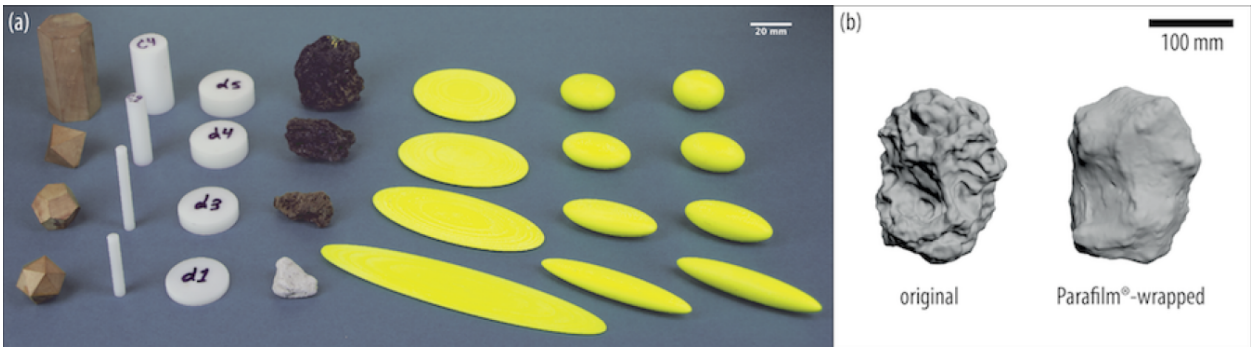

Figure 2.3: A selection of non-spherical particles studied by Bagheri and Bonadonna [31]. Reprinted with permission from Bagheri and Bonadonna [31].

The model by Bagheri and Bonadonna [31] for drag coefficient is given as

$$C_D = \frac{24k_S}{\mathrm{Re}}\left(1 + 0.125\left(\mathrm{Re}\frac{k_N}{k_S}\right)^{2/3}\right) + \frac{0.46k_N}{1 + \frac{5330}{\mathrm{Re}\frac{k_N}{k_S}}}, \tag{2.11}$$

where

$$k_S = \frac{F_S^{1/3} + F_S^{-1/3}}{2}, \tag{2.12}$$

$$k_N = 10\alpha_2\left[-\log(F_N)\right]^{\beta_2}, \tag{2.13}$$

$$\alpha_2 = 0.45 + \frac{10}{\exp\left(2.5\log\rho'\right) + 30}, \tag{2.14}$$

$$\beta_2 = 1 - \frac{37}{\exp\left(3\log\rho'\right) + 100}, \tag{2.15}$$

and

$$F_S = fe^{1.3\left(\frac{d_{\mathrm{eq}}^3}{LIS}\right)}, \tag{2.16}$$

$$F_N = f^2 e^{\left(\frac{d_{\mathrm{eq}}^3}{LIS}\right)}. \tag{2.17}$$

In the equations 2.11 to 2.17, f, e, L, I, S, ρ', and d_{eq} are flatness, elongation, the longest length, the intermediate length, the shortest length, the ratio of the particle density to that of the fluid, and the diameter of the volume-equivalent sphere, respectively.

Zhang and Choi [39] proposed a new shape-dependent model based on the previously published measurement data of virgin microplastic particles to calculate the terminal velocity of microplastic fibres. Their model is capable of distinguishing between the morphologies of fibres, films, and fragments utilizing Aschenbrenner shape factor. Yu *et al.* [95] developed a new drag coefficient correlation for various microplastic shapes based on 1343 data points from the literature. Their model showed improvement in predicting drag coefficient within

the range of $1 < \mathrm{Re} < 1000$. They also introduced an explicit model to estimate the terminal velocity. Cheng *et al.* [96] studied the settling of a range of non-spherical particles including spheroids, cubes, disks, and cylinders via numerical simulations within the Reynolds number range between 0.00277 and 562. They found that the drag force exerted on the non-spherical particles is larger than that on the equivalent sphere, resulting in a lower terminal velocity, especially at higher Reynolds numbers. They also found that the particles maintain their initial orientation within the Stokes regime while they reorient themselves to a stable state within intermediate Reynolds regimes. Kalman and Portnikov [97] experimentally investigated the free falling of a range of cylinders, disks, and irregular particles with various sphericities within a wide range of Reynolds number ($10^{-2} < \mathrm{Re} < 10^4$). In their proposed model, the flow mode is initially determined based on the particle sphericity and Reynolds number. Subsequently, the particle terminal velocity and drag coefficient are determined based on three observed trends of sphericity. The first trend pertains to nearly spherical particles with their sphericities exceeding 0.87, while the other two trend lines represent sphericities lower than 0.87, one for discs and the other for cylinders. The models for the drag coefficient of non-spherical particles are reviewed by Michaelides and Feng [94]. They discovered that the drag coefficient of nonspherical particles differs significantly from that of spherical particles, and the shape of the particles plays a crucial role in its determination. Current drag coefficient correlations for nonspherical particles exhibit significant errors, with an average discrepancy of at least 20% and a maximum discrepancy exceeding 100% when compared to experimental data. In a recent study; however, Qian *et al.* [98] developed a machine learning model to predict the settling velocity of MPs with various shapes, including fibre, film, and fragment. By incorporating dimensionless size, relative density, and optimal shape parameters (Corey shape factor, flatness, elongation, and sphericity for the fragment, film, fibre, and mixed-shape MPs, respectively), the model achieved high accuracy ($R^2 > 0.867$, R^2 is the coefficient of determination) compared to traditional methods. They concluded that MP size is the most influential factor especially for $D^* = D_{eq}(g/\nu_f^2)^{1/3} < 80$, where D^*, D_{eq}, g, and ν_f represent

dimensionless diameter, the diameter of a volume-equivalent sphere, gravitational acceleration, and the fluid kinematic viscosity, respectively. Furthermore, MP shape has a greater impact on the settling velocity when $D^* > 65$. However, no explicit equation was proposed in this study to calculate the drag coefficient or terminal velocity of MPs. More accurate correlations should be derived for specific particle shapes, such as cylindrical geometries, when studying the settling of microfibres in the atmosphere.

2.4 Settling of Cylindrical Rods

This section reviews previous studies on the settling of cylindrical rods, focusing on aspects such as straight rods, curved and bent rods, the effects of asymmetry in rod geometry on settling, and the impact of rod rotation during settling.

2.4.1 Straight Rods

Several studies have investigated the settling of straight cylindrical rods and fibres at low Reynolds numbers in a quiescent fluid, which is associated with the atmospheric settling of plastic microfibres. A straight rod settles at a lower rate than a volume-equivalent sphere because of its higher drag coefficient [99–101]. Jayaweera and Mason [99] performed an experimental study on the terminal velocity and drag coefficient of cylinders in a viscous fluid within a broad range of Reynolds numbers. They observed that the cylinders maintain their initial drop orientations at $\mathrm{Re} < 0.01$, while they are oriented horizontally and show the maximum resistance for $\mathrm{Re} > 0.01$. Re is calculated based on the cylinder diameter in their study. However, Mcnown and Malaika [101] observed a horizontal orientation for the falling cylinders within $\mathrm{Re} > 0.1$, where Re is calculated based on the diameter of the volumetric-equivalent sphere.

The settling behavior of rods and fibres with finite lengths in their stable horizontal orientation has been explored in various studies. In this case, the terminal velocity of rods and fibres depends on their diameter and length. Jayaweera and Mason [99] found that the

terminal velocity of a cylindrical rod increases with both rod diameter and aspect ratio, approaching a constant value at high aspect ratios. In another study, Yang *et al.* [37] demonstrated through gray correlation analysis that the diameter influences the settling velocity to a much greater extent than the moisture absorption rate, fibre length, and curvature. Henn [69] developed a theoretical formula for the terminal velocity of a collection of long fibres. The highest error was reported as 5% when comparing Henn's results with experimental data for the ratio of the aerodynamic equivalent diameter (D_a) to the fibre diameter (D_c) given by D_a/D_c (performed with diameters of 1, 1.5, and 2 μm and aspect ratios (AR) between 10 and 150). Henn's model [69] is given by

$$V_S = \frac{(\rho_p - \rho_f) g D_c^2}{8\mu_f \left\{ \left[\frac{0.448}{\ln 2AR - \frac{1}{2}} \right] + \left[\frac{1.788}{\ln 2AR + \frac{1}{2}} \right] \right\}}, \tag{2.18}$$

where V_S, ρ_P, ρ_f, g, D_c, and μ_f are the fibre terminal velocity, fibre density, fluid density, gravitational acceleration, fibre diameter, and fluid dynamics viscosity. Goral *et al.* [42] conducted a series of experiments to determine the terminal velocity and drag coefficient of both regular, including cylinders and fibres, and irregular shapes. They developed a set of shape-by-shape correlations between the drag coefficient and Reynolds number applicable to broad ranges of Reynolds numbers. Their model for circular cylinders is based on the volumetric-equivalent sphere diameter and holds for $\mathrm{Re} > 1$. They demonstrated that their model yielded lower errors than the model proposed by Yu *et al.* [95] when considering all the data from both studies.

In cases where the orientation of the straight rod is not horizontal, the orientation angle affects the settling velocity due to its impact on the resistive forces. Khayat and Cox [100] developed a theoretical model to predict the force per unit length acting on a long slender body with either straight or curved centerlines and an arbitrary inclination angle, subjected to a uniform flow. For the case of circular cross-section and fore-aft symmetry, the model by Khayat and Cox [100] is given by

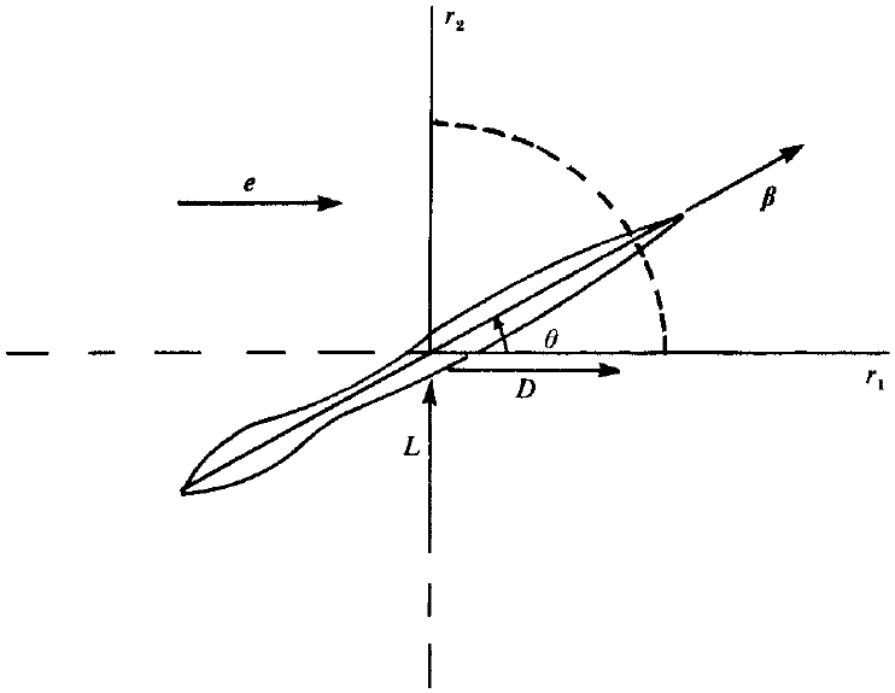

Figure 2.4: The drag (D) and lift components (L) applied to an inclined slender body. Reprinted with permission from Khayat and Cox [100].

$$\frac{D}{\mu U a} = \frac{-4\pi(2-\cos^2\theta)}{\ln\kappa + F_D(Re;\theta)} + O\left(\frac{1}{\ln\kappa}\right)^3, \tag{2.19}$$

where

$$\begin{aligned} F_D(\mathrm{Re};\theta) = \Bigg\{ & \frac{\cos^2\theta}{2\,\mathrm{Re}}\left[E_1(\mathrm{Re}(1-\cos\theta)] + \ln[\mathrm{Re}(1-\cos\theta)] + \gamma' - \mathrm{Re}(1-\cos\theta)\right] \\ & + \frac{\cos^2\theta}{2\,\mathrm{Re}}\left[E_1[\mathrm{Re}(1+\cos\theta)] + \ln[\mathrm{Re}(1+\cos\theta)] + \gamma' - \mathrm{Re}(1+\cos\theta)\right] \\ & + \left(2-\cos^2\theta\right)\Bigg[E_1[\mathrm{Re}(1-\cos\theta)] - \frac{\mathrm{e}^{-\mathrm{Re}(1-\cos\theta)}-1}{\mathrm{Re}(1-\cos\theta)} + \ln(1-\cos\theta) \\ & + E_1[\mathrm{Re}(1+\cos\theta)] - \frac{\mathrm{e}^{-\mathrm{Re}(1+\cos\theta)}-1}{\mathrm{Re}(1+\cos\theta)} + \ln(1+\cos\theta) \\ & + 2\left(\gamma' + \ln\frac{1}{4}\,\mathrm{Re}\right)\Bigg] + 3\cos^2\theta - 2\Bigg\}\,\frac{1}{2\,(2-\cos^2\theta)}. \end{aligned} \tag{2.20}$$

In equations 2.19 and 2.20, $E_1(x) = \int_x^\infty \frac{e^{-t}}{t}dt$, Re is calculated based on the cylinder half-

length (a), κ is twice the inverse of the cylinder aspect ratio ($2/AR$), γ' is the Euler's constant (0.577), and θ is the cylinder inclination angle measured relative to the flow direction, as shown in figure 2.4. Kharrouba *et al.* [41] analyzed flow around finite cylinders oriented at various angles relative to the incoming flow, across a broad range of Reynolds numbers, from creeping flow up to Re = 400. They derived correlations for the hydrodynamic forces and torques acting on the cylinders as functions of inclination angle. Lopez and Guazzelli [102] proposed a model to predict the settling velocity, orientation, and three-dimensional trajectory of fibres in vortical flow under the influence of fluid inertia. Their model improves upon slender body theory (SBT) [100] for particles with finite aspect ratios and Reynolds numbers, but is valid only when the Reynolds number based on cylinder half-length exceeds 1. These studies collectively indicate that the non-dimensional resistive force coefficients tend to decrease as the rod becomes more vertically aligned, potentially leading to higher terminal velocities for inclined cylinders during settling.

Several other studies have examined the settling behavior of two-dimensional cylinders, which serve as idealized representations of very long rods or fibres. For instance, Khalili and Liu [103] analyzed the flow past a 2D cylinder using the Lattice Boltzmann method and determined an equation for the drag coefficient. Their model can be applied to determine the terminal velocity of an infinite cylinder within a range of Reynolds numbers based on the cylinder diameter, spanning from 3×10^{-5} to 1, and is given by

$$C_D = \frac{4\pi\delta}{\mathrm{Re}} \left(\frac{2}{1 + \sqrt{1 + 4.3\delta^2}} \right), \tag{2.21}$$

where $\delta = [1/2 - \gamma' - \ln(\mathrm{Re}/4)]^{-1}$, γ' is Euler's constant (0.577), and Re is calculated based on the cylinder radius. In another example, Huner and Hussey [104] derived a model for the drag coefficient of an infinite circular cylinder within the Reynolds number (based on the cylinder diameter) between 0.23 and 2.6. They also developed two additional relationships that account for the effects of the finite length of the cylinder as well as the finite boundaries on the cylinder terminal velocity. Furthermore, Sen *et al.* [105] studied a uniform flow past a

cylinder using a stabilized finite-element method and derived a model to calculate the drag coefficient of an infinite cylinder. This model is valid for Reynolds numbers (based on the cylinder diameter) between 15 and 40 and for a blockage ratio (the ratio of the cylinder diameter to the domain width) between 0.000125 and 0.8. Their model is given as

$$C_D = \frac{7.89}{Re^{0.50}} + 0.26, \tag{2.22}$$

where Re is based on the cylinder diameter.

Reviewing past studies on the settling of cylindrical rods and fibres reveals that the terminal velocity of rods depends on their size, including diameter and length, as well as their orientation during settling. In a recent study, Yuan *et al.* investigated the settling behavior of submillimeter microplastic fibres in still water using numerical analysis. They found that within the laminar regime (Re<0.1, where Re is calculated based on the fibre volume-equivalent diameter) Stokes' law ($C_D = 24/\mathrm{Re}$) accurately predicts the terminal velocity of the fibres with small orientation angles ($\theta < 30°$, where θ is the angle between the fibre axis and horizontal direction). However, within the same range of Reynolds number, the orientation angle becomes influential for $\theta > 30°$. To account for this effect, they proposed a new model for fibres within this range of orientation angles:

$$C_D = [75.47\exp(1 - \cos\theta/0.168) + 24]/\mathrm{Re}. \tag{2.23}$$

This model incorporates the porosity of the microfibre texture, which affects the apparent density of the fibre, and can be applied to settling of microfibres with different orientations within $0 < \theta < 90°$. More accurate models are still needed to predict the drag coefficient and terminal velocity of fibres settling in the atmosphere.

2.4.2 Curved and Bent Rods

Real microfibres found in the atmospheric deposition samples usually have geometries different from straight cylinders [3, 30, 32, 33, 106]. Several studies have investigated how curvature

and bending affect the settling of cylindrical particles. Cox [107] developed a theoretical model to predict the force per unit length of long slender bodies with both straight and curved centerlines when subjected to a uniform flow within Stokes' regime. Asymptotic expansions as a function of the inverse of the slender body aspect ratio are utilized in their model. Figure 2.5 illustrates a schematic of a slender body curved in an arc of a circle.

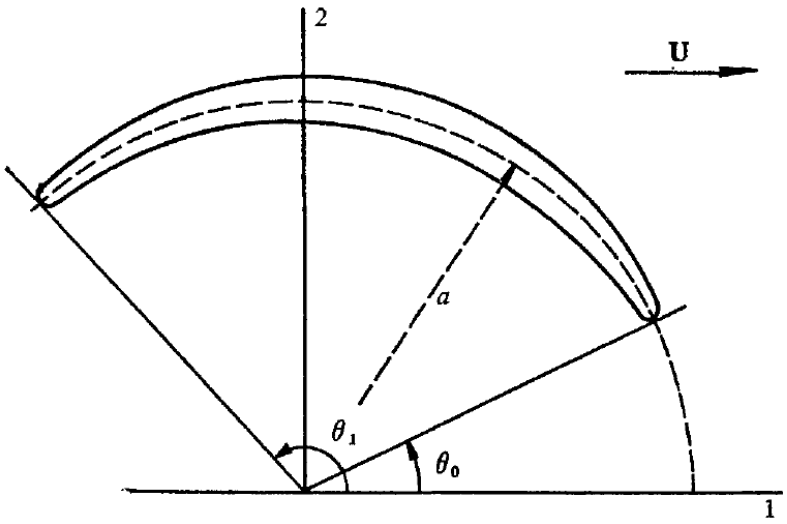

Figure 2.5: Schematic of a slender body curved in a circle arc. θ_0 and θ_1 are the angles of the two endpoints, a is the radius of the circle, and U is the flow velocity. Reprinted with permission from Cox [107].

Based on the model by Cox [107], the resistive force applied to the curved slender body in the flow direction, denoted by F_1, is calculated from

$$F_1 = 2\pi\mu a U \left\{ \frac{A^*}{\ln a/b} + \frac{B^*}{(\ln a/b)^2} + O\left(\frac{1}{(\ln a/b)^3}\right) \right\}, \tag{2.24}$$

where

$$A^* = \frac{1}{2}\{3(\theta_1 - \theta_0) + \cos(\theta_0 + \theta_1)\sin(\theta_1 - \theta_0)\}, \tag{2.25}$$

$$B^* = -\frac{1}{2}\cos(\theta_0+\theta_1)\sin(\theta_1-\theta_0)\ln\left(\tan\frac{1}{4}(\theta_1-\theta_0)\right) - 6\int_0^{\tan\frac{1}{4}(\theta_1-\theta_0)}\frac{\ln t\,dt}{1+t^2}$$
$$+\frac{1}{2}\cos(\theta_0+\theta_1)\sin\frac{1}{2}(\theta_1-\theta_0) - \frac{1}{12}\sin\frac{3}{2}(\theta_1-\theta_0) - \frac{2}{3}\sin\frac{1}{2}(\theta_1-\theta_0)$$
$$-\frac{1}{2}(1+9\ln 2)(\theta_1-\theta_0) - \frac{1}{2}(1+3\ln 2)\cos(\theta_0+\theta_1)\sin(\theta_1-\theta_0)$$
$$+\frac{1}{2}\int_{\theta_0}^{\theta_1}(3+2\cos 2\theta)(\ln\lambda)\,d\theta. \tag{2.26}$$

In equations 2.24 to 2.26, θ_0 and θ_1 are the angles of the two endpoints, a is the half-length of the cylinder, b is the corss-sectional radius of the body, U is the flow velocity, and $\lambda = 1$ for slender bodies with circular cross sections. In another example, Rong *et al.* [36] studied the effects of curvature on the terminal velocity and orientation of individual falling fibres utilizing the lattice Boltzmann method. They investigated three fibres with the same aspect ratio (one straight fibre and two curved fibres with different curl indexes). Their results show that a smaller radius of curvature at a constant fibre length leads to an increase in the final settling velocity. For the smaller radius of curvature, the fibre reaches its terminal velocity faster and shows less overshooting during its settling. Nguyen *et al.* [35] found that fibre length, curliness, and settling orientation affect its terminal velocity. Curliness is defined as the ratio of the length of a straight line connecting the two endpoints of the fibre to the total length of the fibre, given by L_C/L in figure 2.6. They observed that for fibres longer than 1 mm, an increase in the curliness of a fibre retards its settling rate. For instance, the terminal velocity of a microfibre with a length of 2 mm decreases by a factor of 1.75 times as the curliness increases from 1 to 1.3. Additionally, they demonstrated that the diameter of the volume-equivalent sphere is the best length scale for predicting the drag coefficient since this scaling results in the least variability in the drag coefficient for a given Reynolds number. Chow and Adams [108] also investigated the effect of curliness, but for the Reynolds number based on diameter between 200 and 6000. They observed that for the particles with almost the same density as the fluid, as the arc angle (θ in figure 2.7) increases from zero (straight cylindrical particle) to 180 degrees (semi-circle), the particle orientation changes from vertical

($\beta = 90°$; β represents the particle inclination angle, as shown in figure 2.7) to horizontal ($\beta = 90°$). For particles much denser than the medium, the particle tends to fall vertically along its entire trajectory. Huang *et al.* [109] numerically studied the terminal velocity and orientation of a torus in still fluid within the range of ($10 < \mathrm{Re} < 90$) (Re is calculated based on the diameter of the torus cross section, denoted by d, in figure) as they considered only a single value for aspect ratio). They concluded that within this range of Reynolds number, the torus reaches the same velocity and orientation regardless of its initial orientation. They observed that a non-zero inclination angle in the torus ($\theta \neq 0$; θ is shown in figure 2.8) causes zigzag motion and rotation around its axis, but the torus eventually reaches zero inclination angle and a constant terminal velocity. Moreover, a higher inclination angle leads to a larger horizontal drift specifically at higher Reynolds numbers. Candelier *et al.* [110] demonstrated through theoretical analysis that curved fibres consistently settle in a horizontal orientation within the Stokes regime but adopt an oblique orientation at higher Reynolds numbers. The oblique orientation of the curved fibres outside the Stokes regime is caused by a non-zero inertial torque, which influences the fibres' angular dynamics. Furthermore, the obliquely oriented fibres exhibit horizontal drifts while settling, which influence their trajectory during long-range transport in the atmosphere.

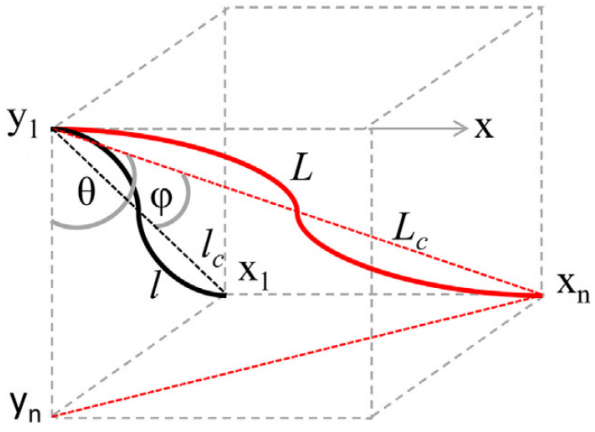

Figure 2.6: Curved fibre, characterized by curliness, defined as L_C/L. Reprinted with permission from Nguyen *et al.* [35].

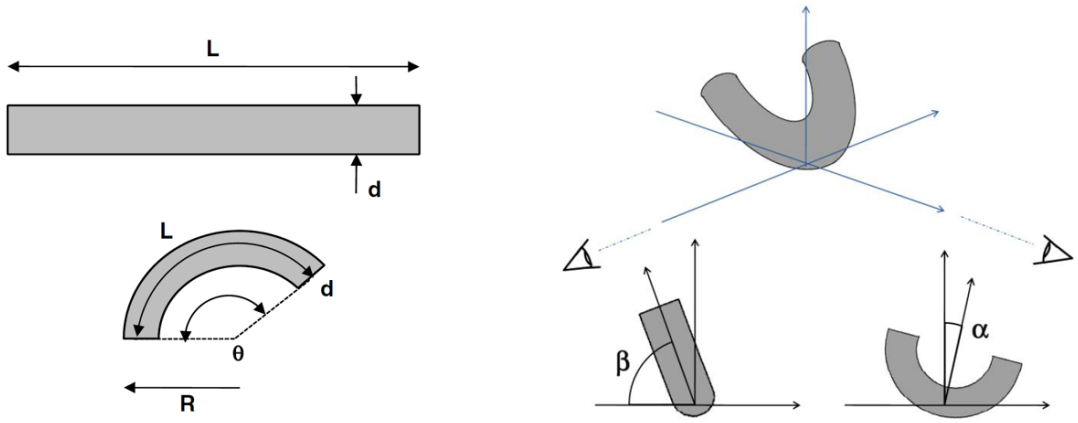

Figure 2.7: Schematic of the curved cylindrical rod studied by Chow and Adams [108]. L, d, θ, R, β, and α represent the rod length, diameter, arc angle, radius of curvature, inclination angle, and angular oscillation angle, respectively. Reprinted with permission from Chow and Adams [108].

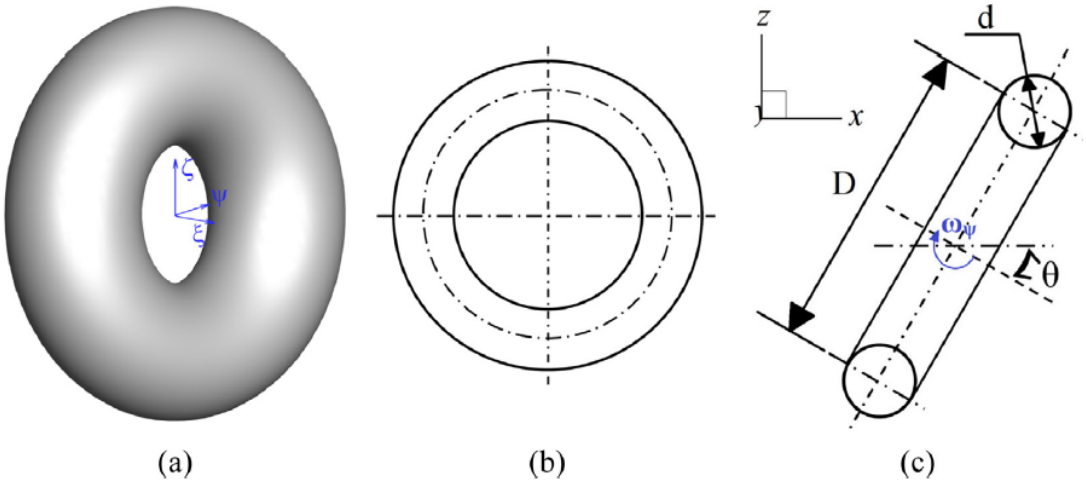

Figure 2.8: Dimensions and orientation of a torus settling in a quiescent fluid in the negative x direction. D, d, and θ represent the torus diameter, diameter of torus cross section, and inclination angle. Reprinted with permission from Huange *et al.* [109].

The drag force applied to the middle of a flexible fibre settling in air is smaller than the two ends, resulting in a bent geometry [111]. The deformation of the elastic fibre leads to a change in its settling velocity since the projected area and the fibre resistance against downward fall changes. Marchetti *et al.* [112] investigated the deformation of elastic fibres

using the dimensionless elasto-gravitational number ($\beta_E = F_g L_C^2/EI$) as a parameter. β_E is elasto-gravitational number, F_g is the fibre weight, L_C is the fibre length, E is the fibre elastic modulus, and I is the fibre second moment of inertia. Their findings indicate that for $\beta_E < 100$, the fibre deformation is negligible and its terminal velocity is the same as a rigid fibre settling broadside. For $100 < \beta_E < 1000$, the fibre adopts a V-shaped geometry, with its terminal velocity increasing with β_E. Finally, for $\beta_E > 1000$, the fibre deforms into a U-shaped, and its terminal velocity tends to approach 1.6 times that of a straight fibre. Li *et al.* [113] analyzed the orientation and trajectory of an elastic fibre while settling within $50 < \beta_E < 800$. Their results indicate that as β_E increases, the geometry of the fibre at terminal velocity deforms progressively more from a straight shape. The fibre transitions from a slightly curved shape to a V-shape, and finally to a U-shape as β_E increases from 50 to 800. The reorientation of the fibre before reaching the final stable shape results in the fibre rotation and coupling between horizontal and vertical translations [113, 114]. Various non-straight geometries of the fibres were also observed in the theoretical analysis performed by Delmotte *et al.* [115]. Based on their results, within $\beta_E < 100$, the height of the deformed fibre increases linearly with β_E, while the viscous drag remains constant and equal to that of a rigid fibre with the same properties. At $\beta_E > 3000$, metastable W-shaped geometry is observed which eventually converges to a horseshoe shape. Dai *et al.* [116] performed an experimental analysis on the settling of submillimetre fibres in still water within very low Reynolds numbers ($\mathrm{Re} < 0.05$). They observed that these fibres did not showcase significant bending, deformation, or rotation around their axis during their settling. In our recent study, Hamidi *et al.* [50] studied the settling of straight and curved cylindrical rods in a quiescent water-glycerin mixture. we developed a semi-empirical model to estimate the drag coefficient and terminal velocity of straight and curved rods with Reynolds numbers ranging from 0.03 to 5, rod aspect ratios between 3 and 120, and curvature indices between 0.02 and 0.25. Our model is given by

$$C_D = \frac{24}{\mathrm{Re}(\mathrm{AR}^{1.20}\phi^{4.38}\beta^{0.21})}(1 + 0.25\mathrm{Re})^{0.96}, \tag{2.27}$$

where ϕ is the rod sphericity and β is defined as the ratio of the curved rod projected length to the rod length. $\beta = 1$ for straight rods and $\beta < 1$ for curved rods.

2.4.3 Effects of Asymmetry

It is well known that the straight rods with fore-aft symmetry tend to settle broadside after reaching terminal velocity at low but finite Reynolds numbers in a quiescent fluid owing to the inertial torque applied [99–101]. However, rods with non-uniform mass distribution may adopt oblique orientations as a consequence of the interaction between inertial, gravitational, and hydrodynamic torques. The terminal velocity and trajectory of these rods are affected by their oblique orientations [100, 117–119]. Yasseri [120] conducted an experimental study on the falling of cylinders in water and found that all cylinders do not fall directly downwards. They can showcase complex trajectories and land at different locations considering their initial drop orientation and non-coincidence between the cylinder center of mass and geometry. Khayat and Cox [100] developed a model, known as slender body theory (SBT), to calculate the drag, lift, and torque applied to the unit length of a long slender body with an arbitrary centreline. They derived a term in their equation for the total torque acting on the rod, accounting for the effects of inertia and the asymmetry in the geometry of a straight cylinder. Based on their model, for a body with a circular cross-section, the total torque applied to the body while settling is calculated from

$$\frac{G}{\mu U a^2} = -2\pi \left(\frac{1}{\ln \kappa}\right)^2 \left[F_G(Re;\theta) + 2\sin\theta \int_{-1}^{1} s \ln R_s(s) \mathrm{d}s\right] + O\left(\frac{1}{\ln \kappa}\right)^3, \tag{2.28}$$

where G is the total toque applied to the slender body, U is the terminal velocity, a is the half-length of the body, κ is the inverse of the body aspect ratio, θ is the body inclination angle relative to a vertical axis, s is the normalized distance from the midpoint of the body,

scaled by a, and $R_s(s)$ is the cross-sectional radius of the body at location s. F_G denotes the inertial torque and can be calculated from

$$\begin{aligned} F_G(\mathrm{Re};\theta) = \Bigg\{ & \frac{\cos\theta}{\mathrm{Re}(1-\cos\theta)} \left[2 + 2\frac{\mathrm{e}^{-\mathrm{Re}(1-\cos\theta)} - 1}{\mathrm{Re}(1-\cos\theta)} - E_1[\mathrm{Re}(1-\cos\theta)] \right. \\ & \left. - \ln[\mathrm{Re}(1-\cos\theta)] - \gamma' \right] + \frac{\cos\theta}{\mathrm{Re}(1+\cos\theta)} \left[2 + 2\frac{\mathrm{e}^{-\mathrm{Re}(1+\cos\theta)} - 1}{\mathrm{Re}(1+\cos\theta)} \right. \\ & \left. - E_1[\mathrm{Re}(1+\cos\theta)] - \ln[\mathrm{Re}(1+\cos\theta)] - \gamma' \right] \\ & - 2 \left[\frac{1}{\mathrm{Re}(1-\cos\theta)} \left(1 - \frac{1-\mathrm{e}^{-\mathrm{Re}(1-\cos\theta)}}{\mathrm{Re}(1-\cos\theta)} \right) - \frac{1}{\mathrm{Re}(1+\cos\theta)} \right. \\ & \left. \times \left(1 - \frac{1-\mathrm{e}^{-\mathrm{Re}(1+\cos\theta)}}{\mathrm{Re}(1+\cos\theta)} \right) \right] \Bigg\} \sin\theta \end{aligned} \tag{2.29}$$

where $E_1(x) = \int_x^\infty \frac{e^{-t}}{t} dt$ and $\gamma' = 0.577$ (Euler's constant). In equation 2.28, $F_G(Re;\theta)$ represents the inertial torque, resulting from the asymmetry in the flow pattern surrounding the inclined rod, and $\int_{-1}^{1} s \ln R_s(s) \mathrm{d}s$ represents the gravitational torque, resulting from the offset of the centre of gravity from the rod midpoint due to the geometrical asymmetry. Once a settling rod reaches its terminal velocity, the total torque applied to the rod becomes zero, indicating a balance between the inertial torque and the gravitational torque. In the case of fore-aft symmetry, the gravitational torque is zero; therefore, the zero net torque is achieved at $\theta = 0, \pi/2$, associated with $F_G = 0$. The solution of $\theta = 0$ is considered unstable equilibrium as it leads to a vertical orientation for the rod. Consequently, $\theta = \pi/2$ or horizontal orientation is the stable orientation for the settling rod with fore-aft symmetry. However, for the case of fore-aft asymmetry, the gravitational torque is not zero, and the sum of the inertial torque (represented by F_G in equation 2.28) and gravitational torque (represented by $\int_{-1}^{1} s \ln R_s(s) \mathrm{d}s$ in equation 2.28) must be zero when the rod is settling with a stable terminal velocity, leading to an oblique inclination angle ($\theta \neq 0, \pi/2$). Candelier and Mehlig [121] investigated a dumbbell-shaped particle composed of two spheres connected by a weightless rigid rod, settling in a quiescent fluid at low Reynolds numbers, as shown in figure 2.9. Their findings indicate that the dumbbell settles vertically when the two spheres

have the same mass density but differ significantly in size, with the larger sphere positioned lower. As the size difference between the two spheres decreases, the dumbbell tends to adopt a stable oblique orientation, resulting in a horizontal drift along the trajectory. It adopts a completely horizontal orientation when the two spheres are identical in size.

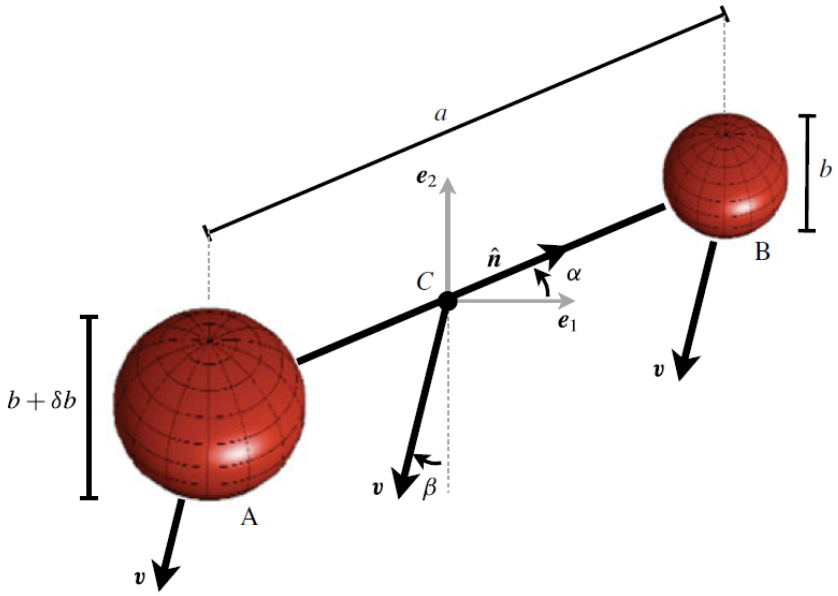

Figure 2.9: Settling of a dumbbell-shaped particle. Reprinted with permission from Candelier and Mehlig [121].

Some other studies have investigated the orientation of asymmetric cylinders or spheroids and assessed how this orientation affects their settling behavior. As shown in figure 2.10, Roy *et al.* [117] studied two cases of asymmetry for a fibre: offset of centre of gravity from the midpoint and a rod consisting of two coaxial cylinders with different radii and lengths. In figure 2.10, R_{COM} represents the centre of gravity offset from the midpoint of the fibre. They developed a map, as shown in figure 2.11, specifying the orientation of an asymmetric fibre, vertical or oblique, using two non-dimensional numbers, Archimedes (Ar) and asymmetry (δ), given by

$$\mathrm{Ar} = \frac{(\rho_P - \rho_f) g V_P}{2\pi \mu_f \nu_f \epsilon}, \tag{2.30}$$

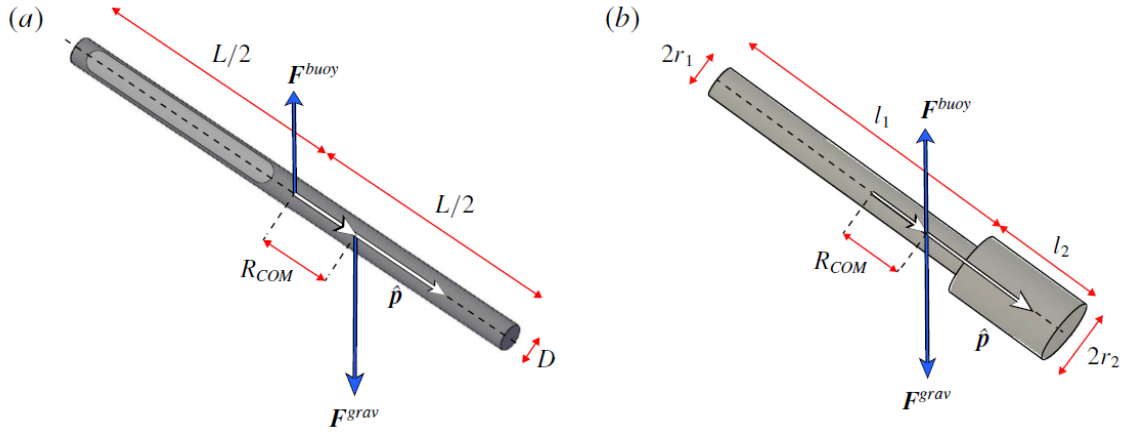

Figure 2.10: Settling asymmetric fibres: (a) uniform cylinder with centre of gravity offset from the midpoint, (b) a particle consisting of two coaxial cylinders of different radii and lengths. Reprinted with permission from Roy *et al.* [117].

$$\delta = \frac{R_{COM}}{l}, \tag{2.31}$$

where ρ_P is the fibre density, ρ_f is the fuid density, g is the gravitational acceleration, V_P is the fibre volume, ν_f is the fluid kinematic viscosity, $\epsilon = 1/\ln(AR)$, and l is the half-length of the fibre. Based on figure 2.11, fibres with an asymmetric distribution of radius or mass transition from a vertical to an oblique settling orientation when the Archimedes number exceeds a critical value or when the degree of asymmetry decreases below a certain level.

In another example, Angle *et al.* [119] studied the orientation and terminal velocity of cylinders settling in quiescent water with both uniform and non-uniform distributions of mass along the cylinder axis. Their observations demonstrated that the cylinder with non-uniform mass distribution settles vertically at $AR = 1$, while it settles with a slightly oblique orientation at $AR = 2$ and 4 due to higher inertia (F_G in equation 2.28). They observed three different settling modes: horizontal, oblique, and vertical oscillating orientations with vertical, angled, and laterally periodic trajectories, respectively. The total cylinder terminal velocity highly depends on the settling mode. The cylindrical particles with tilted orientations exhibit

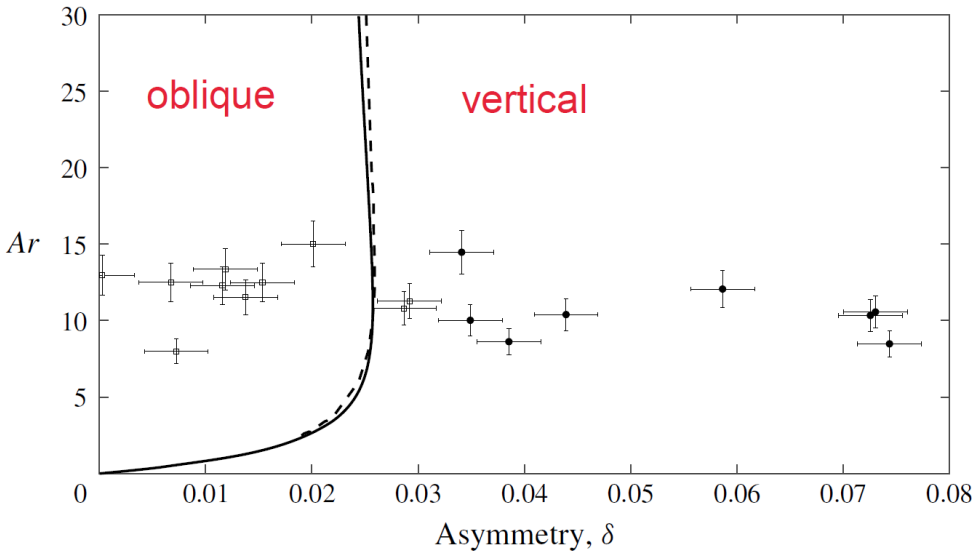

Figure 2.11: Orientation map showing where an asymmetric cylinder settles in vertical and oblique orientations. Filled circles represent vertical orientation and empty squares represent oblique ones. The solid line indicates the numerical phase boundary, while the dashed line shows the analytical approximation. Reprinted with permission from Roy *et al.* [117].

horizontal displacement towards the denser end of the particle along their trajectory [122]. Jiang *et al.* [118] investigated the settling behavior of a single spheroid with a mass center offset using the Newton-Euler equations. They found that the major axis orientation of a spheroid with a mass center offset shifts from horizontal to vertical as the mass center offset increases to the critical value, following a pitchfork bifurcation pattern. This transition can also be triggered by altering density ratio, Galileo number, or aspect ratio. Galileo number is defined as $\mathrm{Ga} = \sqrt{(\alpha - 1) g D_{eq}^3}/\nu$, where α represents the density ratio of the sphroid to the fluid, g represents the gravity, and D_{eq} represents the volumetric-equivalent diameter. Additionally, the maximum horizontal drift angle depends on the velocity ratio between vertical and oblique settling, increasing as the spheroid shape deviates further from a sphere.

2.4.4 Rotating Rods

The inertial torque, arising from the asymmetry of the flow around a settling object due to its geometry or orientation, tends to rotate the object until the net torque acting on the

body becomes zero [100, 117, 123]. The rotation of the objects under such circumstances and its potential impact on their settling have been studied in the literature. For example, Kry and List [124] studied the aerodynamics of spinning spheroids about their minor and major axes in a horizontal wind tunnel. They found that the aerodynamic torques applied to the spheroids only depend on the angular position of the spheroid as well as the airflow Reynolds number, and are unaffected by the spheroid spinning rate about its minor axis. Furthermore, They corroborated the validity of quasi-static approximation within Strouhal numbers (associated with spinning motions about the spheroid minor axis) less than 0.1, provided the Reynolds number is smaller than 1.5×10^5. In another study, Candelier *et al.* [125] demonstrated that a spherical microswimmer (squirmer) experiences an inertial torque similar to a spheroid settling in a quiescent flow that causes it to orient broadside. They utilized a theoretical analysis based on the calculations of Cox [126], which are valid for a passive particle settling in a quiescent fluid. This inertial torque arises from the asymmetry in the flow patterns caused by the squirmer's swimming and tends to rotate the spherical squirmer so that its swimming and settling velocities are aligned in opposite directions.

When it comes to the settling of straight rods, once the orientation of a straight rod shifts away from the broadside position, it undergoes rotational motion during settling due to the effect of inertial torque at low Reynolds numbers [99–101, 117]. This phenomenon affects the rod settling velocity and has been investigated in several studies. The inertial settling of a straight cylinder with an arbitrary initial orientation was numerically studied by Pierson [123]. They investigated the validity of the quasi-steady assumption in the dynamic equations of rod settling, which involves neglecting the term ΩU, where Ω and U represent the spinning rate and settling velocity of the rod, respectively. They demonstrated that this assumption is valid for a broad range of Reynolds numbers calculated based on the rod diameter, up to $\mathrm{Re} = 1$ for rod aspect ratio between 10 and 30 and up to $\mathrm{Re} = 10$ for rod aspect ratios smaller than 10. This assumption simplifies the analysis, allowing the forces and torques on the particle to be modeled based solely on the instantaneous velocity and orientation of

the rod, rather than accounting for its entire motion history. However, for the quasi-steady assumption to remain valid, $\Omega L/U$ should be much smaller than 1, where L is the length of the cylindrical rod. Their results also show that even though the rod inertia does not influence the magnitude of settling and angular velocity, it is responsible for the horizontal orientation of the rods once they reach a stable position during their fall, particularly at larger inertia. Pierson *et al.* [127] studied the torque applied to a cylinder rotating about an axis perpendicular to its main axis, as shown in figure 2.12, within the cylinder aspect ratios lower than 15 and Reynolds numbers (calculated based on the cylinder tip velocity and diameter) smaller than 250. They determined the ratio of both shear stress and pressure contributions to the total torque, demonstrating that the pressure torque becomes more dominant as the cylinder aspect ratio increases. They also derived an equation to determine the cylinder tip velocity ratio, defined as the ratio of the cylinder tip velocity to its settling velocity when the cylinder is freely falling and rotating in the vertical plane, given by

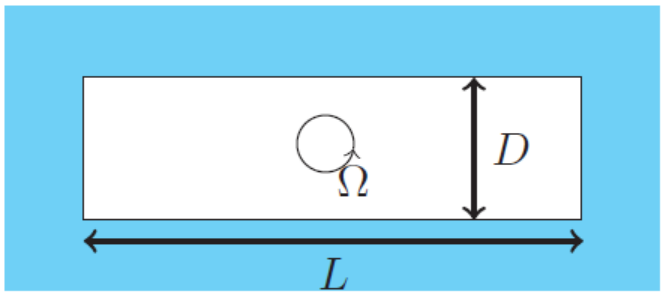

Figure 2.12: Sketch of the rotating cylinder studied by Pierson *et al.* [127]. Ω, L, and D represent the cylinder spinning rate, length, and diameter, respectively. Reprinted with permission from Pierson *et al.* [127].

$$\frac{\Omega L}{U} = 1.1\left(\frac{\mathrm{Re}}{AR}\right)^{0.4}, \tag{2.32}$$

where Ω is the cylinder spinning rate, L is the cylinder length, U is the cylinder settling velocity, Re is calculated based on the velocity of the cylinder tip ($\Omega L/2$) and the cylinder diameter (D), and AR is the cylinder length-to-diameter ratio. Cabrera *et al.* [128] performed

a set of drop experiments with tungsten cylindrical rods with aspect ratios of 8 and 16 in pure glycerin. They measured the torque applied to the rods during settling using a three-dimensional PTV system and compared their results with predictions from slender rod and spheroid theories. They found that the torques predicted by the slender-rod theory are larger than the measured values for the two studied aspect ratios, while the formula derived for a spheroid provides a more accurate estimate for the aspect ratio of 16.

Background turbulence in the fluid can also cause the rods to rotate while settling, leading to a change in their orientation angle and, consequently, their settling velocity. Roy *et al.* [129] studied the settling of fibres and triads in isotropic turbulent flow through theoretical and experimental analyses. They based their theoretical analysis on the balance between the torque arising from turbulence, which tends to deviate the rod's orientation from the broadside, and the inertial torque, which aligns the rod with this orientation. They obtained variations in the variance of the orientation angle at different values of the settling factor (S_F), defined as the ratio of the Kolmogorov time scale to the particle relaxation time. Lower values of the settling factor ($S_F < 0.1$) correspond to a greater influence of turbulence, while higher values of the settling factor ($S_F \gg 0.1$) are associated with the dominance of inertial torque over turbulence effects. As shown in figure 2.13, both fibres and triads exhibit an isotropic distribution of orientation at low settling factors, characterized by a constant variance in orientation angle, which is followed by a decaying transition to a horizontal orientation based on a power law. The variations in orientation variance with the settling factor were shown to be independent of the particle shape (fibre or triad) and the Taylor Reynolds number.
In another study, Xiao *et al.* [30] developed a new model to estimate the settling velocity of round and flat fibres in a turbulent flow. Their results demonstrate that fibres with smaller diameters are more affected by turbulence due to their lower inertia, which leads to variations in their inclination angle and an increase in settling velocity compared to settling in a quiescent fluid. The impacts of turbulence were shown to be negligible for round fibres with diameters of 10 and 20 μm and aspect ratios ranging between 5 and 50. However, due

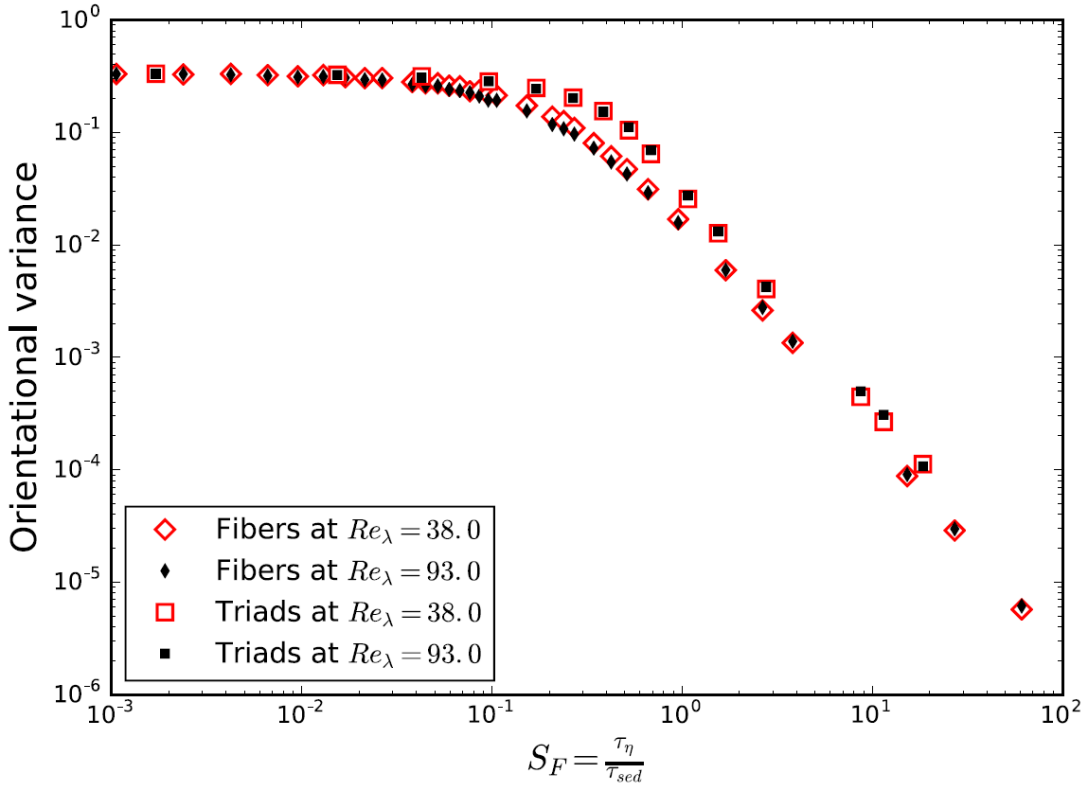

Figure 2.13: Orientational variance of fibres and triads as a function of settling factor (S_F) at different Taylor Reynolds numbers (Re_λ). τ_η is the Kolmogorov time scale and τ_{sed} is the fibre relaxation time. Reprinted with permission from Roy *et al.* [129].

to the dominance of turbulence over fibre inertia, flat fibres exhibit an increase in settling velocity of up to 30% when exposed to turbulence.

2.5 Research Significance and Novelty

Based on the literature reviewed in this chapter, it is concluded that the settling behavior of cylindrical particles at low Reynolds numbers, particularly those with diverse morphologies, has not been extensively studied. The range of aspect ratios examined for straight cylindrical rods or fibres is limited; consequently, the effect of finite cylinder length on settling behavior has not been thoroughly investigated. Additionally, various fibre morphologies, such as curved and bent shapes, have not been adequately explored.

The present research focuses on the influence of a wide range of aspect ratios and morphologies, including curved, V-, U-, and S-shaped geometries, on the settling behavior of rods, specifically their trajectory, orientation, and terminal velocity. Studies on the impact of curvature on rod settling behavior are limited in the literature, and the effects of V-, U-, and S-shaped morphologies have not been previously reported, despite the fact that such geometries are commonly observed in microfibre samples collected from atmospheric deposition and other applications, as outlined in Section 2.2. One of the main objectives of this study, as discussed in Chapter 1, is to develop new models for the drag coefficient of cylindrical rods that can be used to predict the terminal velocity of microfibres settling in a quiescent medium at low Reynolds numbers. For instance, by estimating the terminal velocity of microfibres settling in the atmosphere, it is possible to calculate their residence time and horizontal travel distance. This, in turn, allows atmospheric scientists to predict their trajectories and ultimate fate in the atmosphere.

Chapter 3

Experimental Facility and Methods

In this chapter, the materials selected for the experiments, the experimental setup utilized in this research, and the analysis methods are described. The analysis methods include the methods used for image analysis, the algorithm for stereoscopic calibration to convert pixel space into real-life space, and the analysis of the uncertainty in the data points.

3.1 Design of Experiments

This research aims to replicate the range of Reynolds numbers associated with the settling of plastic microfibres in the atmosphere. This range is estimated using a typical range of microfibre dimensions reported in the literature (100 μm $<$ fibre length $<$ 700 μm, 10 $<$ fibre aspect ratio $<$ 90, and 900 kg/m^3 $<$ fibre density $<$ 1400 kg/m^3), as described in chapter 2 [3, 14, 15, 22, 32, 106], along with the Henn's model given by equation 2.18. Figure 3.1 (a) and (b) show the contours of the calculated Reynolds number variation with the aspect ratio and length of the fibre for the lower and upper bounds of microfibre density observed in atmospheric microplastic depositions, 900 and 1400 kg/m^3, respectively. The results of these computations demonstrate that the atmospheric range of Reynolds number is smaller than 7, which the experiments in this study are designed to replicate.

Fluid dynamic viscosity as large as roughly 1000 times that of water can be provided by glycerin-water mixtures. Therefore, metal cylindrical rods at the millimeter scale, rather

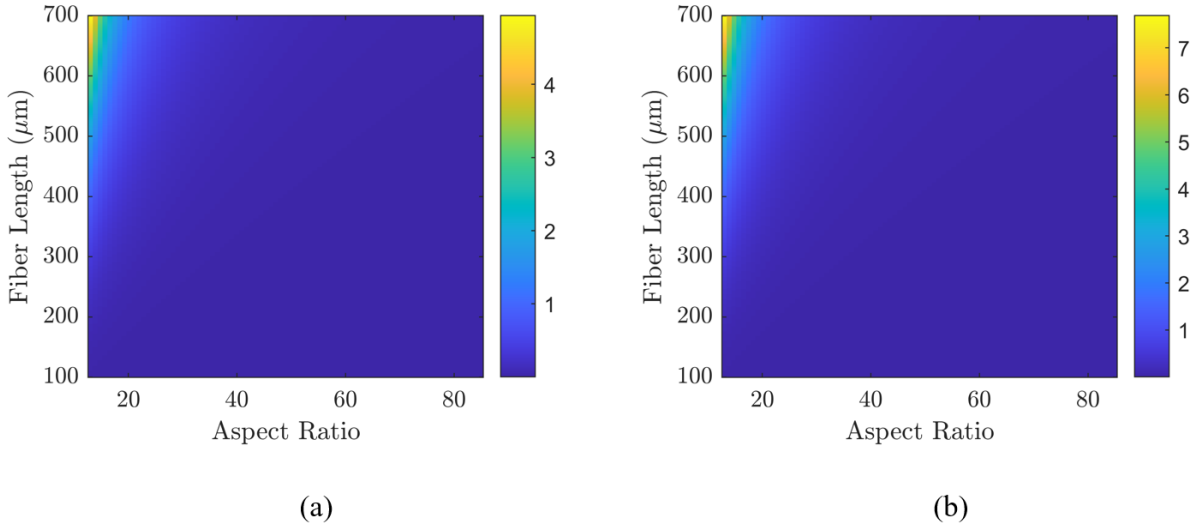

Figure 3.1: Contours of Reynolds number associated with atmospheric transport of microfibres computed using Henn's model [69] and typical range of fibres length and aspect ratio for the fibre density of (a) 900 kg/m^3 and (b) 1400 kg/m^3.

than the micrometer scale, can be dropped to exhibit the same Reynolds number range. This enables the tracking of the three-dimensional trajectory and orientation of these rods as they fall through the viscous liquid. The viscosity of glycerin mixture with different weight ratios at different temperatures has been calculated using Cheng's correlation [130]. The Reynolds number and settling velocity of cylindrical brass particles are estimated using Henn's model [69], as given by equation 2.18. According to the calculation results, brass and aluminum are chosen as the material of the cylindrical rods due to their greater densities, 8730 and 2710 kg/m^3, respectively, compared to the density of the glycerin mixture, ranging between 1207 and 1260 kg/m^3 for weight ratios of 80% and 100% (pure glycerin) at the temperature of 21°C, respectively. The Reynolds numbers associated with the fall of brass and aluminum rods in a water-glycerin mixture are estimated for three different glycerin weight ratios, 80%, 90%, and 100%, at the mixture temperature of 21°C using Henn's model [69], and are shown in the contours in Figure 3.2. The aspect ratio range selected for the cylindrical brass and aluminum particles includes the aspect ratios of typical microfibres collected from atmospheric

deposition, with $10 < AR < 90$ in this case. Moreover, a range of diameters between 0.41 and 2 mm is chosen based on the standard sizes of the brass rods provided by the manufacturers. According to these contours, a water-glycerin mixture with a glycerin weight ratio of 90% (Figure 3.2 (b) and (e)) is selected as the liquid in this study since it can cover a Reynolds numbers range (smaller than 5 and 25 for aluminum and brass, respectively) that is more aligned with the atmospheric settling of microfibres, corresponding to the range of $\mathrm{Re} < 7$.

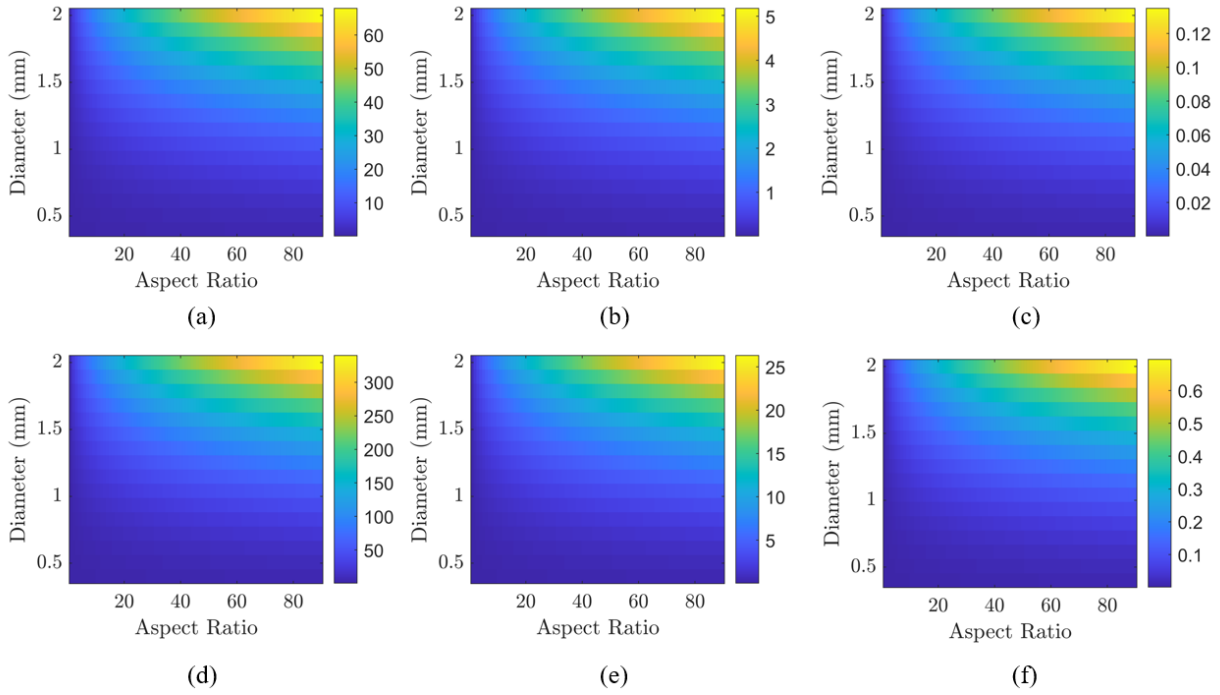

Figure 3.2: Reynolds number contours for aluminum and brass cylindrical particles falling at the temperature of 21°: panels (a), (b), and (c) show aluminum rods and glycerin weight ratios of 80%, 90%, and 100% respectively. panels (d), (e), and (f) show brass rods and glycerin weight ratios of 80%, 90%, and 100% respectively.

The Reynolds number range replicated in this study is based on microplastic fibres with maximum aspect ratios of 90 and fibre lengths as long as 700 μm. Within this range, the elasto-gravitational number, as discussed in Section 2.4.2, is determined to be less than 0.002 for the flexible fibres. Based on Marchetti's results [112], within this range of elasto-gravitational number, the deformation of a flexible fibre and its impact on the fibre terminal

velocity can be neglected. As a result, the fibres maintain their original shape and do not deform, rotate, and undergo variation in velocity [113, 114], which validates the assumption of rigid rods rather than flexible cylindrical geometries in this study.

3.2 Materials

In this research, the settling of rods with diverse shapes beyond the often idealized straight geometry, including curved and bent shapes (V-, U-, and S-shape), has been investigated. To analyze the impact of the diverse morphology of the rods, the results are compared to those of straight geometry with the same diameter and aspect ratio. Daramsing [49] also investigated a range of straight and curved rods, the results of which are included in this dissertation. However, in the present research, additional rods were added to extend the range reported by Daramsing [49]. This was needed to support the comparative analysis of the more complex shapes included in the present dissertation and the broader range of Reynolds numbers considered. Where included, results adopted from Daramsing's study will be clarified.

Figure 3.3 illustrates a schematic of the rod geometries previously mentioned. From left to right, this includes the straight, curved, and bent shapes (V-, U-, and S-shape). For the straight rods, L_C and D_C represent the total length and diameter. For the V-shaped rods, α_0 and L_P denote the bend angle and the projected length of the rod, respectively. The results of the V-shaped rods are compared with those for curved rods having the same length (L_C), diameter (D_C), and projected length (L_P). For these curved rods, θ_0 and ROC represent the arc angle and radius of curvature, respectively. For U-shaped and S-shaped rods, L_1 and L_2 denote the side arm and middle arm lengths, respectively. The uncertainty in the diameter of all rods is ± 0.05 mm. For straight rods, The aluminum rods, with a density of 2710 ± 66 kg/m^3, replicate very low Reynolds numbers ($\mathrm{Re} < 0.1$), whereas the brass rods, with a density of 8730 ± 49 kg/m^3, reproduce intermediate and higher Reynolds numbers ($\mathrm{Re} > 0.1$) within $0 < \mathrm{Re} < 5$. The rods were all cut using a jeweler's saw blade, with an

uncertainty of 0.1 mm in the rod length, and sanded flat at both ends.

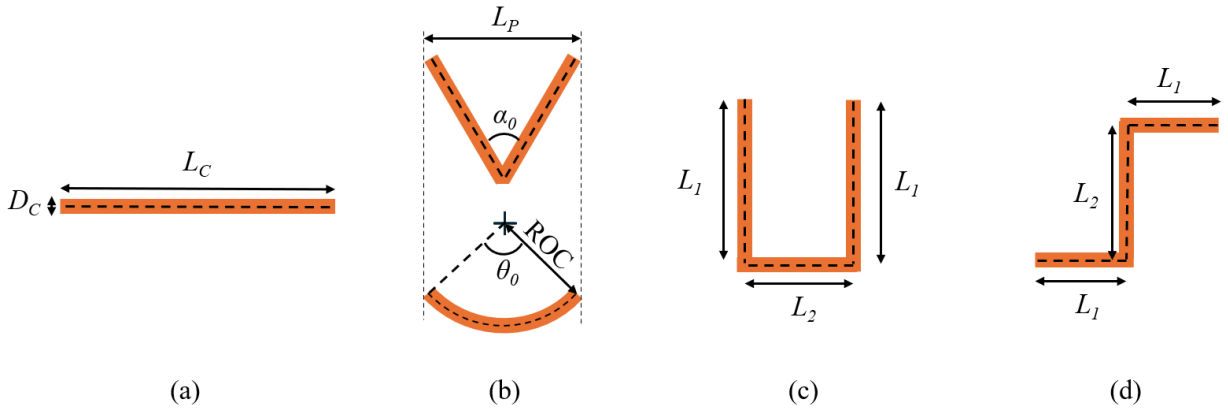

Figure 3.3: Schematic representations of the rod geometries studied in this research: (a) straight rod with length L_C and diameter D_C; (b) V-shaped rod with a bend angle α_0, projected length L_P, and a curved rod with the same projected length (L_P), radius of curvature ROC, and arc angle θ_0; (c) U-shaped rod with side arm length L_1 and middle arm length L_2; (d) S-shaped rod with side arm length L_1 and middle arm length L_2.

3.2.1 Straight and Curved Rods

Table 3.1 presents the material, density, and geometric dimensions of the straight and curved rods, along with their corresponding range of Reynolds numbers obtained from the experiments. All brass straight and curved rods included in this table were studied by Daramsing [49]. However, in this Ph.D. research, these results are extended by incorporating aluminum rods to expand the range of Reynolds numbers. The results of both brass and aluminum rods are included to improve the range and accuracy of the model predicting the terminal velocity of straight, curved, and V-shaped rods. In table 3.1, the rod aspect ratio, denoted by AR, is defined as the ratio of the rod length to its diameter.

3.2.2 V-Shaped and Curved Rods

Table 3.2 shows the material, density, and geometric dimensions of the V-shaped rods studied in this research. Furthermore, the range of Reynolds numbers obtained in the experiments, as

Table 3.1: The properties of the straight and curved rods investigated in this study. All straight and curved brass rods in this table were studied by Daramsing [49].

Geometry	Material	Density (kg/m^3)	D_C (mm)	AR	ROC (mm)	Re (based on D_{eq})	Re (based on L_C)
Straight	Aluminum	2710 ± 118	0.41	30, 40, 60, 90, 120		0.03 to 0.07	0.28 to 1.41
Straight	Brass	8730 ± 49	0.50	3, 5, 10, 20, 30, 60, 90, 120		0.07 to 0.41	0.13 to 8.72
Straight	Brass	8730 ± 49	1.00	3, 5, 10, 20, 30, 45, 60		0.38 to 1.75	0.70 to 23.45
Straight	Brass	8730 ± 49	1.50	3, 5, 10, 20		1.19 to 3.14	2.16 to 20.24
Straight	Brass	8730 ± 49	2.00	3, 5, 10, 15		2.49 to 5.35	4.52 to 28.41
Curved	Aluminum	2710 ± 118	0.41	60	19.9, 27.3, 37.5	0.040 to 0.041	0.53 to 0.55
Curved	Aluminum	2710 ± 118	0.41	90	19.9, 27.3, 37.5	0.056 to 0.060	0.98 to 1.05
Curved	Brass	8730 ± 49	0.50	60	19.9, 27.3, 31.7 - 37.5	0.32 to 0.35	4.34 to 4.65
Curved	Brass	8730 ± 49	0.50	90	19.9, 27.3, 31.7, 37.5	0.38 to 0.43	6.66 to 7.52
Curved	Brass	8730 ± 49	1.00	30	19.9, 27.3, 31.7, 37.5	1.38 to 1.45	11.65 to 12.25
Curved	Brass	8730 ± 49	1.00	45	19.9, 27.3, 31.7, 37.5	1.62 to 1.89	17.87 to 20.84

discussed in Chapter 4, is included. The V-shaped rods were made by bending straight rods at their midpoint to a specific angle, referred to as the bend angle in this study (α_0 in figure 3.3). α_0 ranges between 45 and 135 degrees. The resulting projected length (L_P in figure 3.3) is within ± 0.1 mm for the V-shaped rods at the reported α_0 and is calculated from

$$L_P = L_C \times \sin(\alpha_0/2). \tag{3.1}$$

Table 3.2: The properties of the straight and V-shaped rods investigated in this study.

Geometry	Material	Density (kg/m^3)	D_C (mm)	AR	α_0 (°)	Re (based on D_{eq})	Re (based on L_C)
Straight	Brass	8730 ± 49	0.50 ± 0.05	20, 30, 60, 90		0.19-0.38	1.21-6.66
Straight	Brass	8730 ± 49	1.0±0.05	10, 20, 30, 45		0.83-1.62	3.37-17.87
Straight	Aluminum	2710 ± 66	0.51 ± 0.05	30, 45, 60, 90, 120		0.05-0.09	0.39-1.94
V-shaped	Brass	8730 ± 49	0.50 ± 0.05	20, 30, 60, 90	45, 70, 90, 110, 135	0.21-0.62	1.32-10.86
V-shaped	Brass	8730 ± 49	1.0±0.05	10, 20, 30, 45	45, 70, 90, 110, 135	0.90-2.62	3.65-29.01
V-shaped	Aluminum	2710 ± 66	0.51 ± 0.05	30, 45, 60, 90, 120	45, 70, 90, 110, 135	0.05-0.14	0.40-2.99

The curved rods were made with the same diameter, length, and projected area as the V-shaped rods for $D_C = 0.50$ mm. The total length of a curved rod is calculated from

$$L_C = \text{ROC} \times \theta_0 \tag{3.2}$$

The projected length for the curved rod can be calculated from

$$L_P = 2 \text{ ROC } \sin(\theta_0/2). \tag{3.3}$$

By eliminating ROC from equations 3.2 and 3.3, we will have

$$L_P\theta_0 - 2L_C\sin(\theta_0/2) = 0. \tag{3.4}$$

Knowing the L_C and L_P for a V-shaped rod, the arc angle (θ_0) for a curved rod with the same diameter, length, and projected area as the V-shaped rod can be determined from equation 3.4. Once θ_0 is calculated, ROC can be determined from equation 3.2 or 3.3. In this way, the curved rods are specified with the same L_P as each V-shaped rod. In this research, only the curved rods smaller than a half circle or with $\theta_0 < 180^\circ$ are studied. The curvature index, which measures how much the curved rod geometry deviates from a straight rod [36, 37, 50], can be calculated from

$$C = 1 - \frac{L_P}{L_C}. \tag{3.5}$$

Substituting equation 3.2 and 3.3 into equation 3.5 gives

$$C = 1 - \frac{2\sin(\theta_0/2)}{\theta_0}. \tag{3.6}$$

In equation 3.6, θ_0 varies between 0 and 180°. The Variation of C with θ_0 is illustrated in figure 3.4, showing that variation of C is confined to the range of 0 to 0.36. The values of 0 and 0.36 correspond to a straight rod and a half-circle curved rod, respectively.

The ratio of L_P/L_C, denoted by β, can also be determined for a V-shaped rod, with L_P calculated from equation 3.1, which results in $\beta = \sin(\alpha_0/2)$. By equating β between the curved and V-shaped rod, we have

$$\beta = \sin(\alpha_0/2) = 1 - C. \tag{3.7}$$

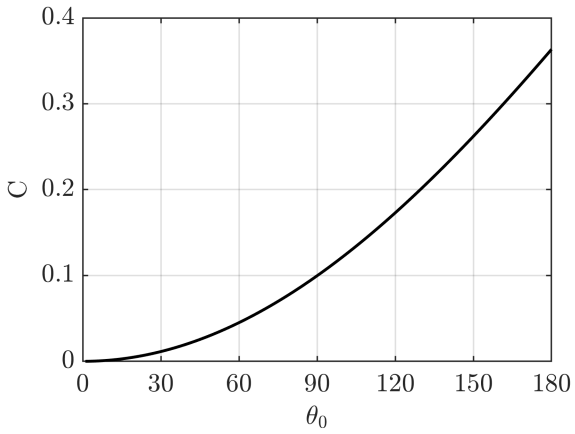

Figure 3.4: Variation of the curvature index of a curved rod (C) with arc angle (θ_0).

Given the range of variation for C, α_0 ranges between 80° and 180°. As a result, the curved rods with the same dimensions and projected area as the V-shaped rods are made only for V-shaped rods with $\alpha_0 = 80°, 85°, 90°, 110°,$ and 135°, $D_C = 0.50$ mm, and $AR = 60$ and 90 in this research. Table 3.3 shows a summary of the geometric parameters of the curved rods as well as the corresponding V-shaped rods with the same dimensions and projected area.

Table 3.3: The geometric parameters of the curved rods and the corresponding V-shaped rods with the same projected area. The rod diameter for all cases in this table is 0.50 mm.

AR	α_0 (°)	L_P (mm)	θ_0 (°)	ROC (mm)	C	β
60	80	18.6	180	9.6	0.36	0.64
90	80	29.3	180	14.5	0.36	0.64
60	85	20.5	169	10.2	0.32	0.68
90	85	30.6	169	15.3	0.32	0.68
60	90	21.2	159	10.8	0.29	0.71
90	90	31.8	159	16.2	0.29	0.71
60	110	24.5	123	13.9	0.18	0.82
90	110	37.3	123	21.6	0.18	0.82
60	135	27.9	78	22.8	0.08	0.92
90	135	41.5	78	32.5	0.08	0.92

3.2.3 U-Shaped Rods

Table 3.4 summarizes the materials, dimensions, and Reynolds number ranges for the U-shaped rods and the straight rods used for comparison in this study. The U-shaped rods were fabricated with aspect ratios ranging from 30 to 90, and with middle arm length ratios ($\alpha = L_2/L_C$), defined as the ratio of the middle segment length (L_2) to the total rod length (L_C), varying between 0.15 and 0.80.

3.2.4 S-Shaped Rods

The materials, dimensions, and Reynolds number ranges of the U-shaped rods and the straight rods used for comparison are summarized in Table 3.5. The S-shaped rods have aspect ratios ranging from 30 to 90 and middle arm length ratios varying between 0.11 and 0.67.

3.3 Experimental Facility

This section describes the drop chamber, the viscous fluid used within it, the custom-designed imaging system for capturing the fall trajectories of the rods, and the rheometer employed to measure the viscosity of the glycerin mixture.

3.3.1 Chamber and Image Acquisition System

A schematic of the chamber and the stereoscopic imaging setup employed in this research is shown in figure 3.5. The side and bottom walls of the chamber are made of clear acrylic sheets to allow for illuminating and capturing the fall trajectory of the rods within the chamber. The size of the chamber is 0.25 m in width and length and 1.0 m in height. The chamber is filled with a water-glycerin mixture with a glycerin weight ratio of 90%. Two 10-watt LED lights are positioned behind two perpendicular sides of the chamber to illuminate the glycerin mixture inside. Additionally, two monochromatic Kaya Iron 250 CXP cameras with 8-bit resolution and Basler C-Mount lenses, each with a focal length of 50 mm, capture images simultaneously from two perpendicular sides of the chamber, encompassing the ZY and XY

Table 3.4: The density, dimensions, and Reynolds numbers of the U-shaped and straight rods used for comparison.

Geometry	Material	Density (kg/m^3)	D_C (mm)	AR	α	Re (based on D_{eq})	Re (based on L_C)
U-Shaped	Brass	8730	0.50	30, 40, 50, 60, 90	0.33	0.43-0.65	3.60-11.40
U-Shaped	Brass	8730	0.50	60	0.11, 0.20, 0.33, 0.50, 0.67, 0.75, 0.80	0.44-0.53	5.87-7.07
U-Shaped	Brass	8730	0.50	90	0.11, 0.20, 0.33, 0.50, 0.67, 0.75, 0.80	0.54-0.66	9.55-11.51
U-Shaped	Brass	8730	0.81	30, 40, 50, 60, 70, 90	0.33	1.18-1.65	9.98-28.96
U-Shaped	Brass	8730	0.81	60	0.20, 0.33, 0.50, 0.67, 0.75, 0.80	1.46-1.55	19.51-20.80
U-Shaped	Brass	8730	0.81	90	0.20, 0.33, 0.50, 0.67, 0.75, 0.80	1.64-1.78	28.80-31.23
U-Shaped	Aluminum	2710	1.02	30, 40, 50, 60, 90	0.33	0.54-0.77	4.58-13.43
U-Shaped	Aluminum	2710	0.81	60	0.15, 0.20, 0.33, 0.50, 0.67, 0.75	0.61-0.69	8.12-9.25
U-Shaped	Aluminum	2710	1.02	90	0.15, 0.20, 0.33, 0.50, 0.67, 0.75	0.68-0.74	11.97-13.03
Straight	Brass	8730	0.50	30, 40, 50, 60, 90		0.33-0.54	2.80-9.44
Straight	Brass	8730	0.81	30, 40, 50, 60, 70, 90		0.99-1.49	8.33-26.16
Straight	Aluminum	2710	0.81	30, 40, 50, 60, 90		0.39-0.62	3.29-10.88

Table 3.5: The dimensions and Reynolds numbers of the S-shaped and straight brass rods used for comparison.

Geometry	Material	Density (kg/m^3)	D_C (mm)	AR	α	Re (based on D_{eq})	Re (based on L_C)
S-Shaped	0.50	Brass	8730 ± 49	30, 40, 50, 60, 90, 120	0.33	0.25-0.44	2.14-9.43
S-Shaped	Brass	8730 ± 49	0.50	60	0.11, 0.20, 0.33, 0.50, 0.67	0.34	4.55
S-Shaped	Brass	8730 ± 49	0.81	30, 40, 50, 60, 90	0.33	0.89-1.39	7.54-24.34
S-Shaped	Brass	8730 ± 49	0.81	60	0.11, 0.20, 0.33, 0.50, 0.67	1.19	15.95
S-Shaped	Brass	8730 ± 49	1.0	30, 40, 50, 60, 90	0.33	1.44-2.14	12.15-37.46
S-Shaped	Brass	8730 ± 49	1.0	60	0.11, 0.20, 0.33, 0.50, 0.67	1.88	25.15
Straight	Brass	8730 ± 49	0.50	30, 40, 50, 60, 90, 120		0.25-0.44	2.14-9.43
Straight	Brass	8730 ± 49	0.81	30, 40, 50, 60, 90		0.89-1.39	7.54-24.34
Straight	Brass	8730 ± 49	1.0	30, 40, 50, 60, 90		1.44-2.14	12.15-37.46

planes, as illustrated in figure 3.5. Both side cameras are placed at a distance of 0.9 m from the side acrylic wall of the chamber. The third camera, equipped with a Basler C-mount lens with a focal length of 25 mm and sharing the same specifications as the other two side cameras, is placed underneath the chamber at a distance of 0.60 m from the bottom acrylic wall. The two side cameras are used to capture the fall trajectory of the rods as they approach the bottom of the chamber and reach their terminal velocities. The bottom camera captures the potential spinning motions of the rods, which is observed for S-shaped rods, around the vertical axis, represented as the Y axis in figure 3.5. The height of the field of view for the side cameras is 15 cm, while the bottom camera can capture an area covering the entire bottom acrylic wall. All cameras are connected to a computer via a Komodo II four-channel CoaxPress 12 G Frame Grabber. Using a software package called Vision Point, the cameras

are synchronized and the image acquisition system is operated. Owing to the sensitivity of the glycerin mixture density and viscosity to temperature, a T-type thermocouple is placed inside the mixture to monitor the temperature. The mixture was homogeneous, and the samples taken over several weeks maintained consistent viscosity within the measurement uncertainty.

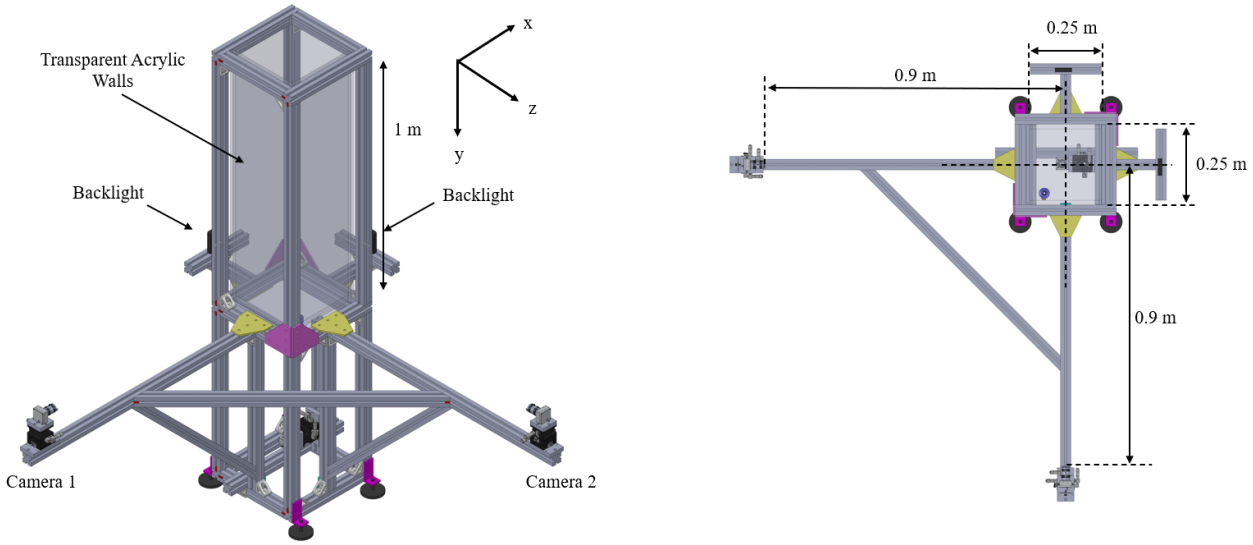

Figure 3.5: Schematics of the chamber and image acquisition system used in this research. The left figure shows an isometric view of the chamber, cameras, and backlighting. The right figure shows a top view of the chamber with the chamber dimensions and the distance between the tank and the cameras.

3.3.2 Rheometer

The viscosity of the glycerin mixture is measured using the Discovery HR-3 hybrid rheometer, as shown in Figure 3.6, which is recommended for low to medium viscosity fluids. In this setup, the system comprises three primary elements: a concentric cylinder, securely attached to the rheometer's base via magnetic locking; a concentric cup, which holds roughly 22 mL of the fluid sample; and a conical rotor, fastened at the top of the rheometer, spinning at different speeds to achieve varying shear rates. A sterile syringe is employed to transfer glycerin mixtures from the sample container into the concentric cup. The temperature of the

cup is regulated by fluid circulating through two tubes attached to the concentric cylinder. To measure the viscosity of the water-glycerin mixture, the mixture undergoes a range of shear rate between 0 and 200 1/s with an increment of 10 1/s. The diameter of the concentric cup is 30.4 mm, and the operating gap between the rotor and the cup is 5.90 mm. The soak time was set to 180 s to ensure thermal balance between the cup, rotor, and the mixture. Viscosity measurement was performed for 30 seconds for each shear rate and the "linear sweep" method has been employed to measure the viscosity.

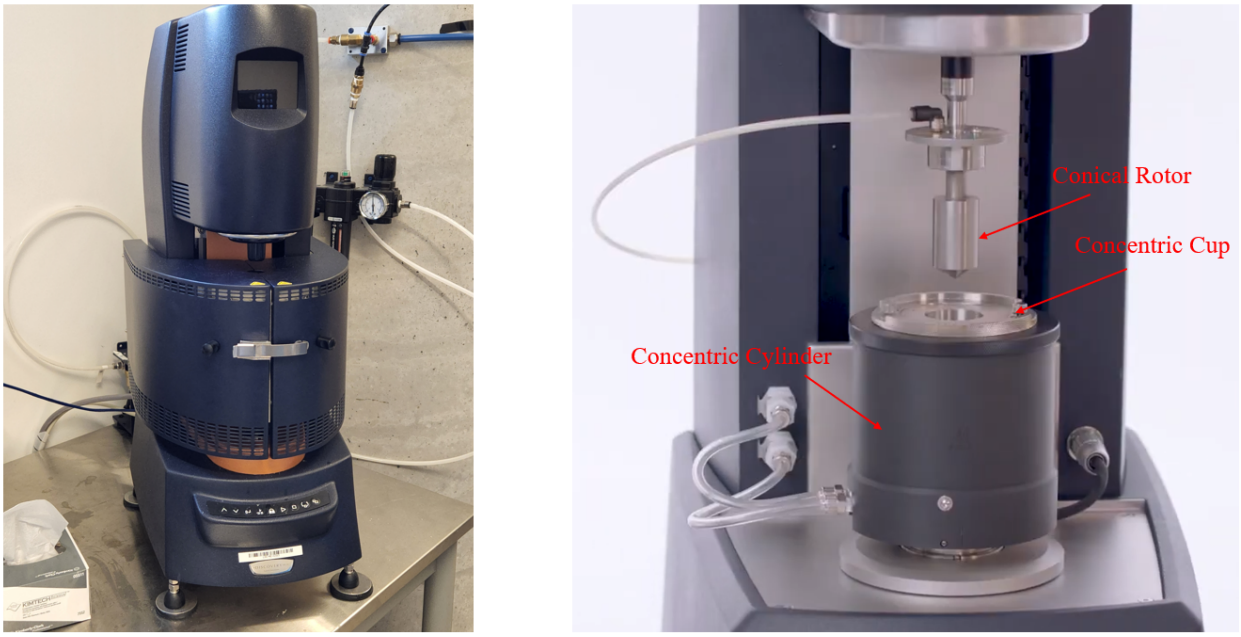

(a) (b)

Figure 3.6: (a) The Discovery HR-3 Hybrid Rheometer, (b) Conical rotor, concentric cup, and cylinder mounted on the rheometer to measure the viscosity of water-glycerin mixture.

To evaluate the accuracy of the viscosity measurements obtained using the rheometer, the viscosity of a reference fluid, N75, provided by Cannon Instruments, was measured and compared with the manufacturer's reference value. Figure 3.7 illustrates the viscosity of the N75 fluid across shear rates ranging from 10 to 200 s^{-1} at a temperature of 20°, along with the reference value of 0.1669 Pa·s. The average viscosity measured over this shear rate range is 0.1660 Pa·s, indicating a deviation of 0.56%. This deviation will be considered in the error

analysis for the calculations of the Reynolds number and drag coefficient, as discussed in Section 3.4.4.

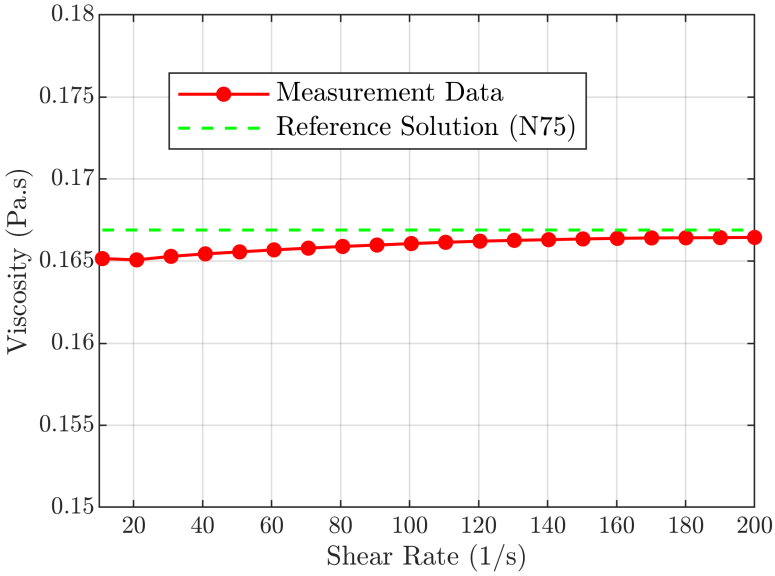

Figure 3.7: Variations in the viscosity of the reference N75 solution with shear rate, measured by the HR-3 Hybrid rheometer at 20 °C. Data markers and the dashed line represent the measured data points and the reference value, respectively.

The viscosity of a water-glycerin mixture with a glycerin weight ratio of 90%, used in the experiments of this research, was measured at a temperature of 21 °C. Figure 3.8 presents the measured viscosity across shear rates ranging from 10 to 200 s^{-1} and compares the data points with results obtained from Cheng's empirical equation [130]. The average measured viscosity over this shear rate range is 0.2160 Pa·s, showing a deviation of 2.48% from the value predicted by Cheng's correlation (0.2107 Pa·s) [130].

3.4 Analysis Methods

This section outlines the methods used to analyze the images captured by the cameras and to convert pixel coordinates into real-world locations through stereoscopic calibration.

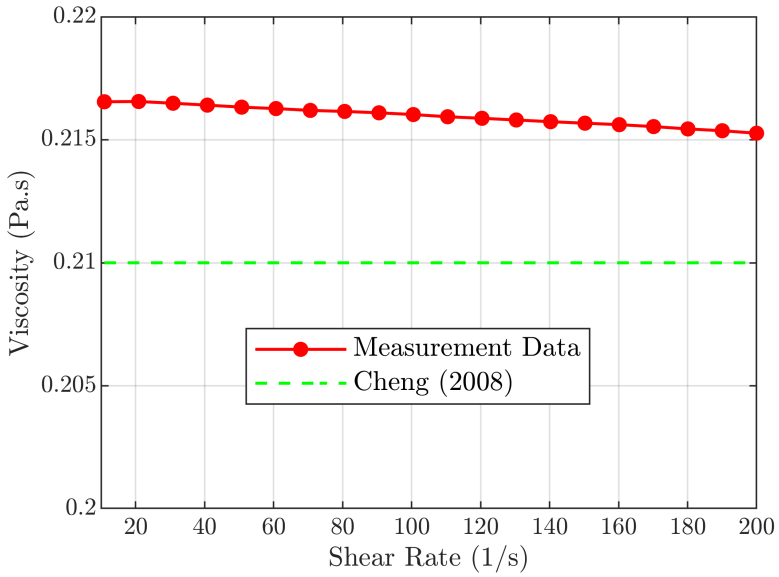

Figure 3.8: Variations in the viscosity of a water-glycerin mixture with a glycerin weight ratio of 90% with shear rate, measured by the HR-3 Hybrid rheometer at 21 °C. The data markers and the dashed line represent the measured data points and the value calculated from Cheng's correlation [130], respectively.

Additionally, the approach employed to quantify the uncertainty of the variables calculated in this research is elaborated.

3.4.1 Image Analysis

The images captured by the two side cameras are analyzed using a custom script in MATLAB to determine the pixel locations of the key points of the rod geometry along the rod fall trajectory. These key points include the centroid and two endpoints for all rod geometries, the midpoint for the V-shaped rod, and the two corner points for the U-shaped and S-shaped rods. The image processing includes binarizing, inverting, and detecting the key points, as illustrated in figure 3.9. These steps are applied to the images from both side cameras. The key points of the rod geometry are determined using *regionprops* and *pgonCorners* functions in MATLAB.

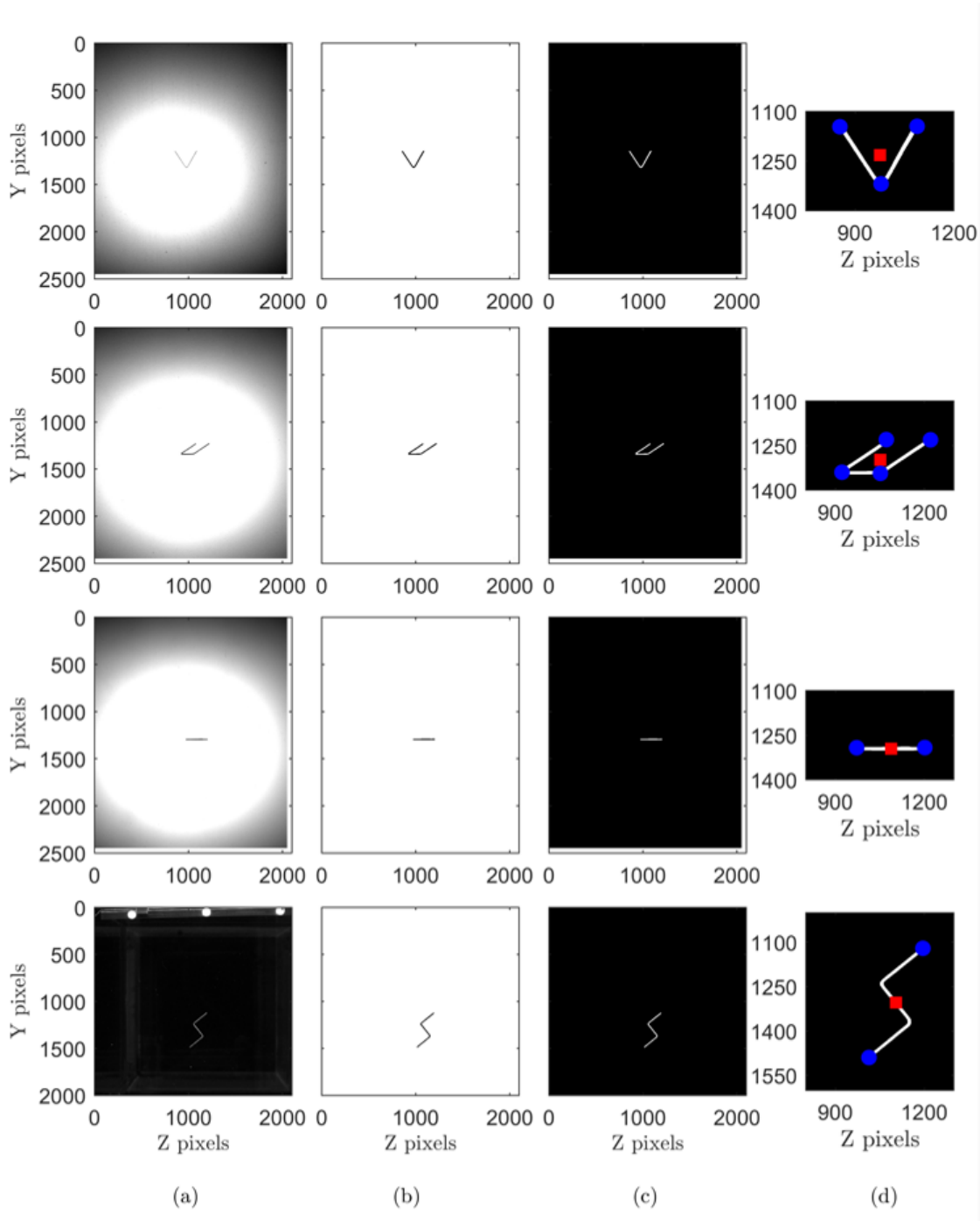

Figure 3.9: Image analysis steps: (a) original images, (b) binarized image, (c) inverted image, and (d) detection of the key points of the rod, including the centroid (red square), as well as the two end points, corner points for U- and S-shaped rods, and the midpoint for V-shaped rods (blue circles). The first and second rows show the V-shaped and U-shaped rods captured by a side camera. The third row shows the S-shaped rod from a side camera, while the last row shows a view captured by the bottom camera.

Based on experimental observations, S-shaped rods exhibit a spinning motion around the vertical axis while settling, which was captured by the bottom camera. To determine the spinning rate, image analysis was used to measure the angle between the line connecting the two rod endpoints and the horizontal axis. This angle, referred to as the orientation angle in this study, is illustrated in figure 3.10 (a) and denoted by γ. The variations in this angle were then plotted against time. The slope of the resulting straight-line plot with an R^2 value of 0.99 represents the spinning rate of the S-shaped rod. As an example, figure 3.10 (b) shows the variations of the orientation angle with time for an S-shaped rod with $D_C = 0.50$ mm, $AR = 60$, and $\alpha = 0.33$. The spinning rate of the rod in this case is 1.78 deg/s.

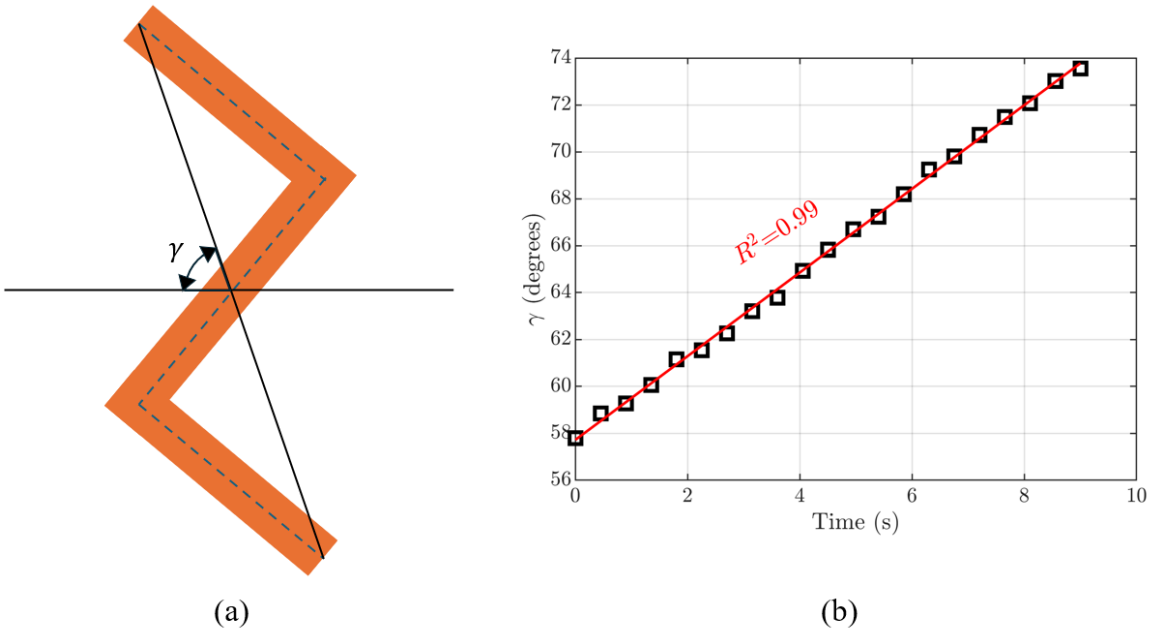

Figure 3.10: (a) Orientation angle of an S-shaped rod, denoted by γ, from a bottom view,(b) Variation of rod orientation angle with time for an S-shaped rod with $D_C = 0.50$ mm, $AR = 60$, and $\alpha = 0.33$. A straight line with $R^2 = 0.99$ and a slope of 1.78 deg/s is fitted to the data points.

3.4.2 Stereoscopic Calibration

The key points of the rod geometry can be located in pixels through the analysis of the images captured by the two cameras as the rod falls within the water-glycerin mixture. In

order to convert the centroid location from pixel space into real-life space, a three-dimensional calibration is required [131–133]. In this research, a mapping method similar to the approach adopted by Soloff's [131] is used. The displacement of the particle centroid between two consecutive images, measured in pixels, can be converted to real-life dimensions, measured in millimeters, using matrix mapping equations, given by

$$\begin{bmatrix} \Delta z \\ \Delta y \end{bmatrix}_{\text{camera 1}} = \begin{bmatrix} F_{11} & F_{12} \\ F_{21} & F_{22} \end{bmatrix} \begin{bmatrix} \Delta X_1 \\ \Delta X_2 \end{bmatrix}_{\text{camera 1}} \tag{3.8}$$

and

$$\begin{bmatrix} \Delta x \\ \Delta y \end{bmatrix}_{\text{camera 2}} = \begin{bmatrix} F'_{11} & F'_{12} \\ F'_{21} & F'_{22} \end{bmatrix} \begin{bmatrix} \Delta X_1 \\ \Delta X_2 \end{bmatrix}_{\text{camera 2}}. \tag{3.9}$$

Equation 3.8 corresponds to camera 1 and equation 3.9 corresponds to camera 2 as shown in figure 3.11. In these two equations, the real-life displacement of the particle in millimeters (left-hand side of the equation) is calculated by multiplying the mapping matrix by the particle displacement in pixels (right-hand side of the equation). Δx, Δy, and Δz represent the displacements of the rod centroid in millimeters along the three coordinate system directions, as shown in figure 3.11, ΔX_1 and ΔX_2 are the horizontal and vertical displacement of the rod in pixels in the images, and F and F' are the elements of the mapping matrices. The elements of the mapping matrices should be determined from the three-dimensional calibration process.

To perform the calibration, a grid is placed at an angle of 45 degrees relative to the chamber sides. The grid utilized in this study has a circle pattern with 59 rows and 60 columns and a spacing of 2 mm between adjacent centroids, as shown in figure 3.11 (a). All purely horizontal and vertical displacements between the adjacent circles in this grid are considered and plugged into equations 3.8 and 3.9 to determine the values of F and F' in the mapping matrices as a function of the location on the calibration grid.

For example, consider a purely horizontal displacement between two arbitrary adjacent circles (circle 1 and circle 2), in which the centroid of circle 1 is at a horizontal location of $X_{1,\text{camera2}}$ (known as the depth of the image) and a vertical location of X_2 (the average

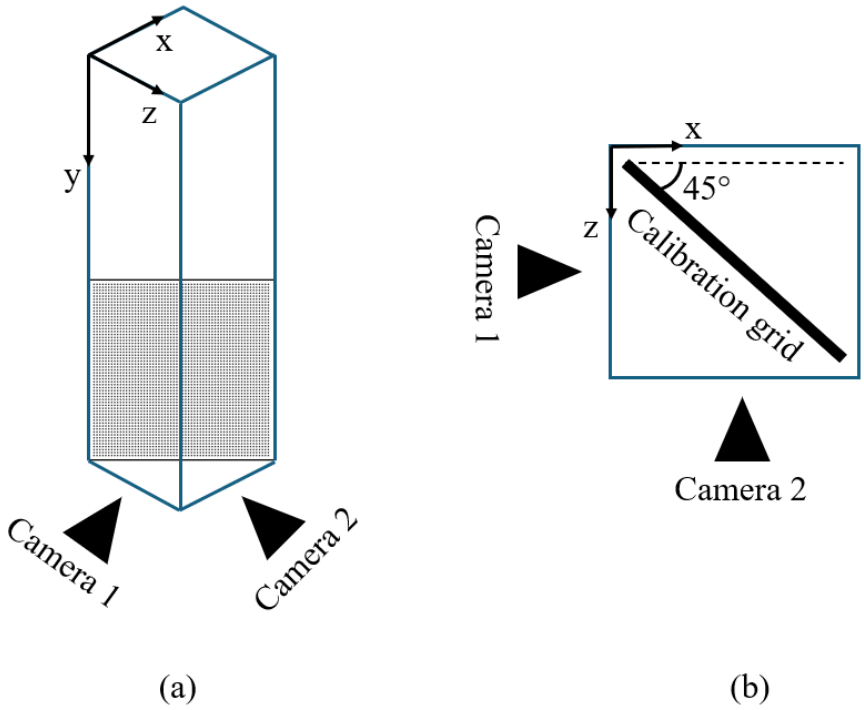

Figure 3.11: (a) Isometric and (b) top view of the calibration grid placed inside the chamber.

of the vertical locations viewed by two cameras to reduce uncertainty). For the mentioned horizontal displacement, equation 3.8 for camera 1 can be simplified to

$$F_{11} = \frac{L \cos 45^\circ}{\Delta X_{1,\text{camera1}}} \tag{3.10}$$

and

$$F_{21} = 0. \tag{3.11}$$

where L is the spacing between the centroids of two adjacent circles on the grid. Similarly, if a purely vertical displacement between the centroids of two consecutive circles is considered, F_{11} and F_{22} can be computed from

$$F_{12} = 0 \tag{3.12}$$

and

$$F_{22} = \frac{L}{\Delta X_{2,\text{camera1}}} \tag{3.13}$$

The values of F' for camera 2 in equation 3.9 can be obtained using a similar approach as explained above for camera 1. It should be noted that the depth of the image for camera 2 is the horizontal location of the same circle centroid in the image captured by camera 1.

The obtained values for F and F' are valid only for displacements between circles 1 and 2 with the starting point located at the image depth of X_1 and average vertical location of X_2. To calibrate the space occupied by the calibration grid, the values of F and F' (mapping matrices) should be determined for all the circles in the calibration grid. As a result, F and F' values will be a function of image depth and the vertical location of the point under investigation. Four fifth-order polynomial correlations are fitted to the nonzero elements of the mapping matrix (F_{11}, F_{22}, F'_{11}, and F'_{22}) to correlate their values with the corresponding image depth and vertical location. The resulting mapping matrices are then used to determine the real-life displacements of the rod's key points using equations 3.8 and 3.9.

3.4.3 Determination of Settling Velocity

The settling velocity of a rod is calculated by dividing the vertical displacement of its centroid between consecutive images, obtained using the method described in Section 3.4.2, by the time interval between these images, which corresponds to the inverse of the camera frame rate. In the current research, the variations in the rod settling velocities within the last 15 cm of its captured trajectory, which falls within the field of view of the two side cameras, do not exceed 1% of the average velocity. This demonstrates negligible variations in the rod velocity and insignificant effects of the chamber bottom wall on the rod velocity within this area. The terminal velocity of the rod is calculated by averaging the settling velocities over the last 15 cm of its captured trajectory [50, 52].

Furthermore, Brenner's model [134] is employed to consider the influence of the bounded

side walls of the chamber on the rod terminal velocity. Based on this model, the terminal velocity of the rod in an unbounded medium is calculated from

$$V_\infty = \frac{V_S}{\alpha'}, \tag{3.14}$$

where V_∞ and V_S represent the terminal velocity of the rod within an unbounded medium and the bounded chamber, respectively. The coefficient α' is calculated from

$$\alpha' = 1 - \frac{1.4}{0.5 - \gamma' - \ln(\mathrm{Re}_\infty/8)} \frac{L_C}{D}, \tag{3.15}$$

where γ' is Euler-Mascheroni constant (≈ 0.577), Re_∞ is the rod Reynolds number based on the terminal velocity of an infinite cylinder with a diameter of D_C, L_C is the rod length, and D is the diameter of the chamber cross-section. In this research, the terminal velocity obtained from the model by Khalili and Liu [103] is used to calculate Re_∞. Additionally, D is considered as the average of the chamber's diagonal and side lengths. The average value obtained for V_S/V_∞ is 0.98. As a result, an uncertainty of 2% has been considered for the effects of bounded walls on the rod velocity. Moreover, to address the repeatability of the experiments and variations in rod manufacturing, each drop test is repeated at least five times using at least three different samples of manufactured rods. An average uncertainty of 2% is calculated to take these factors into account.

3.4.4 Uncertainty Analysis

The uncertainty of the dependent variables in this research is calculated from

$$\sigma_R = \sqrt{\sum_{i=1}^{N} \left(\frac{\partial R}{\partial x_i} \sigma_{x_i} \right)^2}, \tag{3.16}$$

where R is a dependent variable, x_i is an independent variable, σ_R is the uncertainty of R, and σ_{x_i} is the uncertainty of x_i [135, 136]. The uncertainties of the dimensionless variables in this research, Reynolds number (Re) and drag coefficient (C_D), depend on the length of the

cylindrical rod (L_C), the viscosity of the water-glycerin mixture (μ), the density of the rod (ρ), the terminal velocity of the rod (V_S), and the temperature of the water-glycerin mixture (T). Therefore, the uncertainties of Re and C_D as two dependent variables can be calculated from

$$\sigma_{\mathrm{Re}} = \sqrt{\left(\frac{\partial \mathrm{Re}}{\partial L_C}\sigma_{L_C}\right)^2 + \left(\frac{\partial \mathrm{Re}}{\partial \mu_f}\sigma_{\mu_f}\right)^2 + \left(\frac{\partial \mathrm{Re}}{\partial \rho_f}\sigma_{\rho_f}\right)^2 + \left(\frac{\partial \mathrm{Re}}{\partial V_S}\sigma_{V_S}\right)^2 + \left(\frac{\partial \mathrm{Re}}{\partial T}\sigma_T\right)^2} \quad (3.17)$$

$$\sigma_{C_D} = \sqrt{\left(\frac{\partial C_D}{\partial L_C}\sigma_{L_C}\right)^2 + \left(\frac{\partial C_D}{\partial \mu_f}\sigma_{\mu_f}\right)^2 + \left(\frac{\partial C_D}{\partial \rho_f}\sigma_{\rho_f}\right)^2 + \left(\frac{\partial C_D}{\partial V_S}\sigma_{V_S}\right)^2 + \left(\frac{\partial C_D}{\partial T}\sigma_T\right)^2} \quad (3.18)$$

The length of the cylindrical particles is measured using a caliper with an uncertainty of 0.1 mm. As described in Section 3.3.2, the uncertainty in measuring the fluid viscosity is 0.56%, determined by measuring the viscosity of a reference solution provided by the rheometer manufacturer. The uncertainty in rod density is calculated by measuring the density of the rods (measured mass of the particle divided by the rod volume) and comparing it with the density of its material, brass (8730 kg/m^3) or aluminum (2710 kg/m^3). These calculations resulted in mean standard deviations of 49 kg/m^3 for brass rods and 118 kg/m^3 for aluminum rods. Four different sources are considered in determining the uncertainty of the rod terminal velocity: the standard deviation of the calculated velocities over the last 15 cm of the fall trajectory of the rod, the error from the three-dimensional calibration (Section 3.4.2), the impact of the bounded wall, and the effects of the rod manufacturing. The calibration error is considered the root mean square (RMS) error in fitting the fifth-order correlation to the mapping matrix elements (F and F' values in equations 3.8 and 3.9) over the entire space covered by the calibration grid. As mentioned in Section 3.4.3, the errors arising from the bounding walls of the chamber, as well as rod manufacturing, are both determined to be 2%. The uncertainty in the temperature of the water-glycerin mixture is considered to be ± 0.1°C, which corresponds to the uncertainty of the thermocouple used in these experiments. The

resulting uncertainties in Reynolds number and drag coefficient, calculated from equations 3.17 and 3.18, along with the terminal velocity, are represented as error bars in the respective plots in the following chapters.

Chapter 4

Results: Settling of Straight and Bent Rods

Straight and bent (V-shaped and curved rods) were dropped into a quiescent water-glycerin mixture with a glycerin weight ratio of 90%. Their orientation and terminal velocities were investigated and compared under identical dimensions once a stable terminal velocity was achieved. This chapter discusses the results of the straight and bent rods.

4.1 Rod Orientation and 3D Trajectory

4.1.1 Straight Rods

The orientation of straight cylindrical rods along their fall trajectory was observed when they reached their terminal velocity. Figure 4.1 shows selected positions while a straight rod settles in the still fluid. In figure 4.1 (a) and (b), the rod centroid in the first frame (the topmost location of the rod in the 3D trajectory) is at the origin. The 3D calibration algorithm, as discussed in Section 3.4.2, was used to determine the real-life locations of the centroids and the two endpoints of the rod in all frames as it settles. The actual vertical field of view of the camera is 150 mm. The straight cylindrical rods remain oriented horizontally when dropped from an initial horizontal orientation, as shown in figure 4.1 (a) for the case with a diameter of 0.5 mm and aspect ratio of 60. However, a rod dropped from a vertical orientation will reorient itself horizontally, as shown in figure 4.1 (b) for the straight cylindrical rod with a

diameter of 1.5 mm and aspect ratio of 20. A larger diameter rod was used for this example, since smaller diameter rods (with slower settling velocity) take a greater distance to reorient. The steady-state orientation of the straight rods was shown to reach a horizontal orientation from either an initial horizontal or vertical orientation, which is consistent with past examples from the literature, (see Jayaweera and Mason [99] and Roy *et al.* [117] for example).

Figure 4.1 (c) illustrates the variation of the settling velocity of the rods shown in figure 4.1 (a) and (b) at different vertical locations along their trajectories. Once the straight rods reach their terminal velocity, their trajectory becomes entirely vertical. If the rods are dropped with an initial orientation other than horizontal at finite Reynolds numbers (Re $>$ 0.1), they will exhibit a horizontal drift along their trajectory while they reorient from their initial orientation to horizontal, as depicted in figure 4.1 (b). For visualization, figure 4.1 (c) displays only every fifth point from the rod trajectory. Based on the calculated uncertainty obtained from the calibration procedure, the maximum uncertainty of the location and velocity of the rod centroid are 1.5% and 1.6%, respectively. The span of the error bars is similar in extent to the data marker size shown in figure 4.1 (c) and omitted for clarity. The uncertainty in velocity arises from a combination of uncertainties due to calibration in location detection and a minor difference caused by the time differential between images.

According to McKnown and Malaika [101], slender rods with a Re (based on the volume-equivalent diameter) of less than 0.1 tend to maintain their initial orientation while settling. This means that if a long cylindrical rod is dropped at any angle, it will remain in the same position as it settles. However, it will also experience horizontal drift, as demonstrated in the study by Xu and Nadim [137]. For Re values above 0.1, particles tend to orient themselves in a stable position due to inertia, and for cylindrical rods, this position is horizontal [100, 101]. In this research,the straight rods stabilize in a horizontal position, as illustrated in figure 4.1 (a) and (b). For the cases in this study where Re values were less than 0.1, the rods remained in their initial horizontal orientation, and other initial orientations were not considered.

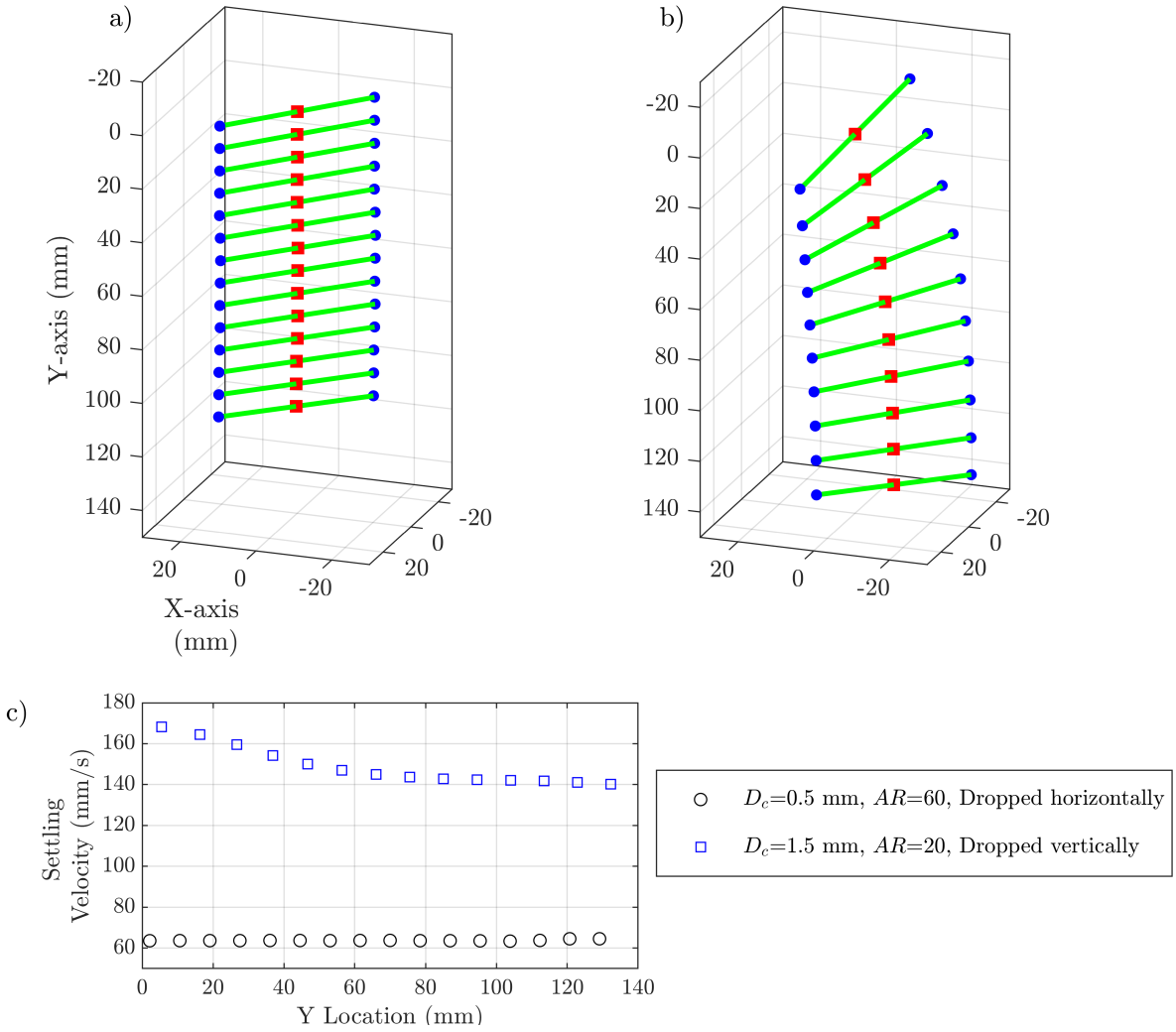

Figure 4.1: Three-dimensional view of the trajectory of straight cylindrical rods. The circles indicate the endpoints, whereas the square indicates the center of gravity. (a) Straight rod with diameter of 0.5 mm and aspect ratio of 60 dropped horizontally, (b) straight rod with diameter of 1.5 mm and aspect ratio of 20 dropped vertically, (c) settling velocity determined at the centroid for cases (a) and (b).

4.1.2 V-Shaped Rods

As mentioned in Section 3.4.2, the real-life locations of the V-shaped rod centroid, endpoints, and midpoint were determined using stereo imaging and analysis. Assuming that the centroid of the rod in the first captured frame is at the origin, the locations of these points in the initial frame as well as the subsequent frames can be determined. This process enables the

determination of the 3D trajectory of the rod fall, as shown in Figure 4.2. In this figure, every seventh frame has been included in the trajectory for improved visualization. Similar to straight and curved rods, the 3D trajectories and the images captured from the bottom camera reveal that V-shaped rods show no spinning motion once they reach their stable terminal velocity and orientation. The V-shaped rods consistently orient horizontally such that their centroid is positioned at the lowest point. A similar orientation is also observed for the curved rods as reported in the studies by Daramsing [49], Rong *et al.* [36], and Cox [107]. Moreover, all V-shaped rods, like straight and curved rods, settle vertically upon reaching their stable terminal velocity, without exhibiting any horizontal drift within the range of Reynolds numbers studied in this research.

4.2 Terminal Velocity

4.2.1 Straight Rods

Figure 4.3 shows the variation of the terminal velocity with the diameter and aspect ratio of the straight rods. The brass rod data points were measured by Daramsing [49], and the aluminum rod data points were obtained in this dissertation to extend the range of Reynolds numbers. This figure shows that as the diameter and aspect ratio of the rod increase, the terminal velocity increases. However, the increase in terminal velocity with aspect ratio is less pronounced at higher aspect ratios, leading to an asymptotic trend. The observed asymptotic trend is consistent with the results of Jayaweera and Mason [99]. The terminal velocity of each rod appears to approach a constant value at high aspect ratios. This is likely because, as the cylinder becomes longer, the effects of the two endpoints of the cylinder become less significant, and further increases in length do not significantly change the velocity. Figure 4.3 includes dashed lines, which are the calculated terminal velocities of a very long or two-dimensional cylinder based on Khalili model [103] (equation 2.21).

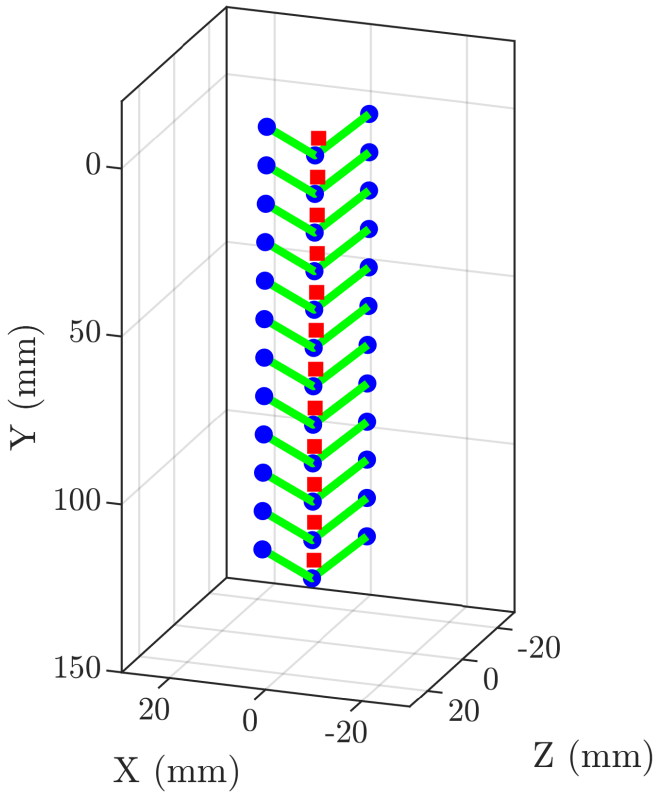

Figure 4.2: 3D trajectory of (a) a straight rod with $D_C = 0.50$ mm and $AR = 60$ and (b) a V-shaped rod with the same D_C and AR and $\alpha_0 = 90°$. The blue circles represent the endpoints and the midpoints of the rod geometry. The red squares represent the rod centroids at different instances.

4.2.2 V-Shaped Rods

The terminal velocity of the V-shaped rods at different diameters, aspect ratios, and bend angles have been determined. Figure 4.4 shows how the terminal velocity of a V-shaped rod changes with different geometric parameters, and compares it with the terminal velocity of a straight rod with the same diameter and aspect ratio. Figure 4.4 (a) illustrates the variation of the V-shaped rod terminal velocity with aspect ratio for $\alpha_0 = 45°$. Similar trends have been observed for other bend angles. This plot shows that the V-shaped rod consistently settles faster than a straight rod with the same diameter and aspect ratio. The maximum

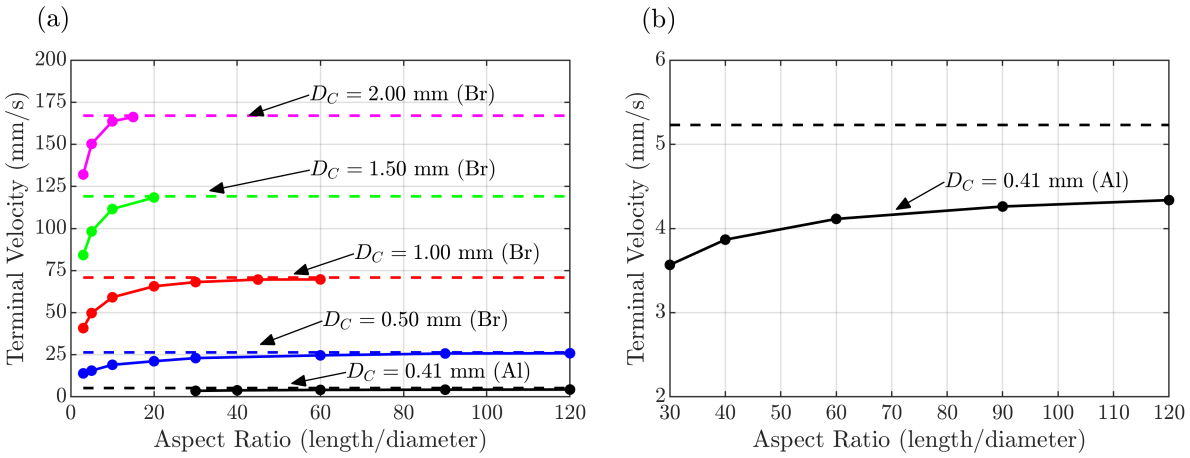

Figure 4.3: Terminal velocity of straight rods for different rod diameters and aspect ratios. Panel (b) shows the magnified plot of aluminum rods with $D_C = 0.41$ mm. The dashed lines represent the terminal velocity of an infinite cylinder calculated from the model by Khalili and Liu [103]. 'Br' means brass and 'Al' means aluminum. The brass rod data points were measured by Daramsing [49], and the aluminum rod data points were obtained in this study.

relative difference between the V-shaped and straight rod terminal velocity corresponds to $D_C = 1.0$ mm, $AR = 45$, and $\alpha_0 = 45°$, and is calculated as 57% within the ranges investigated in this study. The terminal velocity of a V-shaped rod increases with both rod diameter and aspect ratio. Similar to straight rods, it exhibits smaller variations at higher aspect ratios as shown in figure 4.4 (a) due to the reduced effects of the two endpoints of the V-shaped rod on its terminal velocity.

Figure 4.4 (b) depicts the variations of the V-shaped rod terminal velocity with bend angle. For better visualization, only the results for an aspect ratio of 30 are shown in this plot. Similar trends are observed for other rod aspect ratios. Larger bend angles between 45 and 135 degrees result in lower terminal velocities. Moreover, the rate of change in the terminal velocity of a V-shaped rod with bend angle decreases as the bend angle increases, approaching the terminal velocity of a straight rod with the same diameter and aspect ratio. Specifically, for a bend angle from 45 to 70 degrees, the terminal velocity of the V-shaped rod decreases by 13%, while it only decreases by 7% for the bend angle from 110 to 135 degrees. This can be attributed to the V-shaped rod terminal velocity being more sensitive to endpoint

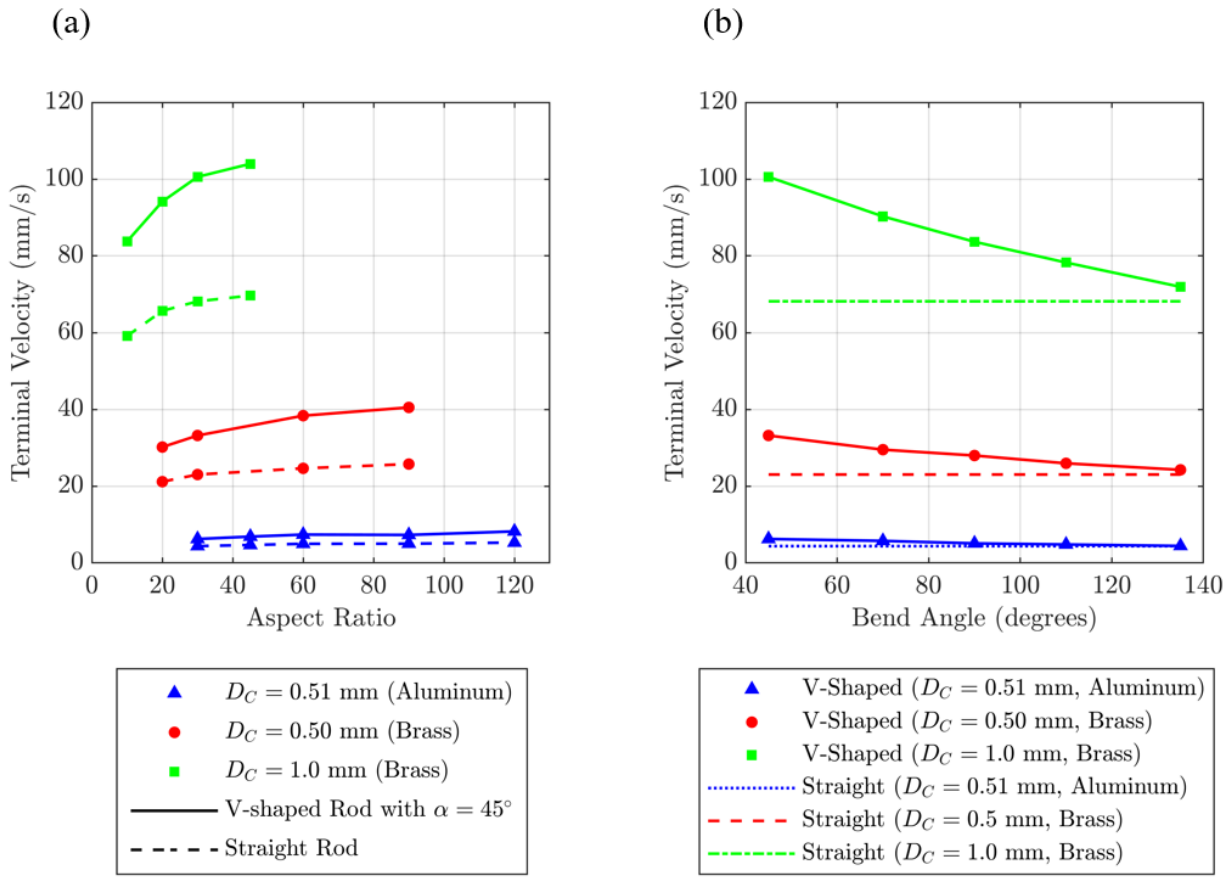

Figure 4.4: Terminal velocity of V-shaped rods with different diameters, aspect ratios, and bend angles. Panel (a) shows the variation of V-shaped rod terminal velocity with aspect ratio for different rod diameters and its comparison with straight rods. For better visualization, only the results of $\alpha_0 = 45°$ are shown. Panel (b) shows the variation of V-shaped rod terminal velocity with bend angle for different rod diameters and its comparison with straight rods. For better visualization, only the results of $AR = 30$ are shown.

effects at smaller bend angles or when the two arms of the rod are more vertically oriented.

Figure 4.5 shows the ratio of the V-shaped rod terminal velocity to that of a curved rod with the same diameter, aspect ratio, and projected area at different curvature indices (denoted by C as defined in equation 3.5) for $D_C = 0.50$ mm and $AR = 60$ and 90. In this comparison, only the effect of the rod geometry, curved or V-shaped, on the rod terminal velocity is taken into consideration. The results show that within the ranges studied in this

research, the V-shaped rod settles only slightly faster than the curved rod. The relative difference between the V-shaped and curved rod terminal velocities increases with C and reaches the highest value of 4% at $C = 0.36$. As discussed in Section 3.2.2, the maximum feasible value for C for the curved rods is 0.36, which is associated with a semi-circle. Based on figure 4.5, the ratios of the V-shaped rod terminal velocity to that of the curved rod are almost the same for the two rod aspect ratios, indicating that this velocity ratio depends only on the curvature index and is independent of the rod aspect ratio.

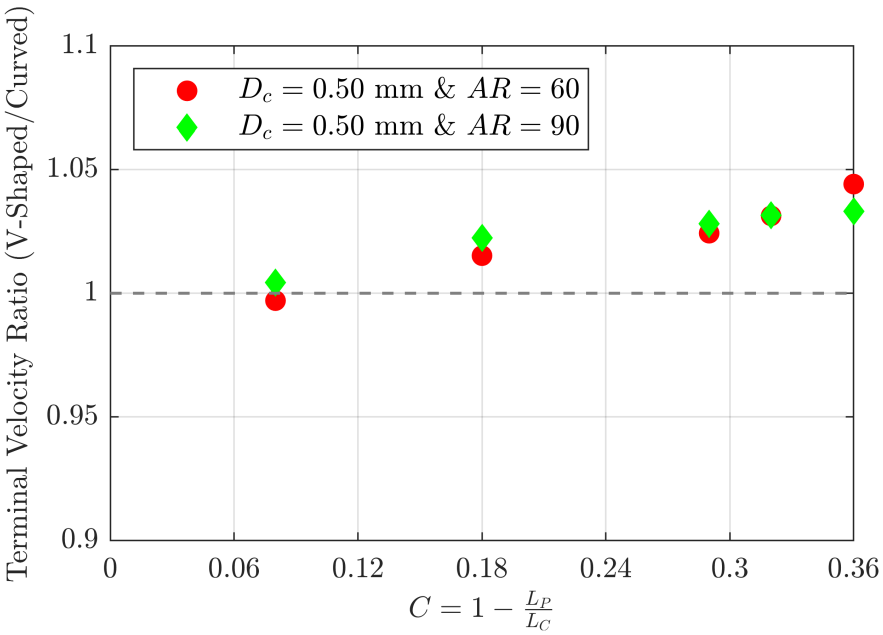

Figure 4.5: The ratio of the V-shaped rod terminal velocity to that of the curved rod with the same projected areas.

The marginal increase in the terminal velocity of the V-shaped rod compared to the curved rod with the same dimensions and projected area can be explained by comparing the "mean inclination angle" of the curved rod with that of the V-shaped rod. According to figure 4.6, the inclination angle of an arbitrary element of the curved rod at point A (ds) can be defined as the angle between the tangential line to the curved rod at this point and the vertical line. This angle is denoted by ζ, and can be calculated from

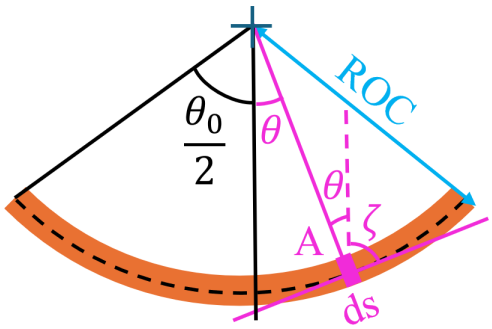

Figure 4.6: Definition of inclination angle for a curved rod.

$$\zeta = \frac{\pi}{2} - \theta \tag{4.1}$$

Therefore, the mean inclination angle for the whole curved rod ($\bar{\zeta}$) can be calculated from

$$\bar{\zeta} = \frac{1}{(\text{ROC})(\theta_0/2)} \int_0^{\theta_0/2} (\frac{\pi}{2} - \theta)\, \text{ds}, \tag{4.2}$$

where $\text{ds} = (\text{ROC})\text{d}\theta$. Equation 4.2 results in $\bar{\zeta} = (\pi/2) - (\theta_0/4)$. Considering the equality of the rod total length and projected length between the V-shaped and the curved rods, the ratio $\beta = L_P/L_C$ is the same for both types of rods. From equations 3.6 and 3.7, the relationship between the V-shaped rod inclination angle, denoted by α_0' which is equal to $\alpha_0/2$, and the arc angle of the curved rod (θ_0) is

$$\alpha_0' = \sin^{-1}(\frac{2\,\sin(\theta_0/2)}{\theta_0}). \tag{4.3}$$

The ratio of the curved rod mean inclination angle to that of the V-shaped rod ($\bar{\zeta}/\alpha_0'$) is plotted versus θ_0 in figure 4.7. This figure shows that $\bar{\zeta}$ is consistently larger than α_0', indicating a more horizontally aligned mean orientation for the curved rod compared to the V-shaped rod with the same dimensions and projected area. This difference in the mean orientations accounts for why the V-shaped rod settles slightly faster than the corresponding curved rod within the ranges of this study. As an example, for a curved rod with $C = 0.36$,

corresponding to a V-shaped rod with the same dimensions and projected area at $\alpha_0 = 80°$, $\bar{\zeta}$ is 45.2° based on the ratios shown in Figure 4.7. This is equivalent to a V-shaped rod with the same dimensions and a bend angle of 90.4°. Based on the experimental results in this study, the terminal velocity of a V-shaped brass rod with $D_C = 0.50$ mm and $AR = 90$ is 32.8 mm/s and 34.1 mm/s for $\alpha_0 = 90°$ and 80°, respectively, showing a difference of 4%, which is consistent with the results illustrated in figure 4.5. The terminal velocity of the V-shaped rod with $\alpha_0 = 80°$ is determined by interpolation between the velocities at $\alpha_0 = 70°$ and $\alpha_0 = 90°$.

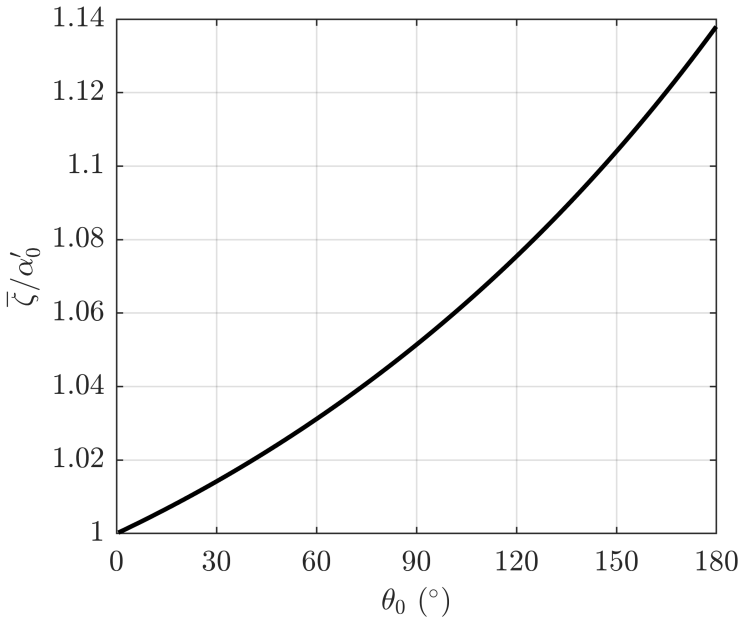

Figure 4.7: Ratio of the mean inclination angle of the curved rod ($\bar{\zeta}$) to that of the V-shaped rod (α_0') versus curved rod arc angle (θ_0).

4.3 Drag Coefficient

In this section, the variations of the straight and V-shaped rod drag coefficient with Reynolds number for different rod diameters, aspect ratios, and bend angles are discussed. The Reynolds number is calculated from

$$\mathrm{Re} = \frac{\rho_f V_S D_{eq}}{\mu_f}, \tag{4.4}$$

where ρ_f, V_S, D_{eq}, μ_f represent the density of the fluid, the terminal velocity of the rod, the diameter of a sphere with the same volume as the rod, and the viscosity of the fluid. D_{eq} is calculated from

$$D_{eq} = (\frac{3}{2} D_C^2 L_C)^{\frac{1}{3}}. \tag{4.5}$$

The drag coefficient is calculated from [31, 38, 50]

$$C_D = \frac{(\rho_P - \rho_f) g (\pi/4) D_C^2 L_C}{0.5 \rho_f V_S^2 A_P}, \tag{4.6}$$

where ρ_P and g are the rod density and gravity acceleration, respectively. A_P is $L_C D_C \sin(\alpha_0/2)$ for the V-shaped rods and $L_C D_C$ for the straight rods, given their orientations when they reach terminal velocity, as discussed in Section 4.1.

This research focuses on the settling of rods in a quiescent fluid when they reach a stable orientation and terminal velocity; therefore, the volume-equivalent diameter is used to calculate the Reynolds number. Yang *et al.* [37] found that the diameter of a finite fibre has the greatest influence on the terminal velocity compared to other factors, such as length or curvature index, in a quiescent fluid. Nevertheless, the effects of other dimensions are also important in relating the drag coefficient to the Reynolds number for non-spherical particles, as shown by Song *et al.* [38], Bagheri *et al.* [31], and Zhang *et al.* [39]. Concerning fibres, Nguyen *et al.* [35] showed that there is a strong correlation between the drag coefficient and the Reynolds number based on the volume-equivalent diameter. This scaling resulted in the least variability in the drag coefficient for a given Reynolds number. However, in cases where the rods undergo reorientation, such as while subject to turbulence, vortex motions, or inertial torques, the length of the cylinder is known as an important parameter in the calculation of the Reynolds number [102, 138].

4.3.1 Straight Rods

The variation of the straight rod drag coefficient with Reynolds number is shown in figure 4.8. The uncertainties in the calculated values of Re and C_D are determined using the method explained in Section 3.4.4. The uncertainties mentioned are comparable in size to the markers shown in figure 4.8; therefore, they are not displayed. However, in subsequent figures with more detailed views and narrower variable ranges, the corresponding uncertainty bars are included. The brass rod data points were measured by Daramsing [49], and the aluminum rod results were obtained in this study. According to this figure, the Reynolds number of the straight rods increases with diameter and aspect ratio due to the increased terminal velocity, which is consistent with the results shown in figure 4.3. Similar to the trend predicted by Stokes' Law, $C_D = 24/\mathrm{Re}$, there is also a decrease in the value of the drag coefficient with an increase in the diameter of the rods. A decrease in the value of the drag coefficient is also observed with an increase in aspect ratio for rods of the same diameter. For the increasing values of aspect ratio for the same diameter, the rod length (L_C) and, consequently, the diameter of a volume-equivalent sphere (D_{eq}) increases as predicted by equation 4.5, which leads to a decrease in the drag coefficient.

The experimental data for the drag coefficient of the straight rods are compared with the models of Khalili and Liu [103] and Huner and Hussey [104] in figure 4.9. These models were developed to estimate the drag coefficient of a two-dimensional cylinder at a low Reynolds number, which can represent a cylinder with infinite length or a very high aspect ratio. To make our drag coefficient data comparable with the mentioned models, the Reynolds number for our data is recalculated based on the cylinder diameter (D_c), and the drag coefficient is determined based on the drag force and projected area per unit length of the cylinder, indicated by F'_D and A'_P respectively in figure 4.9. As can be seen in figure 4.9, as the aspect ratio of the rod increases for a certain diameter, the drag coefficient asymptotes to the value predicted by the two-dimensional cylinder models. At the highest aspect ratio, the findings of the present research for drag coefficient are in good agreement with the Khalili model

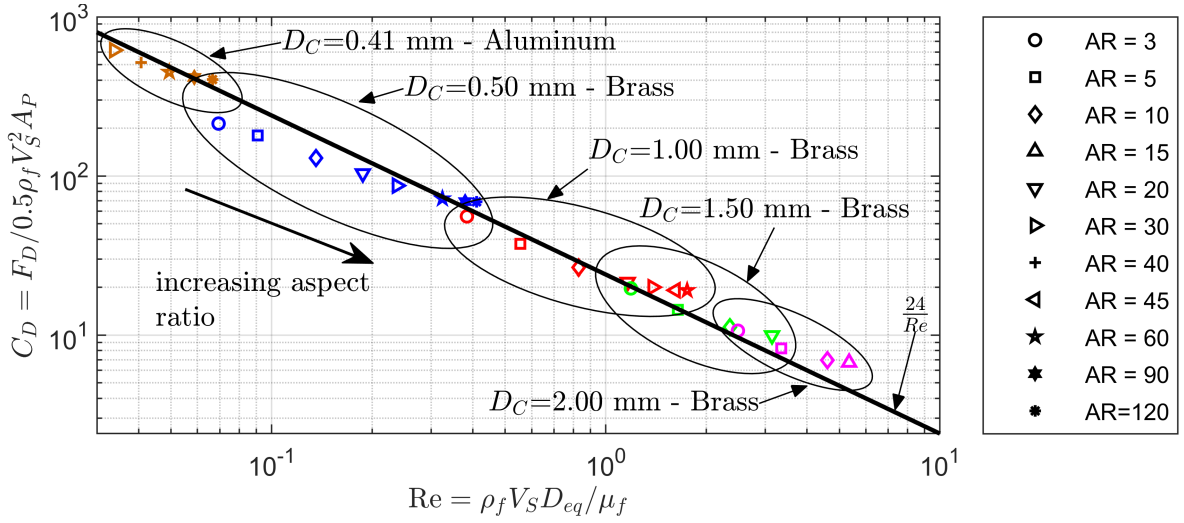

Figure 4.8: Variation of drag coefficient with Reynolds number for different diameters and aspect ratios of straight rods. The uncertainties of C_D and Re are of the same size as the markers shown in this figure. The brass rod data points were measured by Daramsing [49], and the aluminum rod results were obtained in this study.

[103]. Huner model [104] is valid for larger Reynolds number (0.23<Re, where Re is based on cylinder diameter), which explains the deviation of its results from Khalili model [103] and the experimental data points obtained in this research at lower Reynolds numbers, especially for Re < 0.1.

The experimental results of the straight rods are also compared with Jayaweera's results [99] in figure 4.10 within the common range of Reynolds number based on the rod diameter. A power correlation has been fitted to the C_D versus Re data points presented by Jayaweera (1965) with $R^2 = 0.99$. The drag coefficients for the Reynolds numbers obtained in this research are then calculated from the mentioned correlation and compared with the corresponding C_D values obtained in this research. It should be noted that in figure 4.10, the Reynolds numbers are calculated based on the rod diameter (D_C) to make the results consistent with Jayaweera's results [99]. The RMS error resulting from this comparison is 9.7%.

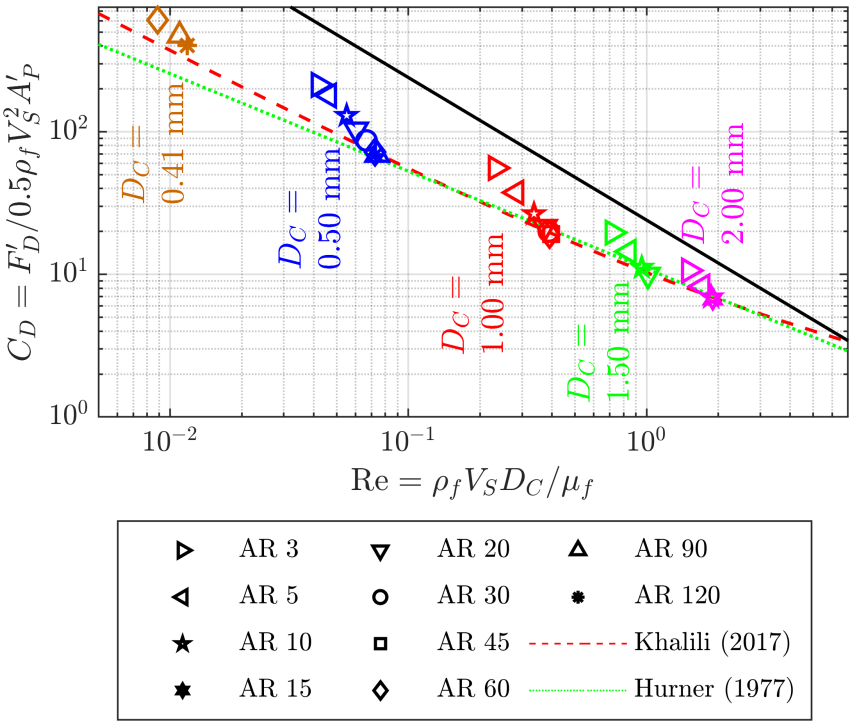

Figure 4.9: Comparison of the experimental results in the present study with models for prediction of infinite cylinder drag coefficient. The brass rod data points were measured by Daramsing [49], and the aluminum rod results were obtained in this study.

4.3.2 V-Shaped Rods

Figure 4.11 shows the variation of the V-shaped rod drag coefficient with Reynolds number for different rod diameters, aspect ratios, and bend angles studied. Similar to straight rods, an increase in the V-shaped rod aspect ratio for a given diameter leads to an increase in the Reynolds number due to the increase in the diameter of the volumetric-equivalent sphere as well as the rod terminal velocity. A change in the diameter and material of the rods shifts the Reynolds number sub-range covered by the corresponding results at different aspect ratios and bend angles. For instance, the ranges of $0.05 < \mathrm{Re} < 0.14$, $0.19 < \mathrm{Re} < 0.62$, and $0.83 < \mathrm{Re} < 2.62$ are covered by the aluminum rods with $D_C = 0.51$ mm, brass rods with $D_C = 0.50$ mm, and brass rods with $D_C = 1.0$ mm, respectively. Furthermore, for

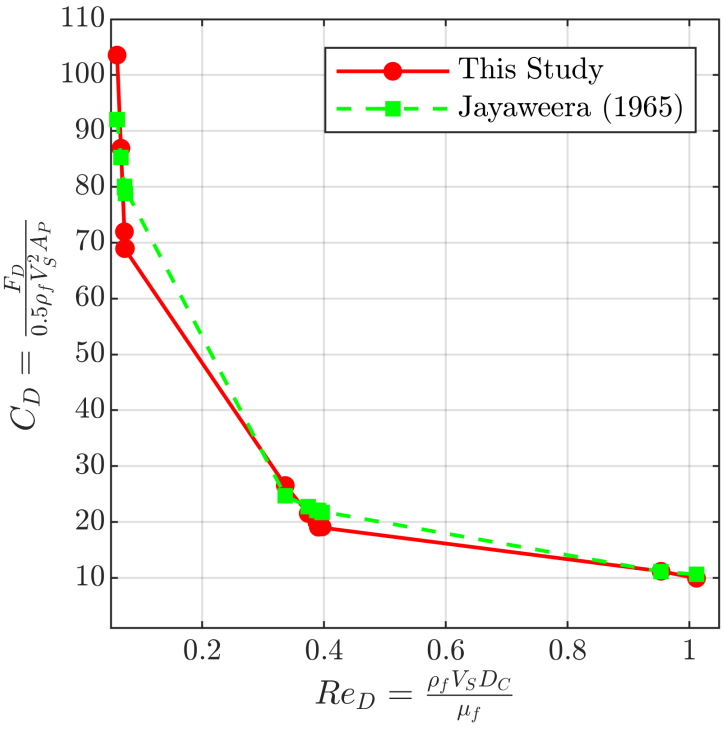

Figure 4.10: Comparison of the straight rod results in the present research with Jayaweera's results [99]. The Reynolds number is calculated based on the rod diameter (D_C) in this comparison.

the same diameter and aspect ratio, the Reynolds number increases with a decrease in the V-shaped rod bend angle due to the increased terminal velocity, as discussed in Section 4.2. The results in figure 4.11 also indicate that, similar to the straight rods, the drag coefficient of a V-shaped rod decreases with both rod aspect ratio and diameter. The increase in these two dimensions leads to an increase in the diameter of the volumetric-equivalent sphere as well as the rod terminal velocity, resulting in a decrease in the drag coefficient. This decreasing trend is consistent with the Stokes' law for a sphere ($C_D = 24/\mathrm{Re}$) as shown in figure 4.11. However, the drag coefficient values for both V-shaped and straight rods deviate from the Stokes' law due to the deviation of the cylindrical rod geometries from their corresponding volumetric-equivalent spheres.

The trend in the change of the drag coefficient with the bend angle of a V-shaped rod

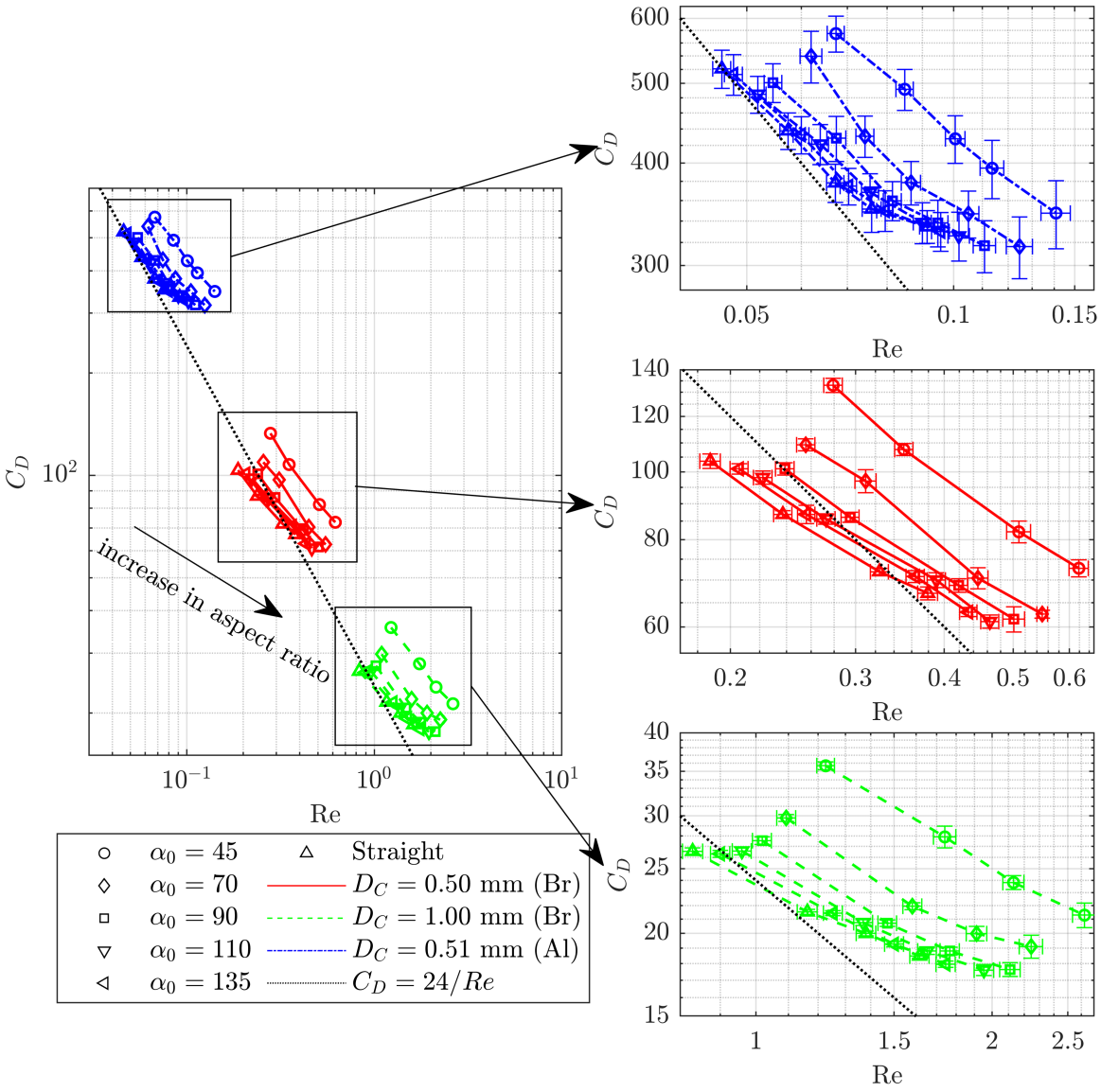

Figure 4.11: Variation of the V-shaped and straight rod drag coefficient with Reynolds number for different rod diameters, aspect ratios, and bend angles. The dotted line shows the drag coefficient calculated based on the Stokes law for a sphere. “Al" means aluminum and “Br" means brass.

is also illustrated by the data points in figure 4.11. The drag coefficient of a V-shaped rod with a certain diameter and aspect ratio decreases as the bend angle decreases from 180 degrees (straight rod) to approximately 90 degrees. It should be noted that this range of

bend angle is associated with the range of curvature index ($0 < C < 0.36$) or the projected length-to-total length ratio ($0.64 < \beta < 1$), within which a curved rod with arc angle less than 180° can be made to have the same projected area as each V-shaped rod. For bend angles lower than 90 degrees, as the bend angle decreases, the drag coefficient increases. The reason for this trend can be explained with respect to equation 4.6. As α_0 increases, V_S decreases as discussed in Section 4.2, while A_P increases due to an increase in the rod projected length. Consequently, an increase or a decrease in C_D with α_0 depends on trade-off between V_S^2 and A_P. The greater influence of V_S^2 compared to A_P across the range $90° < \alpha_0 < 135°$ results in an increase in C_D with increasing α_0, whereas the stronger effect of A_P over V_S^2 causes C_D to decrease as α_0 increases within $45° < \alpha_0 < 90°$.

4.4 Model Development

A new model to predict the drag coefficient and terminal velocity of straight, curved, and V-shaped rods is developed in this section based on the experimental results obtained in this study. This model is based on the framework developed by Song *et al.* [38], originally formulated for spherical and non-spherical particles settling in a quiescent fluid.

The model by Song *et al.* [38] is given by equation 2.10. In this equation, ϕ is sphericity, defined as the ratio of the surface area of the volume-equivalent sphere to that of the particle. S is the projected area ratio, defined as the ratio of the projected area of the volume-equivalent sphere to that of the particle. a', b', c', and d' are constant coefficients. Incorporation of the terms $(1/\mathrm{Re})$ and $(1 + a'\mathrm{Re})$ in this model accounts for both very low and moderate Reynolds numbers, as seen in other similar models for the settling of particles [31, 40, 88, 139]. The term $(1/\mathrm{Re})$ is important in the Stokes' regime (low Reynolds numbers), while $(1 + a'\mathrm{Re})$ becomes relevant at moderate Reynolds numbers. Sphericity (ϕ) is calculated from

$$\phi = \frac{\pi D_{eq}^2}{\frac{\pi}{2} D_C^2 + \pi D_C L_C}, \tag{4.7}$$

where D_{eq} is the diameter of a volume-equivalent sphere and can be calculated from equation

4.5. Sphericity is a measure of the extent to which the rod geometry deviates from that of a sphere with the same volume. It ranges from 0 to 1. The closer it is to 1, the more similar the geometry of the particle is to a volume-equivalent sphere. Obviously, for a cylindrical rod with a specific volume, the sphericity decreases as the aspect ratio increases since it deviates more from a sphere. The variable S in equation 2.10 is a function of the orientation of the particle during its settling. It becomes particularly significant when studying a range of particle geometries with varying orientations, as demonstrated in the research conducted by Song *et al.* [38] or Bagheri *et al.* [31]. Since the orientation of the straight, curved, and V-shaped rods remains horizontal during settling within the range of Reynolds numbers studied in this research, the S term is omitted from equation 2.10, which leads to

$$C_D = \frac{24}{\mathrm{Re}(\phi^{c'})}(1 + a'\mathrm{Re})^{b'}. \tag{4.8}$$

Equation 4.8 was fitted to all experimental data points for straight rods, and the coefficients a', b', and c' were determined. When comparing the C_D results of the model with the experiments, a Root Mean Square (RMS) error of 22% was calculated. To reduce the obtained error, aspect ratio (AR), known as one of the important shape factors describing cylindrical rods, was added to the new model. As the length of a rod increases while maintaining a constant diameter, the terminal velocity also increases. However, as described in Section 4.2, this increase in velocity shows an asymptotic behavior due to the balance between gravity, buoyancy, and drag forces, and the negligible effect of the rod ends on the drag force for longer rods. Additionally, as the aspect ratio increases, the drag coefficient decreases non-linearly with terminal velocity, as shown in figure 4.11, leading to a general decreasing trend that becomes asymptotic at very high aspect ratios. To represent this relationship, a power function is used, and the variation of drag coefficient with aspect ratio is considered as $C_D \propto 1/AR^c$. Therefore, the new general model is

$$C_D = \frac{24}{\mathrm{Re}(AR^c\phi^d)}(1 + a\mathrm{Re})^b. \tag{4.9}$$

Equation 4.9 was fitted to the data points of the straight rods, and the coefficients a, b, c, and d were determined as 0.25, 0.96, 1.20, and 4.38. The RMS error of the new model, when comparing the C_D results between the model and the experiments, was calculated to be 6.8%. This demonstrates a substantial improvement in the RMS error of the model when compared with considering only ϕ in equation 4.9

In the next step, another term, β, was added to equation 4.9, to account for the curved and V-shaped rods. As described in Section 3.2.2, β is defined as the ratio of the projected length (L_P in figure 3.3) to the total length of the cylindrical rod (L_c). Considering the orientations of the rods while settling, β is equal to 1 for straight rods and L_P/L_C for V-shaped and curved rods. As discussed in Section 4.2, there is a marginal difference between the terminal velocity of a V-shaped rod and that of a curved rod with the same diameter, aspect ratio, and projected area, and consequently the same β, within the Reynolds number range investigated in this study. This difference reaches the maximum value of only 4% at $C = 0.36$ as shown in figure 4.5. Therefore, it is assumed that a curved rod settles as fast as a V-shaped rod with the same D_C, AR, and β, and a single model will be applied for both. As the value of β decreases, the rod becomes more bent or curved and its shape aligns more with the surrounding flow streamlines. This results in a smaller wake region behind the rod and consequently smaller drag coefficient. The data points in Figure 4.11 for V-shaped rods, along with the curved rod data from Daramsing [49] and this dissertation (published as a joint work [50]), suggest that the drag coefficient of V-shaped and curved rods varies nonlinearly with their bend angle and radius of curvature, respectively. It approaches the drag coefficient of a straight rod as β increases; therefore, a power function ($C_D \propto 1/\beta^e$) is considered in this study. The new form of our model is given by

$$C_D = \frac{24}{\mathrm{Re}(AR^c\phi^d\beta^e)}(1 + a\mathrm{Re})^b. \tag{4.10}$$

This model was fitted to all experimental data points related to the V-shaped and curved rods, and the coefficient e was determined as 0.65. Part of the curved rod results were obtained

by Daramsing [49] and were extended in this dissertation by incorporating new curved rods, listed in table 3.3, as well as aluminum rods, shown in figure 4.14, to broaden the range of curvature index and Reynolds numbers, respectively. As a result, equation 4.10 shows the final form of our new model, and the coefficients used in this model are summarized in table 4.1.

Table 4.1: The coefficients used in our new model (equation 4.10).

a	b	c	d	e
0.25	0.96	1.20	4.38	0.65

4.4.1 Comparison with Experiments and Other Models

Straight Rods

The settling velocities of straight cylindrical rods falling in a glycerin mixture can be calculated using the new model proposed in this research (equation 4.10) assuming $\beta = 1$. An iterative solution method is employed to establish the relationship between drag coefficient and Reynolds number. The process begins with an initial guess for the Reynolds number (Re), followed by the calculation of the drag coefficient (C_D) using equation 4.10. The settling velocity (V_S) is then determined from equation 4.6 and subsequently used in equation 4.4 to compute an updated Reynolds number. This process is repeated until convergence is achieved, which is defined as the updated Reynolds number differing by less than 0.1% from the previous iteration. Figure 4.12 compares the calculated results for straight rods from our model and other models with the measured results from the experiments conducted in this dissertation and by Daramsing [49]. It should be noted that the experimental data points for straight brass rods were measured by Daramsing [49], while the data points for straight aluminum rods were measured in this dissertation. The experimental data points shown in figure 4.12 were corrected to the boundless domain following the method outlined by Brenner [134] and mentioned previously in Section 3.4.3.

The dashed line in figure 4.12 has a slope of 1. The closer the data points obtained from

a specific model align with this line, the better the agreement between the calculated and measured results. It is evident from this figure that the new model proposed in this research shows the best alignment with the experimental data. While the models developed by Song *et al.* [38], Bagheri *et al.* [31], Ganser [40], and Zhang *et al.* [39] all underestimate the terminal velocity of straight rods, the model by Yu *et al.* [95] overestimates the terminal velocities. Notably, these models were developed for a wide range of geometries rather than specifically for cylindrical rods. Therefore, there may be inaccuracies in predicting the terminal velocity of cylindrical rods. The Henn model [69] fails to accurately predict the terminal velocity of the cylindrical rods at high aspect ratios and tends to overestimate the velocities. The Cox model [107] was developed for low Reynolds numbers and long slender bodies. However, it does not offer high accuracy for the entire range of aspect ratios and diameters studied in this research. Although the Kharrouba *et al.* [41] and Fintzi *et al.* [138] models exhibit better alignment with the experimental data points than other models from the literature, there are still significant discrepancies in their results when compared to the experimental findings. Moreover, the velocities calculated from the model by Goral *et al.* [42] deviate from the experimental data at smaller rod diameters of 0.41, 0.50, and 1.0 mm in this comparison. This deviation is primarily because this model developed for circular cylinders is generally valid for Re > 1. The RMS errors of this model are calculated as 110.6% for Re < 1 and 12.4% for Re > 1, indicating the inaccurate prediction of the model for Reynolds numbers below 1 and its good performance for Reynolds numbers above 1. On the contrary, the model by Yuan *et al.* [140] offers more accurate results for Re<1. The RMS error calculated for this model is 16.4% for Re<1 and 20.7% for Re>1.

The values of root mean square error (RMSE) and R^2 corresponding to our new model and other models are listed in table 4.2. These values are calculated by comparing the results from the models with the experimental data points obtained in this research. R^2 (R-squared), known as coefficient of determination, is a measure of how the calculated results deviate from the experimental results and is an indicator of the goodness of a fitting. R^2 is calculated from

$$R^2 = 1 - \frac{SSR}{SST}. \tag{4.11}$$

In equation 4.11, SSR is the sum squared regression and is calculated from

$$SSR = \Sigma_i (V_{S,i} - \hat{V_{S,i}})^2, \tag{4.12}$$

where $V_{S,i}$ is the calculated terminal velocity and $\hat{V_{S,i}}$ is the measured terminal velocity. SST is the total sum of squares, and is calculated from

$$SST = \Sigma_i (V_{S,i} - \bar{V_{S,i}})^2, \tag{4.13}$$

where $\bar{V_{S,i}}$ is the average of all calculated velocities. R^2 ranges between 0 and 1, and the closer R^2 to 1, the better the model aligns with the measured results.

Table 4.2 shows that the new model presented in this study best conforms to the experimental data, as indicated by its low RMS error and an R^2 value close to 1. The RMS error of our new model for the straight rods with an aspect ratio less than 10 is 8.2% while this error for the modles by Cox [107], Kharrouba *et al.* [41], and Fintzi *et al.* [138] is 28.3%, 28.8%, and 27.5%, respectively. Therefore, for a relatively low aspect ratio, the logarithmic relation between the drag coefficient and aspect ratio utilized in the aforementioned models may limit their applicability and the model proposed in this study results in a lower error than those developed based on slender body theory (SBT). For aspect ratios larger than 10, the RMS error of our model is 5.1%, whereas it is calculated as 28.7%, 8.9%, and 18.7% for the models developed by Cox [107], Kharrouba *et al.* [41], and Fintzi *et al.* [138], respectively. Overall, the results of our new model for the terminal velocity of straight rods align better with the experimental data than the previous models based on SBT within the Stokes regime and for both low and high aspect ratios ($3 < AR < 120$).

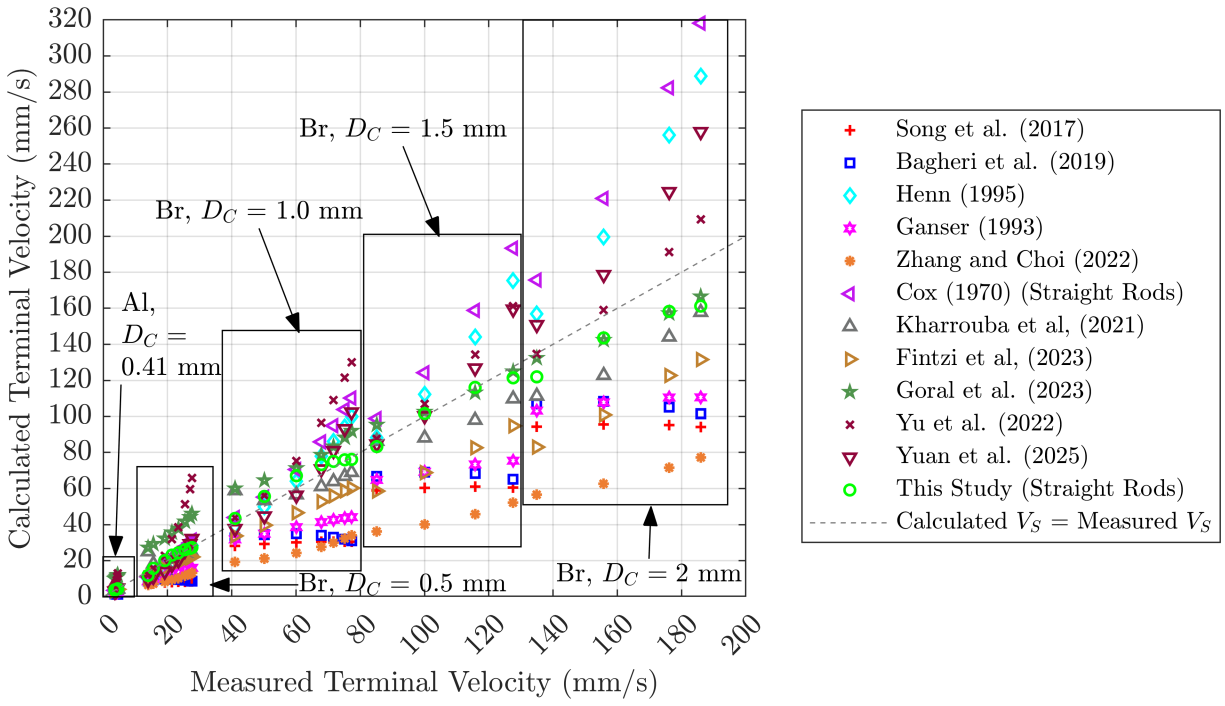

Figure 4.12: Terminal velocity of straight rods calculated using various models compared to terminal velocities measured in the present research or by Daramsing [49]. The data points for straight brass rods were measured by Daramsing [49], while the data for aluminum rods were obtained in this study. The hollow and filled green circular symbols represent the results for straight cylindrical rods, respectively. The dashed line equates the measured and calculated data. 'Al' denotes aluminum, whereas 'Br' denotes brass.

V-shaped rods

The terminal velocities of the V-shaped rods settling in water-glycerin mixture with a glycerin weight ratio of 90% at a temperature of 21°C have also been calculated using the model developed in Section 4.4. The calculated results have been compared with the experimental data points obtained in this study in figure 4.13, and an RMS error of 7.9% is obtained. The experimental terminal velocities shown in this figure have been corrected using Brenner's correction factor [134], as outlined in Section 3.4.3, to account for the effects of the bounded medium in which the rod settles.

The terminal velocities of the V-shaped rods investigated in this research have also been compared with two other models by Kharrouba *et al.* [41] and Fintzi *et al.* [138], which

Table 4.2: RMS error (RMSE) and R^2 values associated with the model presented in this research and other models when compared to experimental results for straight rods from figure 4.12.

	Song (2017)	Bagheri (2019)	Henn (1995)	Ganser (1993)	Zhang (2022)	Cox (1965)
RMSE (%)	56.0	51.1	21.4	38.0	55.0	28.5
R^2 Value	0.51	0.62	0.71	0.71	0.21	0.46
	Kharrouba (2021)	Fintzi (2023)	Goral (2023)	Yu (2022)	Yuan (2025)	This Study
RMSE (%)	20.1	22.9	81.4	74.0	18.4	6.6
R^2 Value	0.94	0.80	0.95	0.84	0.87	0.98

were developed for the aerodynamic forces acting on an inclined cylinder at low Reynolds numbers. For this comparison, it is assumed that a V-shaped rod is made of two inclined cylinders, with an inclination angle of $\alpha_0/2$ relative to a vertical direction, and the total drag force opposite to the vertical settling direction is calculated. The horizontal lift forces applied to the two inclined cylinders balance each other out due to the symmetry of the V-shaped rod geometry relative to the middle vertical axis. Therefore, the only component of the aerodynamic force affecting the settling of a V-shaped rod is the vertical drag force acting on each inclined arm. Considering the mentioned drag force, as well as the gravity and buoyancy forces exerted on the V-shaped rods, the terminal velocities are determined and compared with the experimental results in figure 4.13. As can be seen, there are larger discrepancies between the experimental data and both the Kharrouba model [41] and the Fintzi model [138]. The RMS errors of the Kharrouba model [41] and the Fintzi model [138] when compared to the measured terminal velocities of the V-shaped rods are 19.4% and 23.5%, respectively. The assumption of two individual inclined rods instead of a V-shaped rod neglects the interactions between the two rods when they are joined at one endpoint, which may account for the discrepancy. The terminal velocities predicted by the Kharrouba and Fintzi models are underestimated.

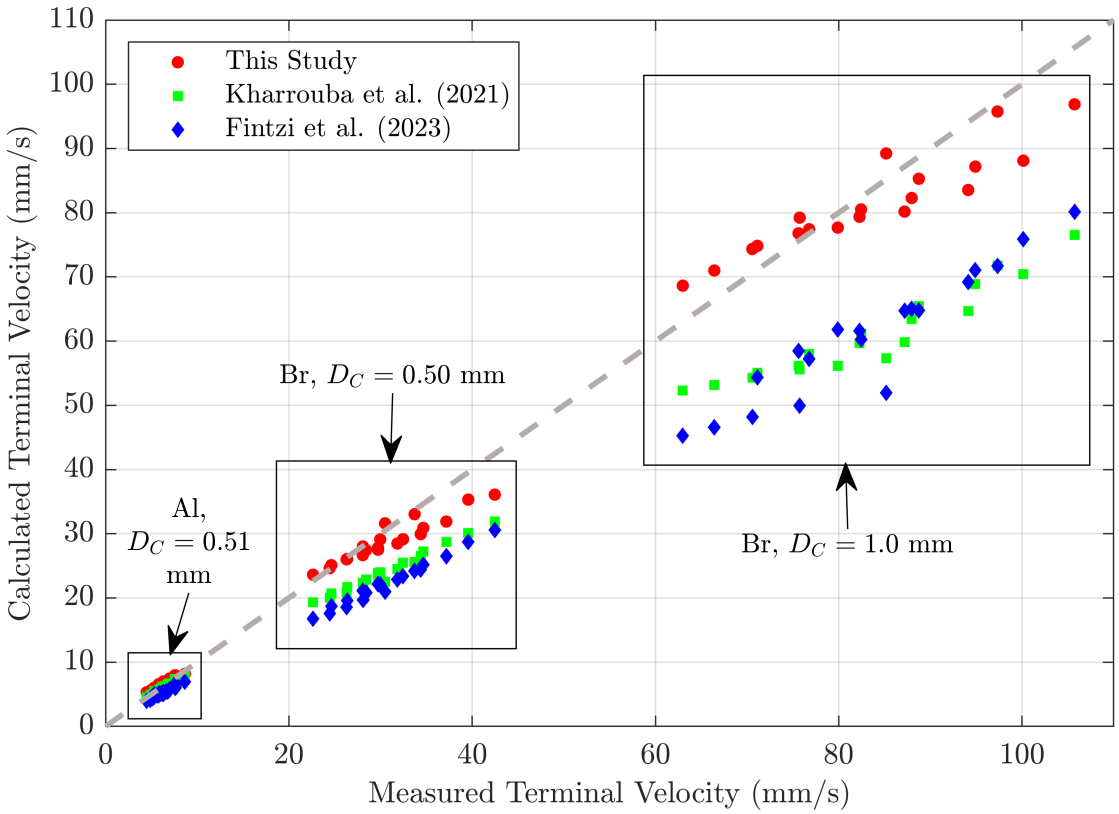

Figure 4.13: Comparison of the V-shaped rod terminal velocities settling in 90% glycerin mixture, calculated from the new model developed in this study (equation 4.10), with the measured terminal velocities. The results of two other models developed for inclined cylinders relative to the flow, Kharrouba *et al.* [41] and Fintzi *et al.* [138] models, have also been compared to the experimental results. The dashed line equates the calculated data points with the measured data points. 'Al' means aluminum and 'Br' means brass.

Curved Rods

The curvature index (C) in our recent study [50] ranges between zero and 0.25, while with the newly added curved rods mentioned in table 3.3, the curvature index range is extended to $0 < C < 0.36$ in the present study. As discussed in Section 3.2.2, this range covers the entire feasible curvature index range for all curved rods with $\theta_0 < 180°$. The terminal velocities of the curved rods calculated from our previous model [50] (equation 2.27) and the model proposed in this study (equation 4.10) are compared with the experimental data in figure 4.14. The experimental results for curved aluminum rods, as well as the brass curved rods

mentioned in table 3.3, were obtained in this dissertation, while the experimental results for all other curved brass rods were obtained by Daramsing [49]. All experimental data were corrected utilizing Brenner's correction factors [134] to account for the impacts of bounded medium. As evident from this figure, the data points associated with our new model in this study are closer to the dashed line representing a perfect alignment. The RMS error of our previous model for all the curved rods investigated in the previous and current studies is 6.8%, whereas the RMS error of our new model for the same rods is 4.1%. The primary reason for the difference in accuracy between these two models for the curved rods is that our previous model is valid within $C < 0.25$, while the valid curvature index range in our new model is extended to $C < 0.36$ due to the inclusion of newly studied curved rods (table 3.3). The RMS error of our previous model for $0.25 < C < 0.36$, which falls outside the valid range for this model, is 11.8%, whereas it is only 4.6% in our new model. Consequently, disregarding the marginal difference between the terminal velocity of the V-shaped and curved rods with the same D_C, AR, and β, as discussed in Section 4.2, the new model proposed in this study (equation 4.10) can be applied to straight, V-shaped, and curved rods within $0.03 < \mathrm{Re} < 5$, $3 < AR < 120$, and $0.64 < \beta < 1$ with an RMS error of 7.1%.

4.4.2 Application to Atmospheric Microfibres

Straight Microfibres

In this section, the modeled terminal velocities of microplastic fibres with straight geometries in quiescent air are calculated by applying the new model developed in Section 4.4. The results for straight microfibres with a diameter of 20 μm, a density of 1184 kg/m^3 [12], and aspect ratios ranging between 1 and 120 are shown and compared with other models in figure 4.15. The minimum and maximum Re for the fibre studied in this figure are calculated as 0.07 and 0.58, respectively, corresponding to aspect ratios of 3 and 120. This range of Reynolds numbers falls within the range covered by the experiments conducted and the newly developed model in this research ($0.03 < \mathrm{Re} < 5$). According to this figure, the model proposed in this

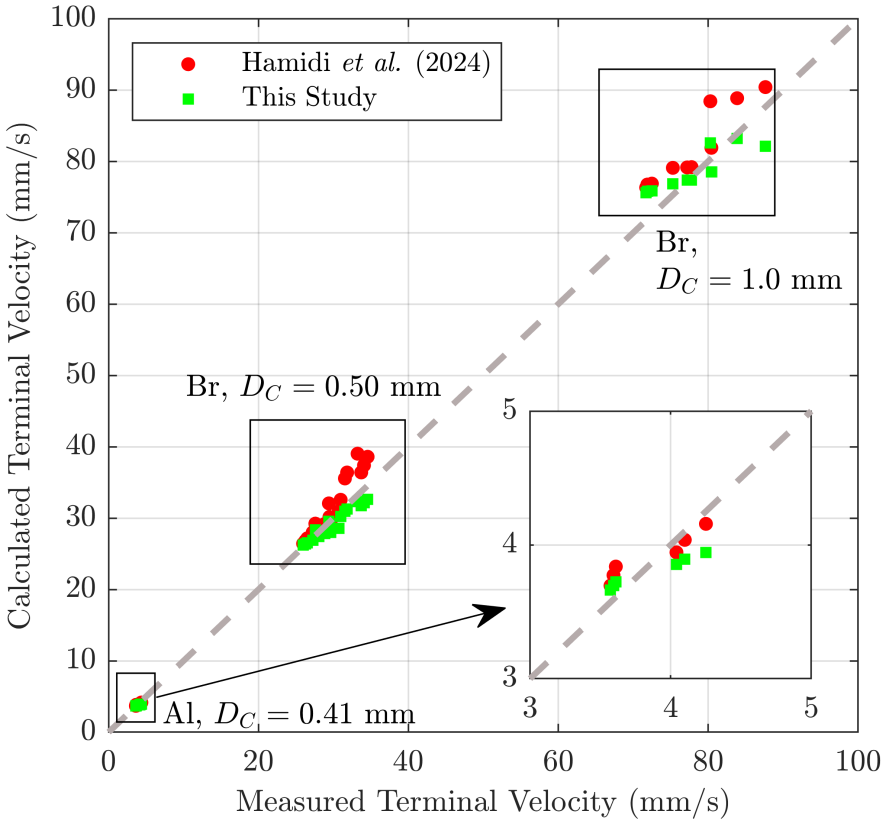

Figure 4.14: Comparison of the curved rod terminal velocities settling in 90% glycerin mixture, calculated from the model developed in our recent study [50] as well as the new model proposed in this study (equation 4.10), with the measured terminal velocities. “Al" means aluminum and “Br" means brass. The inset zooms in on the area covered by the results of aluminum rods with $D_C = 0.41$ mm.

research shows an increasing trend in the terminal velocity as the fibre aspect ratio increases. Furthermore, the fibre velocity is predicted to approach the velocities predicted by Khalili and Liu [103] or Huner and Hussey [104], which are associated with an infinite cylinder. Bagheri *et al.* [31], Song *et al.* [38], Zhang *et al.* [39], and Ganser [40] models all underpredict the fibre terminal velocity, while Yu *et al.* [95] model overpredicts it as their models cover a wide range of geometries (not only cylindrical rods), a narrower range of aspect ratios for cylindrical rods, and a broader range of Reynolds numbers, which makes these models less accurate for predicting fibre settling in the atmosphere. The Bagheri *et al.* [31] and the

Song *et al.* [38] models both predict the convergence of the terminal velocity to a constant value at a much smaller value of aspect ratio compared to other models. Furthermore, even though the Goral *et al.* model [42] used in this comparison applies only to cylinders, there is still a significant discrepancy between their model and the one presented in this study. This disparity appears to be mainly because the model developed by Goral *et al.* [42] for circular cylinders and fibres is valid only for high Reynolds numbers ($1 < \mathrm{Re} < 1000$) and relatively low aspect ratios ($AR < 30$). The maximum microfibre Reynolds number in figure 4.15 is 0.58, which falls outside the valid range for the Goral *et al.* model [42]. The main limitation of the Henn model [69] is predicting a continuous increase in the terminal velocity with aspect ratio, without showing any asymptotic behavior in the trend at higher values of aspect ratios. It is also observed in figure 4.15 that the terminal velocity predicted by our model aligns best with the infinite fibre terminal velocity predicted by Khalili and Liu [103] and Huner and Hussey [104] at high aspect ratios. The Cox model [107] overpredicts while the Kharrouba *et al.* model [41] and Fintzi *et al.* model [138] underpredict the fibre terminal velocity at high aspect ratios. The Yuan model [140] was developed for a range of Reynolds numbers less than 1, and its results conform relatively well to the results of the model proposed in this study for this case. However, the difference between Yuan model [140] and the model developed in this study reaches a maximum value of 21.25% for $AR = 120$. Additionally, the results of the Yuan model [140] do not approach the infinite cylinder velocities predicted by Khalili and Liu [103] and Huner and Hussey [104] at the highest Reynolds numbers considered (for $70 < AR < 120$ in this case) and are overestimated.

Bent Microfibres

The new model developed in Section 4.4 can also be utilized to estimate the terminal velocity and the horizontal travel distance of V-shaped and curved fibres in the atmosphere. As discussed in Sections 4.2 and 4.4.1, a V-shaped fibre can be assumed to settle at the same rate as a curved fibre with the same diameter, length, and projected area. As a result, the

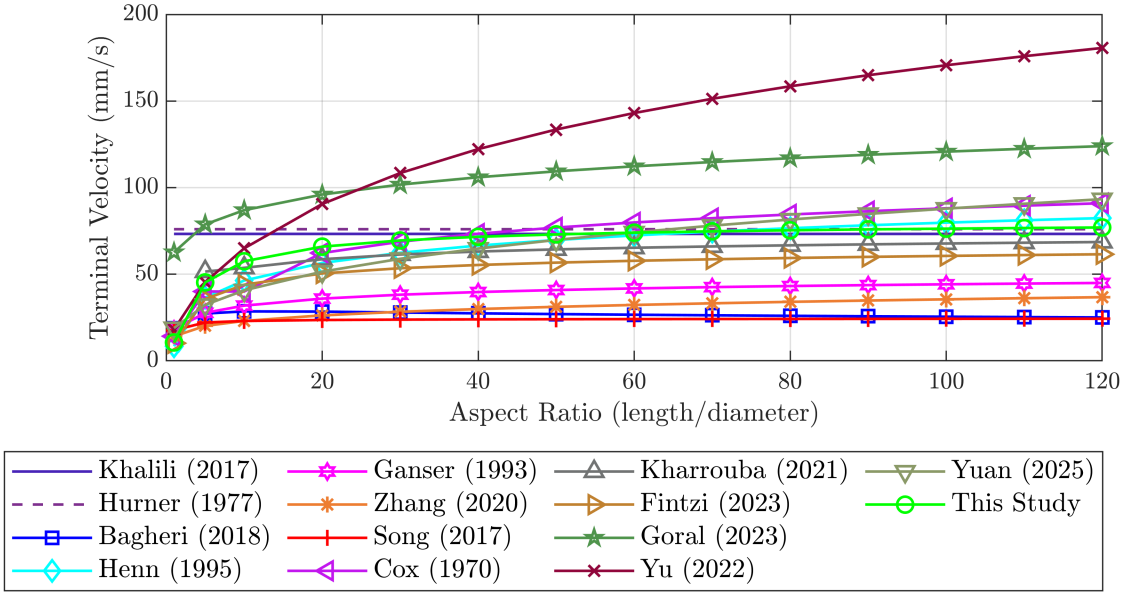

Figure 4.15: Predicted terminal velocity of a straight microfibre with a diameter of 20 µm, aspect ratio between 1 and 120, and density of 1184 kg/m^3 using the new model in the present study and other models.

terminal velocities calculated in this section can be applied to both V-shaped and curved fibres. A typical microfibre made of polyacrylonitrile with a diameter of 20 μm, an aspect ratio of 20, and a density of 1184 kg/m^3, as reported in the sample studied by Wright *et al.* [12], is considered with various bend angles within the ranges investigated in this study. The V-shaped fibre bend angle is assumed to vary between 45° and 135°, resulting in β changing from 0.38 to 0.92 for both V-shaped and curved fibre. The ratio of the terminal velocities of V-shaped or curved fibres to those of straight fibres with the same diameter and aspect ratio has been calculated and plotted at different values of β in figure 4.16. As can be observed in this figure, the terminal velocity ratio of the V-shaped or curved fibre to the straight fibre decreases from 1.37 to 1.03 as β increases from 0.38 to 0.92. Therefore, the larger the bend angle for a V-shaped fibre, the slower the settling rate. Furthermore, this figure shows that a V-shaped or curved fibre always settles faster than a straight fibre of the same size. The

Reynolds number for this fibre decreases from 0.37 to 0.28 as β increases from 0.38 to 0.92. The terminal velocity of a curved fibre has also been calculated using the model introduced in our recent study [50] within the valid range of $\beta > 0.75$ for that model. As can be seen from the figure, the discrepancy between the two models decreases as β increases, with a maximum difference of 12.2% and a mean difference of 7.2% over the range $0.75 < \beta < 0.92$.

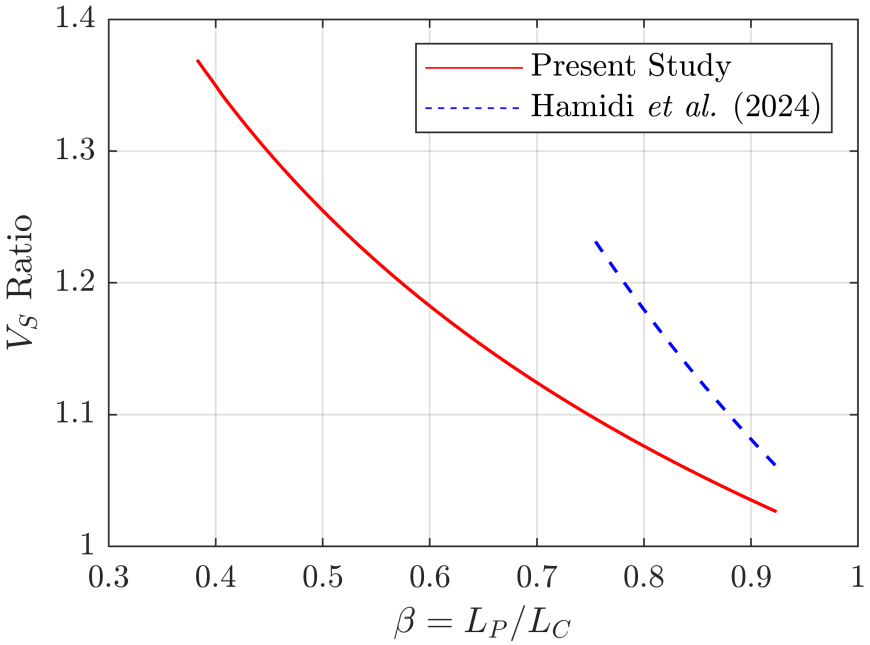

Figure 4.16: Ratio of a V-shaped or curved fibre terminal velocity to that of a straight fibre with $D_C = 20$ μm, $AR = 20$, and $\rho_P = 1184$ kg/m^3 [12] at different values of β. The model for curved fibres developed in our recent study [50] is also included within its valid range of β ($\beta > 0.75$).

The horizontal travel distance of the typical microfibre discussed above has also been calculated and plotted versus the bend angle in figure 4.17. According to Wright *et al.* [12], it is assumed that the fibre is released from a height of 750 m above the ground, which is the height of the daytime atmospheric boundary layer during winter in London, and is exposed to a horizontal wind velocity of 5 m/s. It is further assumed that the fibre travels at the same horizontal velocity as the wind. This figure shows that a V-shaped fibre consistently travels a shorter horizontal distance compared to a straight fibre with the same dimensions before it is

deposited on the ground. This shorter distance is due to the larger vertical terminal velocity of the V-shaped fibre, leading to a shorter residence time in the air than the straight fibre. Moreover, this horizontal travel distance increases with the fibre bend angle, from 41.5 km at $\alpha_0 = 45°$ to 55.4 km at $\alpha_0 = 135°$, approaching the distance traveled by the straight fibre. The horizontal travel distance of the V-shaped fibre is 27% and 2.6% shorter than that of the straight fibre with the same dimensions at $\alpha_0 = 45°$ and $\alpha_0 = 135°$, respectively. The straight fibre travel distance is estimated to be 60 km by Wright *et al.* [12] and 56.9 km by our model, resulting in a difference of 5.4%. The Henn model [69] was used to predict the fibre terminal velocity in the study by Wright *et al.* [12]. Given the sensitivity of the terminal velocity and travel distance of fibres to their geometries, specifically a V-shape in this case, as also noted by Ward *et al.* [29] and Tatsii *et al.* [28], accurate modeling of atmospheric microfibre shape is crucial in simulations for determining their global transport range and deposition rate.

4.5 Chapter Summary

In this chapter, the settling behavior of V-shaped and curved rods was investigated and compared to that of straight rods with identical diameters and aspect ratios at low Reynolds numbers relevant to the atmospheric transport of plastic microfibres. It was found that V-shaped rods consistently settle faster than straight rods due to the inclination of their arms and their reduced projected area. However, existing models for predicting the terminal velocity of inclined cylinders within the Reynolds number range considered in this study were unable to accurately predict the behavior of the V-shaped rods.

When comparing V-shaped and curved rods with the same diameter, aspect ratio, and projected area, differences in terminal velocity were found to be minor. V-shaped rods settle slightly faster than curved ones, with the velocity difference increasing with curvature and reaching a maximum of 4% for a semi-circular shape. The drag coefficient of V-shaped rods generally decreases as the rod is bent from a straight geometry to a 90° bend, due to the dominant effect of increased terminal velocity over changes in projected area. However,

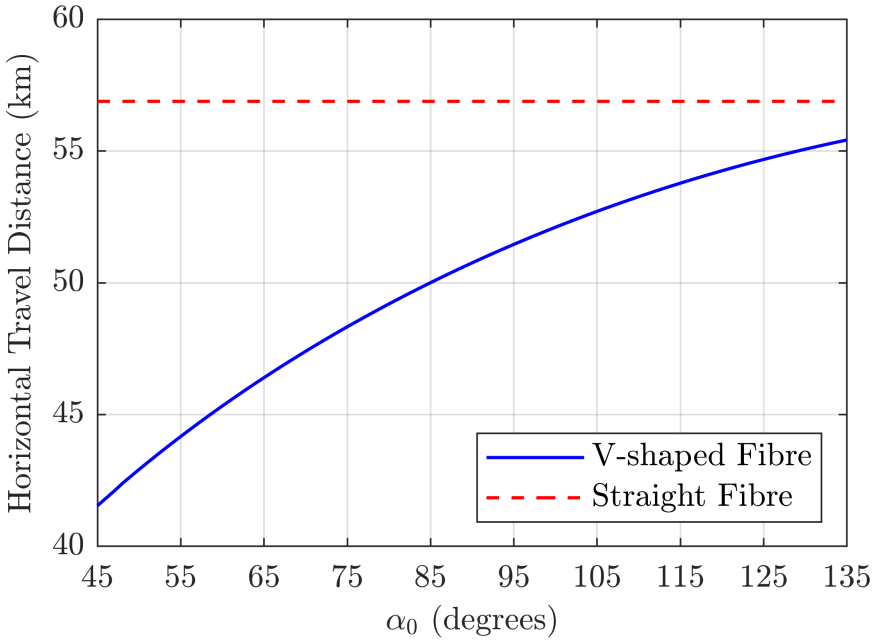

Figure 4.17: Horizontal travel distance of a V-shaped fibre with $D_C = 20$ μm, $AR = 20$, and $\rho_P = 1184$ kg/m^3 varying with bend angle. The fibre is dropped from a height of 750 m above the ground and is exposed to a horizontal wind velocity of 5 m/s. The dashed line shows the horizontal travel distance of a straight fibre with the same D_C and AR as the V-shaped fibre.

bending the rod further from 90° to 45° leads to an increase in drag coefficient, as the projected area has a stronger influence than the terminal velocity in that range.

A new model was developed to predict the drag coefficient and terminal velocity for V-shaped, curved, and straight rods within the ranges of $0.03 < \text{Re} < 5$, $3 < AR < 120$, and $0.64 < \beta < 1$. When compared to experimental data from both this study and a related previous study on straight and curved rods [49], the model yielded a root mean square (RMS) error of 7.1%. This model was also applied to estimate the vertical terminal velocity and horizontal travel distance of typical atmospheric microfibres with curved or V-shaped geometries relative to their straight counterparts. Results show that increasing the bend angle (for V-shaped fibres) or the projected area (for curved fibres) reduces terminal velocity and increases horizontal travel distance, gradually approaching the behavior of straight fibres

with the same diameter and aspect ratio. For instance, bending a straight fibre into a V-shape with a 45° angle resulted in a 27% reduction in horizontal travel distance, highlighting the potential impact of fibre shape on atmospheric deposition predictions.

Chapter 5

Results: Settling of U-Shaped Rods

This chapter presents the experimental results for U-shaped rods settling in a water-glycerin mixture, along with a comparison to straight rods of similar dimensions. The following subsections provide a detailed analysis of the orientation and trajectory of the U-shaped rods during settling, their terminal velocity and drag coefficient, and development of a model to predict vertical terminal velocity and settling orientation of U-shaped rods.

5.1 Rod Orientation and Trajectory

The trajectory and orientation of two different U-shaped rods are illustrated in Figure 5.1, each rod having $D_C = 0.50$ mm and $AR = 60$, one with $\alpha = 0.33$ and the other with $\alpha = 0.67$. In this example, the rod with a smaller middle arm length ratio ($\alpha = 0.33$) exhibits an oblique orientation and a horizontal drift along its trajectory (figure 5.1 (a)), while the rod with a larger middle arm length ratio ($\alpha = 0.67$) showcases a vertical orientation and a vertical trajectory (figure 5.1 (b)). Figure 5.1 (c) shows the variations in the U-shaped rod inclination angle along the corresponding vertical locations in figures 5.1 (a) and (b). For $\alpha = 0.33$ and $\alpha = 0.67$, the average inclination angles are 60° and 89° with standard deviation to mean ratios of 1.44% and 0.39%, respectively. Given negligible variations, we can assume that the rods have asymptoted to stable orientations.

The middle arm introduces asymmetry to the geometry of a U-shaped rod when viewed

from the side, resulting in an oblique orientation and horizontal drifts under specific conditions. In addition to the middle arm length ratio, the Reynolds number also affects the U-shaped rod orientation. At low Reynolds numbers, similar to the behavior of asymmetric straight rods outlined by Khayat and Cox [100] and Roy *et al.* [117], the inclination angle of U-shaped rods after achieving terminal velocity is determined by the interplay between inertial torque, acting on the side arms, and gravitational torque, resulting from the asymmetry caused by the middle arm. Figure 5.2 illustrates a phase map showing the orientation of the U-shaped rods, either oblique or vertical, based on the Reynolds number and middle arm length ratio. In this map, inclination angles greater than 80° are considered vertical orientation, while angles smaller than this value are considered oblique. Similar to the conclusions drawn by Roy *et al.* [117] and Jiang *et al.* [118] for asymmetric straight rods and spheroids, respectively, our observations indicate that a U-shaped rod takes on an oblique orientation for middle arm length ratios less than a critical value for a given Re, and for Reynolds numbers above a critical value for a given α. Therefore, the increased inertial effects, represented by the Reynolds number, favor an oblique U-shaped rod orientation at higher Re values, whereas the effect of asymmetry, represented by the middle arm length ratio, favors a vertical rod orientation. The dashed line in Figure 5.2 demarcates the two orientations, showing a positive correlation between the critical Re and α.

5.2 Terminal Velocity Components

The vertical component of the U-shaped rods' terminal velocity for various diameters, aspect ratios, and middle arm length ratios, as specified in table 3.4, was determined. Figure 5.3 shows the variations in the vertical terminal velocity and inclination angle of the U-shaped rods made of brass with $D_C = 0.50$ and 0.81 mm with aspect ratio and middle arm length ratio. The trend in the vertical velocity of the aluminum rods with $D_C = 1.02$ mm resembles that of the brass rods with $D_C = 0.50$ mm due to the similarity of the Reynolds number range (see table 3.4), and is not shown in this figure. Figure 5.3 (a) shows that with an

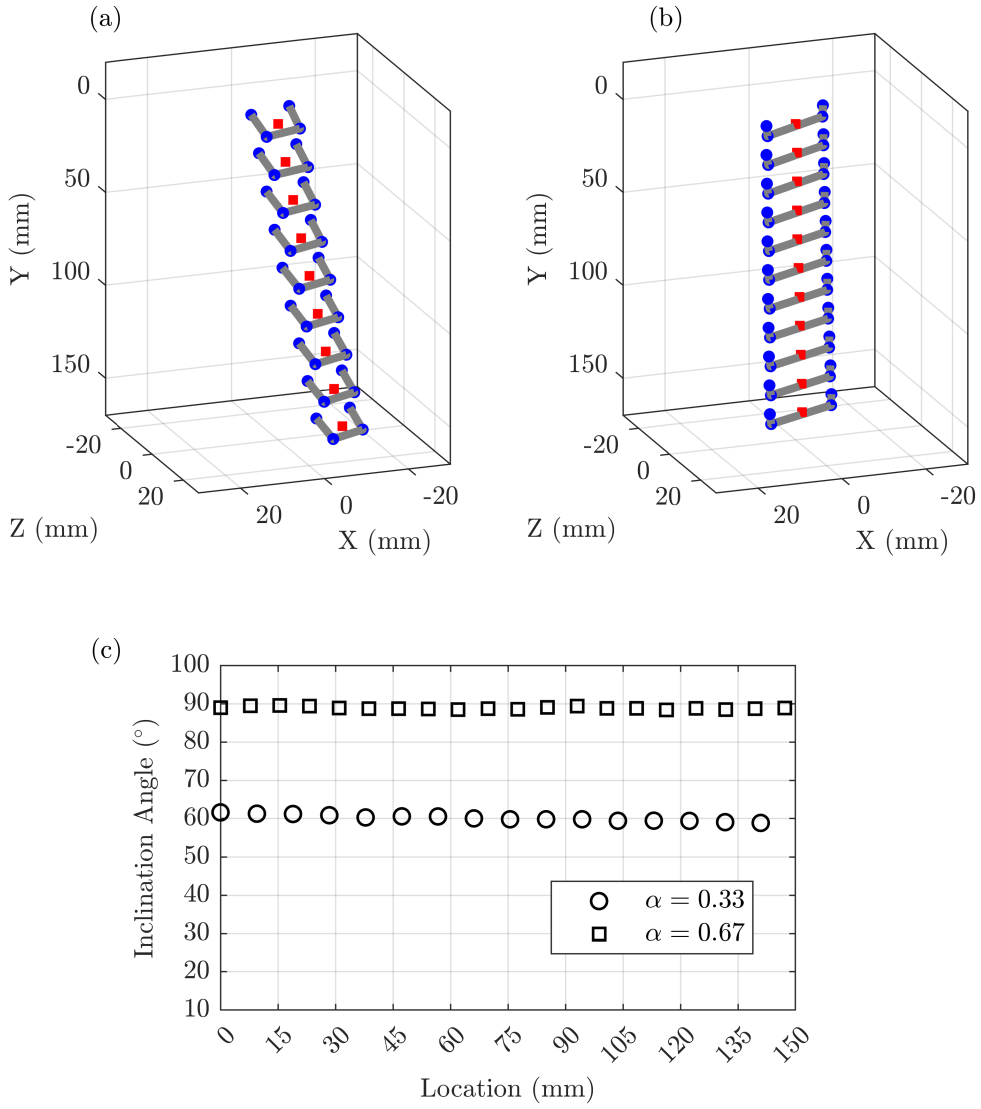

Figure 5.1: Three-dimensional fall trajectory of a U-shaped rod with (a) $D_C = 0.50$ mm, $AR = 60$, and $\alpha = 0.33$, and (b) $D_C = 0.50$ mm, $AR = 60$, and $\alpha = 0.67$. Panel (c) shows the variations in the inclination angle with the vertical location of the rod centroid along the trajectory for the cases shown in (a) and (b).

increase in the rod aspect ratio, the vertical velocity of the U-shaped rod with $D_C = 0.5$ mm increases within $30 < AR < 50$, peaks at $AR = 50$, and decreases within $50 < AR < 90$ [52]. However, the U-shaped rod with $D_C = 0.81$ mm exhibits an almost constant vertical terminal velocity across all aspect ratios in the range $30 < AR < 90$. The reason for these two different

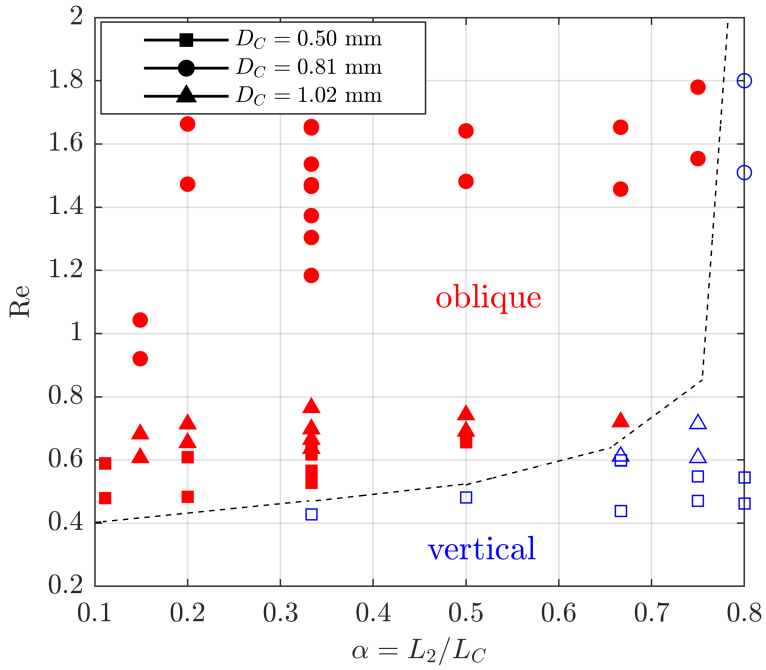

Figure 5.2: Orientation phase map for U-shaped rods. The filled and hollow markers show oblique and vertical orientations, respectively. The dashed line separates the two orientations.

behaviors can be attributed to the variations in the inclination angle. For $D_C = 0.50$ mm, the inclination angle changes from 88° (roughly vertical orientation) to 40° (oblique orientation) as the aspect ratio increases from 30 to 90. For a constant α, increasing the aspect ratio corresponds to a relative elongation of the side arms, which tends to increase the rod vertical terminal velocity and Reynolds number due to the overall increase in rod length. However, as the Reynolds number increases, inertial torque becomes more dominant and outweighs the influence of rod asymmetry, leading to a more horizontal orientation of the side arms during settling. This orientation reduces the vertical velocity. As a result, the vertical settling velocity of the U-shaped rod reflects a balance between increasing rod length and increasing inclination angle, leading to an initial rise, a peak, and a subsequent decline in velocity with increasing aspect ratio. For $D_C = 0.81$ mm, the inclination angle varies only from 41° (oblique) to 24° (oblique), which is much narrower compared to $D_C = 0.5$ mm. This behavior

may be attributed to the higher Reynolds number and the resulting inertial effects, which cause the rod to maintain a more oblique orientation with smaller variation over a narrower range. Due to the smaller changes in inclination angle and the trade-off between rod size and orientation, as discussed above, the vertical terminal velocity of the U-shaped rod with $D_C = 0.81$ mm remains nearly constant across the entire aspect ratio range of $30 < AR < 90$. The transition from vertical to oblique orientation for $D_C = 0.50$ mm can also be observed in figure 5.2, where some data points exhibit both oblique and vertical orientations. In contrast, for $D_C = 0.81$ mm, the corresponding data points lie farther from the boundary between the two regimes and exhibit exclusively oblique orientation. Additionally, Figure 5.3 shows that the vertical terminal velocity of a U-shaped rod consistently exceeds that of a straight rod with the same diameter and aspect ratio, with the difference ranging from 10% to 45% across the studied parameter space. This consistent difference is explained by the persistent non-zero inclination angle of U-shaped rods, which contributes to their enhanced vertical velocity relative to straight rods.

Figure 5.3 (b) illustrates the variations in vertical terminal velocity with the U-shaped rod middle arm length ratio for brass rods at diameters of 0.50 and 0.81 mm and aspect ratios of 60 and 90. The interplay between the rod size and orientation determines the vertical velocity as the middle arm length ratio changes for a given D_C and AR. A higher α value means a relatively shorter side arm, which leads to a decrease in the vertical velocity. However, the side arms become more vertically aligned with an increase in α due to the greater influence of the asymmetry of the bottom-heavy U-shape. For $AR = 60$, the inclination angle of the U-shaped rod with $D_C = 0.50$ mm increases from 37° (oblique) to 90° (vertical) as the middle arm length ratio changes only from 0.20 to 0.50. This transition from oblique to vertical orientation occurs over a much narrower range of α compared to the rod with $D_C = 0.81$ mm, whose inclination angle increases from 19° (oblique) to 90° (vertical) as α changes from 0.20 to 0.80. The difference in the behavior of the inclination angle with α between these two cases can be attributed to the higher inertial effects in the larger rod diameter, which

help maintain the rod in an oblique orientation over a wider range of α. As a result, the vertical velocity of the rod with $D_C = 0.50$ mm initially increases within $0.11 < \alpha < 0.33$, peaks at $\alpha = 0.33$, and decreases within $0.33 < \alpha < 0.80$, while the vertical velocity of the rod with $D_C = 0.81$ mm remains almost constant over the entire range of $0.20 < \alpha < 0.80$. The variation of vertical terminal velocity with α for rods with an aspect ratio of 90, with diameters of 0.50 mm and 0.81 mm, shows trends consistent with those previously observed for rods with an aspect ratio of 60. The only difference is that for $D_C = 0.50$ mm, the peak in vertical velocity occurs at a higher α ($\alpha = 0.50$ for $AR = 90$ compared to $\alpha = 0.33$ for $AR = 60$), indicating the stronger effects of inertia for the higher aspect ratio, which causes the oblique orientation for a wider range of α.

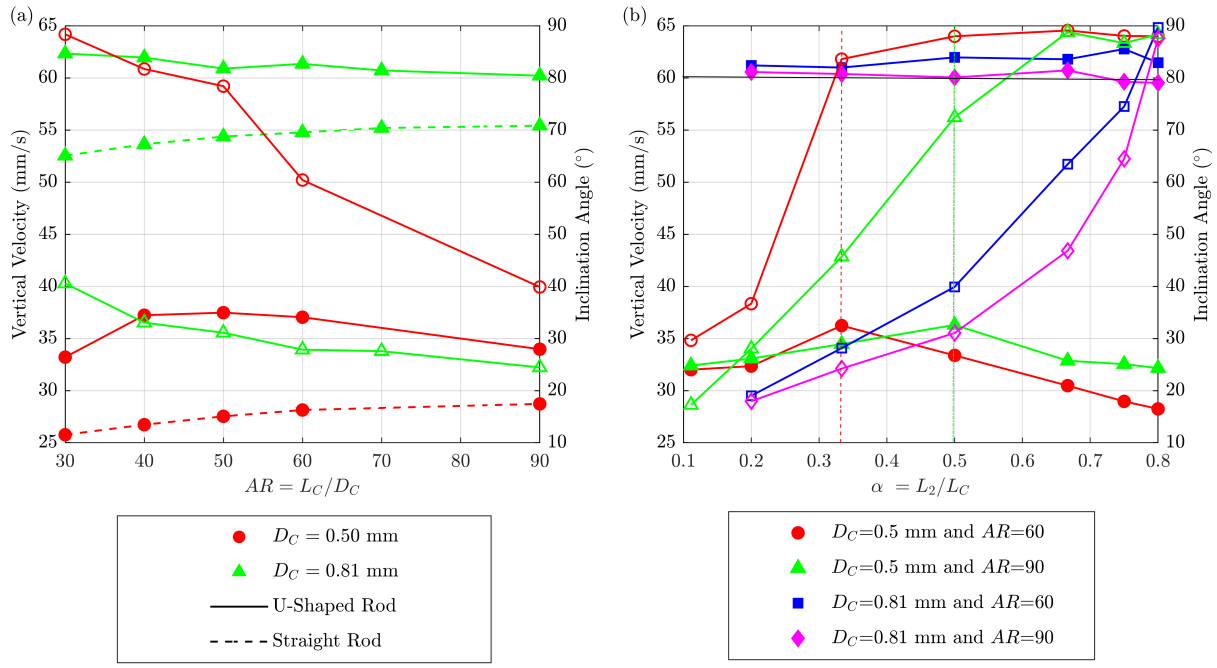

Figure 5.3: Variations in vertical terminal velocity and inclination angle of U-shaped brass rod with (a) aspect ratio for $\alpha = 0.33$ and with (b) middle arm length ratio for $AR = 60$ and 90. The filled and hollow symbols represent the vertical velocity and inclination angle, respectively. The red dashed and green dot-dashed lines in panel (b) illustrate the link between the peak vertical velocity for $D_C = 0.50$ mm and its corresponding inclination angle for $AR = 60$ and 90, respectively. The solid black line in panel (b) shows $\theta = 80°$. The rod orientation above and below this line is considered vertical and oblique, respectively.

Figure 5.4 shows the variations in the horizontal velocity ratio of U-shaped brass rods (denoted by V_H/V_S, where V_H and V_S are the horizontal and total velocity of the rod) with aspect ratio. As illustrated in figure 5.1 (a), when the U-shaped rods settle obliquely, they experience a horizontal drift toward the side where the middle arm is positioned. This horizontal movement occurs due to the asymmetry in the flow around the oblique U-shaped rod, pushing the rod towards the middle arm, which is the heavier region of asymmetric mass distribution, when viewed from the side. This horizontal drift is consistent with the behavior of straight rods with a non-uniform mass distribution along their axis, which drift horizontally towards the heavier end [117, 121, 122]. Furthermore, the horizontal velocity ratio is strongly correlated with the inclination angle. While the horizontal velocity ratio increases significantly from 0.02 to 0.19 as the aspect ratio changes from 30 to 90 for $D_C = 0.50$ mm, it only varies slightly around 0.19 for $D_C = 0.81$ mm. This can be attributed to the changes in inclination angles for these two cases.

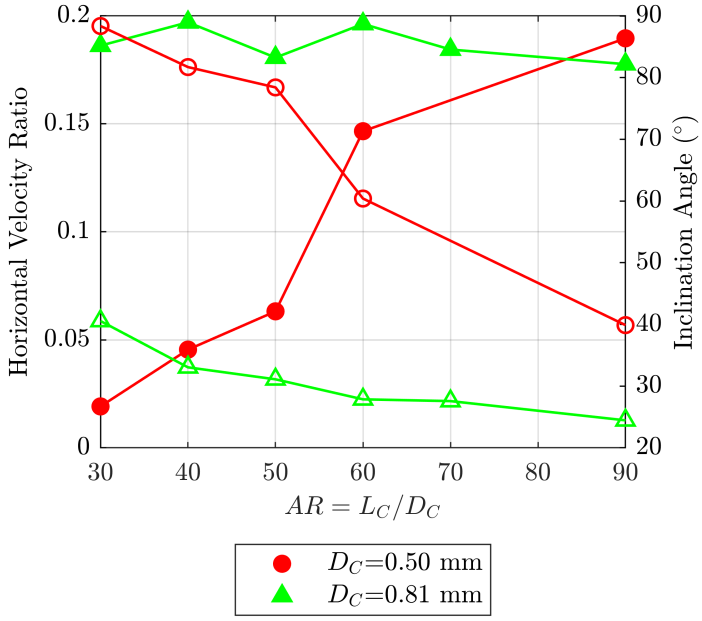

Figure 5.4: Variations in the horizontal velocity ratio (V_H/V_S) with aspect ratio for U-shaped brass rods with $\alpha = 0.33$. The filled and hollow symbols represent the terminal velocity and inclination angle, respectively.

Figure 5.5 illustrates how the horizontal velocity ratio varies with middle arm length ratio for U-shaped brass rods. Due to the similarity in the range of Reynolds number based on table 3.4, the trend observed for aluminum rods with $D_C = 1.02$ mm is similar to that of the brass rods with $D_C = 0.50$ mm and is therefore not shown in figures 5.4 and 5.5. In all cases, the horizontal velocity ratio reaches its peak at an α value of either 0.20 or 0.33. For lower inertia, associated with smaller diameters and aspect ratios, the transition from oblique to vertical orientation occurs over a narrower range of α, resulting in a significant drop in the horizontal velocity ratio. However, for larger diameters and higher aspect ratios, the changes in inclination angle and horizontal velocity ratio are more gradual due to the impacts of inertia. As an example, for $D_C = 0.50$ mm and $AR = 60$, the orientation angle undergoes a significant increase from 37° (oblique) to 84° (roughly vertical) as α changes from 0.20 to 0.33. This shift in inclination angle results in the horizontal velocity ratio decreasing from 0.21 to 0.05 over the same change in α. However, for $D_C = 0.50$ mm and $AR = 90$, the inclination angle has a more gradual change from 28° (oblique) to 87° (vertical) as α varies from 0.20 to 0.67, resulting in a more gradual decrease in the horizontal velocity ratio from 0.21 to 0.06 across the same range of α. A similar comparison can be made between the two aspect ratios for $D_C = 0.81$ mm. The horizontal drift velocity approaches zero when the U-shaped rod assumes a vertical orientation. The fact that the U-shaped rod horizontal velocity peaks at a specific level of asymmetry conforms to the observation of Roy *et al.* [117] and Jiang *et al.* [118] for asymmetric cylindrical rods and spheroids, respectively. Jiang *et al.* [118] found that the maximum horizontal drift angle of an asymmetric prolate spheroid depends only on the aspect ratio. This angle increases with the aspect ratio, approaching an asymptote of 19° at very high aspect ratios. Based on our observations, the horizontal velocity ratio of U-shaped rods does not exceed 0.2. It peaks at an α value between 0.20 and 0.33 and then decreases with further increase in α.

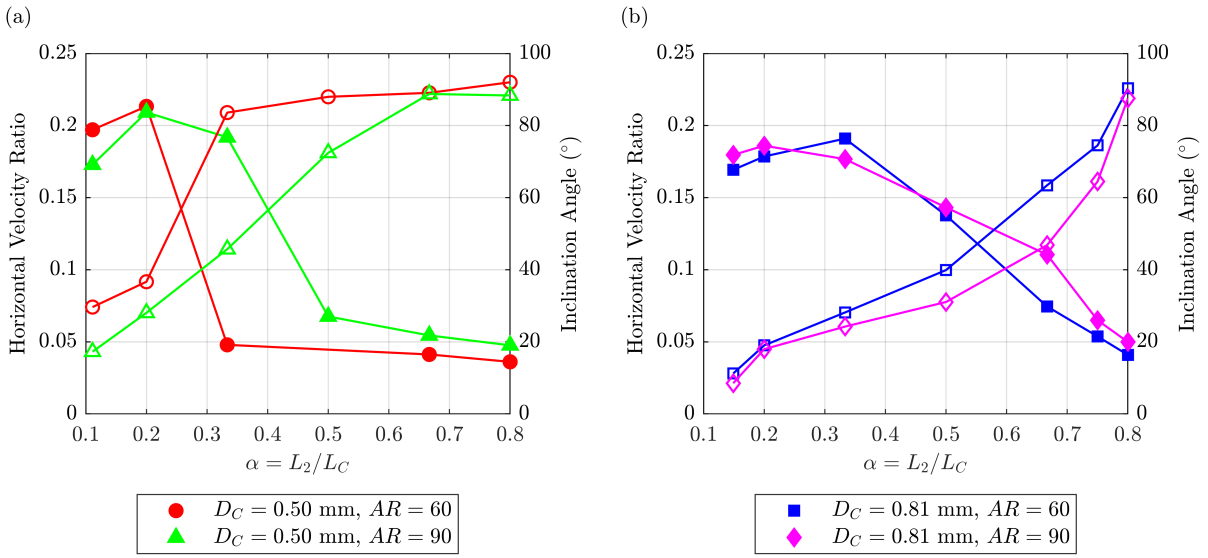

Figure 5.5: Variations in the horizontal velocity ratio (V_H/V_S) with middle arm length ratio for U-shaped brass rods with (a) $D_C = 0.50$ mm and (b) $D_C = 0.81$ mm. The filled and hollow symbols represent the horizontal velocity ratio and inclination angle, respectively.

5.3 Drag Coefficient

This section examines the variations in the drag coefficient of U-shaped rods with Reynolds number and other geometric parameters, including aspect ratio and middle arm length ratio, and compares these with straight rods of the same dimensions. The Reynolds number is calculated from

$$\mathrm{Re} = \frac{\rho_f V_V D_{eq}}{\mu_f}, \tag{5.1}$$

where V_V is the vertical component of the terminal velocity of the U-shaped rod. The drag coefficient is calculated from

$$C_D = \frac{(\rho_P - \rho_f) g (\pi/4) D_C^2 L_C}{0.5 \rho_f V_V^2 A_P}, \tag{5.2}$$

The drag coefficient used for the U-shaped rods is based on the vertical component of the total aerodynamic force force, which is balanced by the downward gravitational force and

the upward buoyancy force. In figure 5.6, A_P is calculated using two methods: one based on the projected length of the U-shaped rod on a horizontal plane (L_P) and the other based on the total length of the rod (L_C). L_P for a U-shaped rod with an inclination angle of θ is calculated from

$$L_P = \alpha L_C D_C + (1 - \alpha) L_C D_C \cos(\theta). \tag{5.3}$$

Based on the results illustrated in figure 5.6, the drag coefficient of the U-shaped rod consistently decreases with the Reynolds number if the projected area is defined based on the projected length. Therefore, this definition for A_P will be considered for the following analyses in this chapter.

The drag coefficient of a U-shaped rod can be either smaller or larger than that of a straight rod with the same diameter and aspect ratio. It depends on the trade-off between A_P and V_V^2 in equation 5.2 since a U-shaped rod consistently has a larger terminal velocity and a smaller projected area compared to a straight rod of the same dimensions (figure 5.3). As an example, for $D_C = 0.50$ mm, U-shaped rods of $AR = 30,\ 40,$ and 50, having inclination angles of $88°,\ 82°,$ and $78°$ respectively, exhibit higher drag coefficients compared to the straight rods of the same dimensions. For these cases, where the rod orientation is close to vertical, A_P exerts a greater influence on the drag coefficient, leading to a larger drag coefficient for $AR = 30,\ 40,$ and 50. However, for $AR = 60$ and 90 having $\theta = 60°$ and $40°$ respectively, the U-shaped rod is more oblique, associated with a smaller θ, and has a larger projected area. For these two oblique orientations, the rod vertical velocity becomes more influential, resulting in a reduced drag coefficient for the U-shaped rod compared to the straight rod. As observed for the brass rods with $D_C = 0.81$ mm, the drag coefficient of the U-shaped rod is consistently smaller than that of the straight rod due to the oblique orientation and the greater influence of the vertical velocity relative to the projected area.

Figure 5.7 shows the variations in the U-shaped rod drag coefficient and inclination with middle arm length ratio. This figure shows that C_D increases with α when the U-shaped

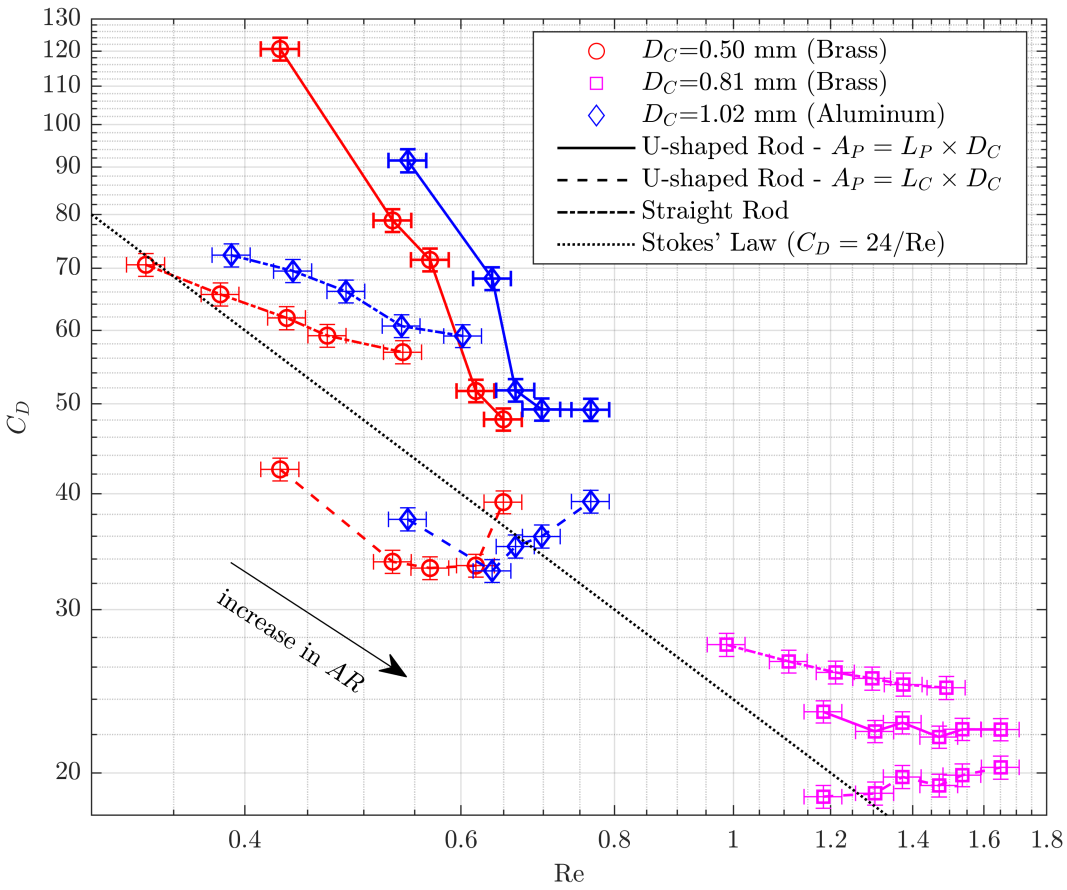

Figure 5.6: Variations in the drag coefficient of U-shaped and straight rods with Reynolds numbers at different diameters and aspect ratios. For U-shaped rods, where $\alpha = 0.33$, the drag coefficient is calculated using two projected areas: one based on the rod projected length (L_P) and the other based on the total rod length (L_C).

rod is oriented obliquely and decreases with α when the rod is oriented vertically. For instance, for $D_C = 0.50$ mm and $AR = 60$, the drag coefficient increases from 49.7 to 87.3 and the inclination angle changes over $30° < \theta < 84°$ (oblique orientation) as α changes from 0.11 to 0.33. However, the drag coefficient decreases from approximately 87 to 65, and the inclination angle varies from 84° to 90° (vertical orientation) as α increases from 0.33 to 0.80. The drag coefficient peaks at $\alpha = 0.67$ for $D_C = 0.50$ mm and $AR = 90$, which is larger than the corresponding α for $AR = 60$ due to greater inertial effects. Furthermore, C_D consistently increases with α for both ARs of 60 and 90 for $D_C = 0.81$ mm owing to their

oblique orientation over the entire range of $0.2 < \alpha < 0.8$.

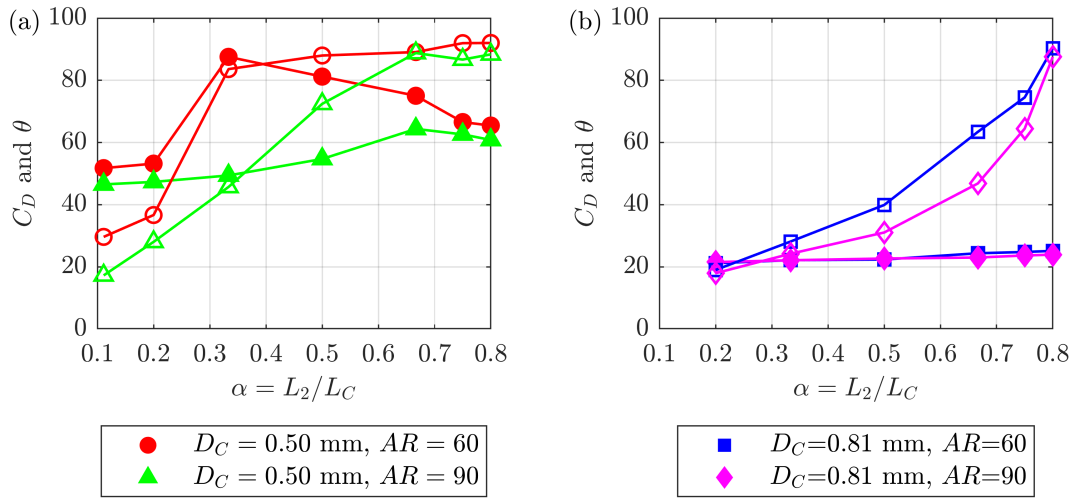

Figure 5.7: Variations in the drag coefficient of U-shaped brass rods with α for diameters of (a) $D_C = 0.50$ mm and (b) $D_C = 0.81$ mm. The filled and hollow symbols represent the drag coefficient and inclination angle, respectively.

5.4 Model Development and Comparison

In this section, a model is developed to predict the drag coefficient and vertical terminal velocity of U-shaped rods. As mentioned in Section 5.3, to achieve more consistent behavior in the trend of C_D, the projected area of the U-shaped rod on a horizontal plane should be calculated based on the rod projected length (equation 5.3), which is a function of the inclination angle. According to Figure 5.3 (a), the inclination angle of the U-shaped rod decreases with an increase in aspect ratio, while it increases with an increase in the middle arm length, as shown in Figure 5.3 (b). Based on the orientation map shown in Figure 5.2, U-shaped rods tend to reorient from vertical to oblique as the Reynolds number increases, resulting in a decrease in the inclination angle. Furthermore, the results demonstrate that the relationship between C_D and the aforementioned variables, AR, Re, and α, tend to follow a power law. Therefore, the general model considered for the U-shaped rod inclination angle is

$$\theta = a_1 \frac{\alpha^{b_1}}{AR^{c_1}\mathrm{Re}^{d_1}}. \tag{5.4}$$

This model was fitted to the inclination angle data points obtained in this study, and the coefficients of a_1, b_1, c_1, and d_1 were determined as 712.09, 1.03, 0.43, and 0.70, respectively. The RMS error of this model, when used to calculate the projected area of the U-shaped rods, is 6%.

The drag coefficient model for U-shaped rods is based on the framework developed by Song *et al.* [38], as presented in equation 2.10, which was developed for the settling of particles with various geometries and orientations. Our proposed model is given by

$$C_D = \frac{24}{\mathrm{Re}AR^{c_2}\phi^{d_2}S^{e_2}}(1 + a_2\mathrm{Re})^{b_2}, \tag{5.5}$$

where ϕ and S are the U-shaped rod sphericity and projected area ratio, respectively. Sphericity is calculated from equation 4.7. As explained in Section 4.4, AR was included, relative to the model by Song *et al.* [38], to improve the fit for straight cylindrical rods. Furthermore, our new model for U-shaped rods incorporates S, which is defined as the ratio of the projected area of the volumetric-equivalent sphere to that of the U-shaped rod. The reason for including this term, as explained in Section 5.1, is that, unlike the straight, curved, and V-shaped rods, the orientation of the U-shaped rod is not fixed and depends on other variables and parameters, including Re, AR, and α. This behavior of the U-shaped rod orientation affects the drag coefficient, as described in Section 5.3. S for the U-shaped rods is calculated from

$$S = \frac{\frac{\pi}{4}D_{eq}^2}{L_P D_C}, \tag{5.6}$$

where L_P is calculated from equation 5.3. By fitting equation 5.5 to the experimental data obtained for U-shaped rods, the coefficients of a_2, b_2, c_2, d_2, and e_2 were determined as 4.87, 0.27, 1.31, 5.54, and -0.77, respectively. The new models (equations 5.4 and 5.5) were

utilized to calculate the vertical velocity of the U-shaped rods settling in the glycerin mixture investigated in this research through an iterative solution method, as outlined by Song *et al.* [38]. The results of these calculations are compared with the experimental data in figure 5.8, yielding an RMS error of 7.2% for our model. The experimental data in figure 5.8 were corrected utilizing the correction factors introduced by Brenner [134] to account for the impacts of the chamber bounded walls [50, 99]. Our new model is valid within the ranges of this research, including $30 < AR < 90$, $0.10 < \alpha < 0.80$, and $0.43 < \mathrm{Re} < 1.78$.

Additionally, our experimental results are compared with the results of the models by Kharrouba *et al.* [41], Fintzi *et al.* [138], and Khayat and Cox [100] in figure 5.8. These models were used to calculate the total vertical drag force applied to the three arms of the U-shaped rods. For the U-shaped rods oriented obliquely, the angle of the inclined arms relative to the flow, denoted by λ, is considered in the calculations when using these models. This angle is shown in figure 5.9 and is calculated from

$$\lambda = \frac{\pi}{2} - \theta - \gamma. \tag{5.7}$$

In equation 5.7, θ is the rod inclination angle obtained from the experiments. γ is the angle of the rod velocity vector and is calculated from $\sin^{-1}(V_H/V_S)$, where V_H and V_S are experimentally determined. Figure 5.10 illustrates the forces acting on the side and middle arms of a U-shaped rod. $F_{\parallel}$ and $F_{\perp}$ represent the components of the drag force parallel and perpendicular to the inclined side arm axis, respectively. F_V, F_H, F_G, and F_B denote the vertical and horizontal components of the drag force, as well as the gravitational and buoyancy forces, respectively. Subscripts 1 and 2 refer to the side and middle arms, respectively. The total drag force on the U-shaped rods in the vertical direction ($F_{V,t}$) is calculated by summing the vertical components of the drag forces acting on the three arms: two on the inclined side arms and one on the horizontal middle arm. This is given by

$$F_{V,t} = 2(F_{\parallel 1} \sin\theta + F_{\perp 1} \cos\theta) + F_{\perp 2}. \tag{5.8}$$

The vertical velocity of the U-shaped rod is then determined by balancing the gravitational, buoyancy, and drag forces acting on the rod, using an iterative solution. This force balance is expressed as

$$F_{V,t} = 2(F_{G1} - F_{B1}) + (F_{G2} - F_{B2}). \tag{5.9}$$

This iterative process is repeated to determine a vertical velocity for each of the three models previously mentioned. In the case of a vertically oriented U-shaped rod, λ is zero, and the total drag force is calculated by adding up the two drag forces applied to the vertical side arms and the one applied to the horizontal middle arm. Furthermore, for an oblique rod, the total horizontal drag force is given by

$$F_{H,t} = 2(F_{\perp 1} \sin\theta - F_{\parallel 1} \sin\theta). \tag{5.10}$$

This force is ultimately counterbalanced by the horizontal force exerted by the fluid once the rod reaches its terminal velocity; therefore, no horizontal acceleration occurs.

Figure 5.8 demonstrates that the models by Kharrouba *et al.* [41], Fintzi *et al.* [138], and Khayat and Cox [100] result in predictions of the vertical velocity that significantly differ from the measured values in this research. The RMS errors for the models by Kharrouba *et al.* [41], Fintzi *et al.* [138], and Khayat and Cox [100] were calculated as 12.8%, 18.0%, and 31.8%, respectively. In applying these models, the drag forces on the three arms are calculated separately, and the connections between them are ignored. This may limit their ability to accurately predict the terminal velocity. Additionally, each model cannot predict the inclination angle, which was measured and used to apply the model.

5.5 Application of the Model to Atmospheric U-Shaped Microfibres

The new model can predict the vertical velocity of U-shaped microplastic fibres distributed

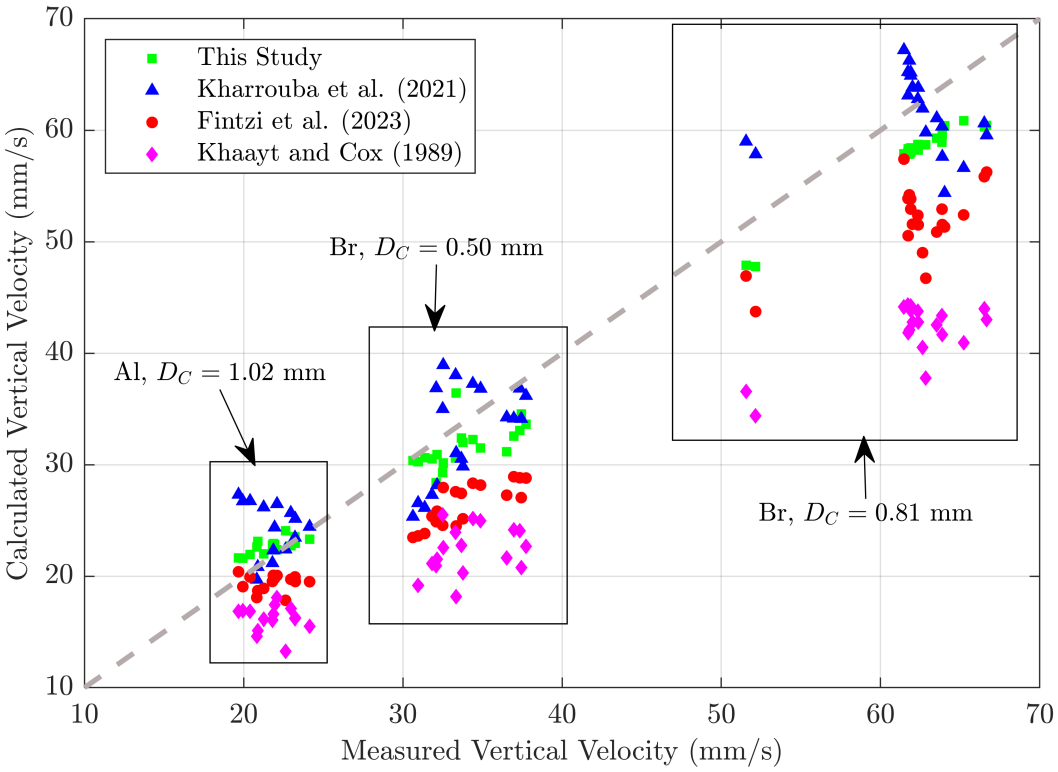

Figure 5.8: The vertical velocities of U-shaped rods settling in a water-glycerin mixture with a glycerin weight ratio of 90% calculated from the models proposed in this research (equations 5.4 and 5.5) as well as the models by Kharrouba *et al.* [41] and Fintzi *et al.* [138] versus the measured vertical velocities from the experiments.

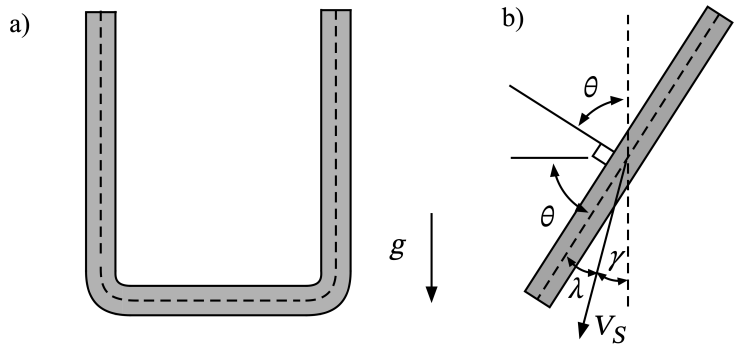

Figure 5.9: Flow angle (λ) utilized to calculate the vertical drag force acting on the inclined arms of U-shaped rods at oblique orientations in the models of Kharrouba *et al.* [41], Fintzi *et al.* [138], and Khayat and Cox [100]. γ and θ represent the velocity vector and rod inclination angles, respectively.

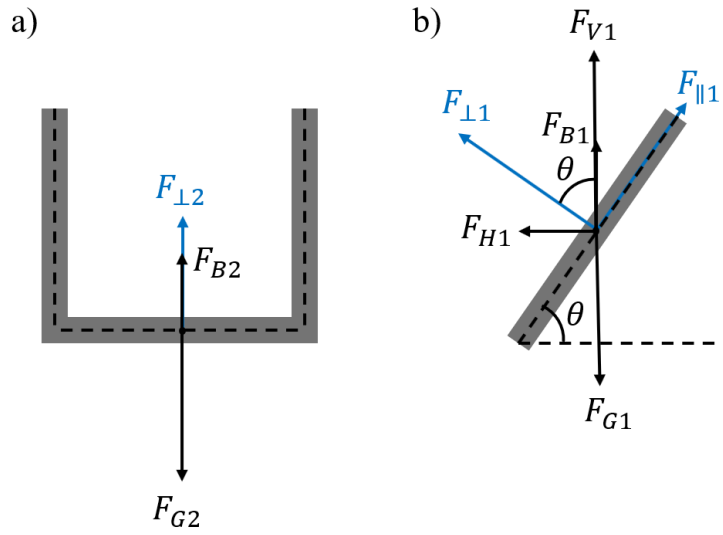

Figure 5.10: Force body diagram of a U-shaped rod oriented obliquely during settling. Panels (a) and (b) illustrate the forces applied to the middle and one side arm, respectively. $F_{\parallel}$ and $F_{\perp}$ are the drag components parallel and perpendicular to the inclined side arm. F_V, F_H, F_G, and F_B denote the vertical drag force, horizontal drag force, gravitational force, and buoyancy force, respectively. Subscripts 1 and 2 refer to the side and middle arms, respectively.

through the atmosphere. The residence time of these fibres in the atmosphere can be calculated by dividing their initial height by their vertical velocity. Wright *et al.* [12] investigated a representative straight microplastic fibre with a diameter of 20 μm in their study. In this section, a fibre with the same diameter and two representative aspect ratios, 30 and 60, which fall within the range commonly observed in atmospheric depositions, are assumed. The influence of a U-shaped geometry on the vertical velocity of the fibre is evaluated across a range of α.

Figure 5.11 (a) and (b) illustrate the variations in the vertical velocity with middle arm length ratio for $AR = 30$ and 60, respectively. The vertical velocity of the microfibres with $AR = 30$ and 60 reaches a peak at $\alpha = 0.31$ and 0.46, respectively. These values of α also correspond to the transition of the U-shaped microfibre from an oblique to a vertical orientation according to figure 5.11 (e) and (f). As discussed in Section 5.2, the higher inertial effects, associated with the larger aspect ratio, tend to maintain the rod at an oblique

orientation, resulting in a larger value of α corresponding to the transition in orientation and the maximum vertical velocity across the studied range of α. Figures 5.11 (c) and (d) show the ratio of the vertical terminal velocity and drag coefficient of a U-shaped microfibre to those of a straight microfibre with the same diameter and aspect ratio. Figure 5.11 (c) indicates that the U-shaped microfibres consistently settle faster than straight microfibres with the same diameter and aspect ratio, with maximum differences of 28% and 15% for $AR = 30$ and 60, respectively. The model proposed in Section 4.4 developed for straight, V-shaped, and curved rods has been utilized to calculate the terminal velocity of straight fibres. The differences in vertical velocities, combined with the horizontal drift of U-shaped fibres, can significantly influence their residence time in the atmosphere, as well as their travel distance and dispersion. These findings underscore the significance of a U-shaped geometry in the transport of fibres in the atmosphere. Similar to the trends shown in Section 5.3, figure 5.11 (c) and (d) show that the ratio of U-shaped microfibre drag coefficient to that of a straight microfibre with the same dimensions increases with α when the microfibre has an oblique orientation, corresponding to $\alpha < 0.31$ for $AR = 30$ and $\alpha < 0.46$ for $AR = 60$. However, once the microfibre orients vertically as a result of an increase in α, the drag coefficient ratio decreases with further increases in α. The terminal velocity and drag coefficient of the straight microfibres were calculated using the model proposed in Section 4.4.

5.6 Chapter Summary

In this chapter, the results of the settling of U-shaped brass and aluminum rods in a quiescent water-glycerin mixture were discussed. The observations show that a U-shaped rod can take either vertical or oblique orientations depending on the Reynolds number and middle arm length ratio. This orientation shifts from vertical to oblique when the Reynolds number exceeds a critical value or when the middle arm length ratio falls below a critical value.

The vertical velocity of a U-shaped rod is determined by the interplay between the length and orientation of the side arms. The vertical velocity either peaks at a specific value of

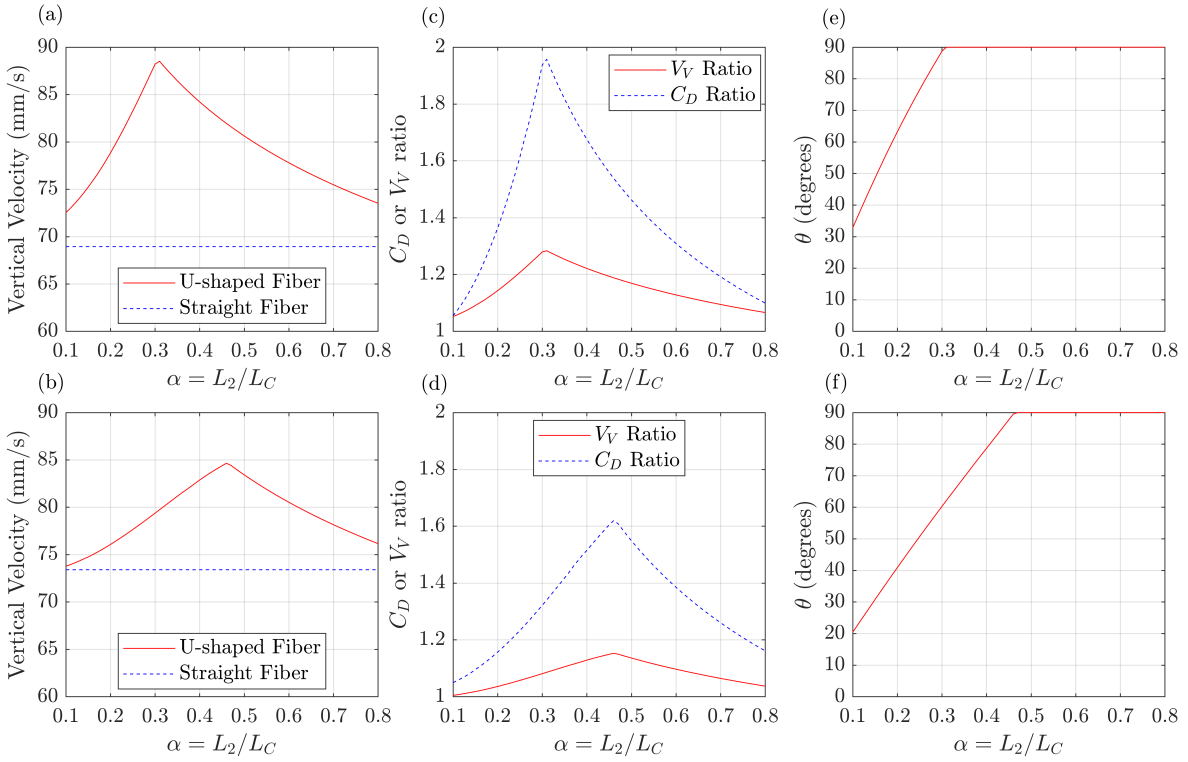

Figure 5.11: Modelled Variations in vertical velocity, drag coefficient, and inclination angle of a U-shaped microfibre with $D_C = 20$ μm and $AR = 30$ in (a), (c), and (e) and $AR = 60$ in (b), (d), and (f) with respect to the middle arm length ratio. Panels (a) and (b) show the U-shaped microfibre vertical velocity, (c) and (d) show the ratio of the U-shaped microfibre vertical velocity and drag coefficient to those of a straight microfibre with the same dimensions, and (e) and (f) show the inclination angle of the U-shaped microfibre.

the rod aspect ratio and middle arm length ratio or remains constant as the aspect ratio or middle arm length ratio varies, depending on the Reynolds number and inertial effects. For a given diameter, the maximum vertical velocity occurs at a higher middle arm length ratio for a larger aspect ratio due to stronger inertial effects. The horizontal velocity ratio of a U-shaped rod is primarily affected by the rod inclination angle. As the orientation of the rod approaches vertical, the horizontal velocity ratio decreases significantly. In general, the horizontal velocity ratio increases with the aspect ratio because of a consistent decrease in the inclination angle, making the rod more oblique. However, it peaks at a value of 0.2 for a

middle arm length ratio between 0.2 and 0.3. Higher inertial effects at larger diameters and aspect ratios lead to more gradual changes in both the inclination angle and the horizontal velocity ratio compared to cases with lower inertia.

The drag coefficient of a U-shaped rod, calculated based on the projected length, is higher than that of a straight rod with the same dimensions when oriented vertically, due to the greater influence of the projected area compared to the vertical velocity. However, for oblique orientations, the straight rods have a larger drag coefficient due to the dominance of the rod vertical velocity over the projected area. The drag coefficient of a U-shaped rod has a positive correlation with the middle arm length ratio for oblique orientations and a negative correlation for vertical orientations, due to the trade-off between the projected area (A_P) and the square of the vertical velocity (V_V^2) in the drag coefficient calculations.

New models were developed to predict the inclination angle, drag coefficient and vertical terminal velocity of U-shaped rods. Comparison between the model and the measured data points shows an RMS error of 7.2%. This new model is valid for U-shaped rods and microfibres within $30 < AR < 90$, $0.10 < \alpha < 0.80$, and $0.43 < \mathrm{Re} < 1.78$. The model was also applied to predict the vertical velocity of a microfibre with $D_C = 20$ μm and $AR = 30$ and 60 over a range of α. It was found that the vertical velocity of a U-shaped microfibre is consistently higher than that of a straight microfibre with the same diameter and aspect ratio, with a maximum difference of 28% for $AR = 30$ and 15% for $AR = 60$ over the range $0.10 < \alpha < 0.80$. This difference in vertical terminal velocity, as well as the horizontal drift observed in the settling of U-shaped rods, underscores the significant effect of this geometry on the long-range distribution of microfibres in the atmosphere.

Chapter 6

Results: Settling of S-Shaped Rods

In this chapter, the experimental results of the S-shaped rod orientation, terminal velocity, spinning rate, and tip velocity ratio are discussed. Furthermore, a theoretical analysis is performed to derive a relation for the spinning rate of an S-shaped rod. Next, a new model predicting the ratio of an S-shaped rod tip velocity to its terminal velocity is developed and compared with the experimental data. Finally, the terminal velocities of a sample microfibre with various aspect ratios and geometries have been compared utilizing the models derived in this research.

6.1 Orientation and 3D Trajectory

The observations in this research show that the S-shaped rods fall with a completely horizontal orientation upon reaching the terminal velocity, similar to the straight rods. Figure 6.1 (a) illustrates the 3D trajectory of an S-shaped rod with $D_C = 0.50$ mm, $AR = 60$, and $\alpha = 0.33$. The asymmetry in the geometry of the S-shaped rod relative to the axes passing through its centroid on the rod plane results in the rod spinning motion during settling. When viewed from the side, unlike U-shaped rods, where the heavier part is located at one end, leading to oblique orientations, S-shaped rods have their heavier part at the midpoint. Figure 6.1 (b) shows the variations in the rod orientation angle (γ in figure 3.10 (a)) with the vertical location. This plot shows that the S-shaped rod orientation angle changes linearly with

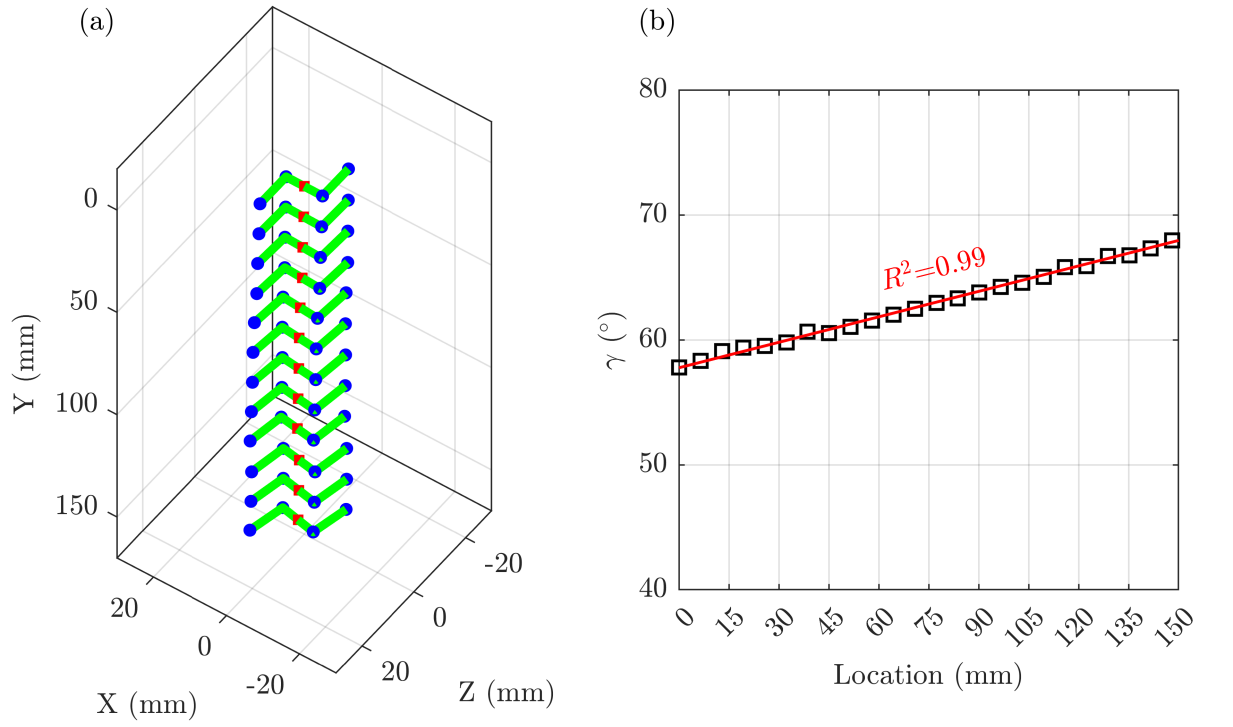

Figure 6.1: (a) 3D trajectory of an S-shaped rod with $D_C = 0.50$ mm, $AR = 60$, and $\alpha = 0.33$; (b) The orientation angle of the S-shaped rod varying with location along the rod vertical trajectory. A straight line with $R^2 = 0.99$ and a slope of 0.07 deg/mm is fitted to the data points.

location with R^2 value of 0.99. Due to the constant terminal velocity, the orientation angle of the S-shaped rod also varies linearly with time, resulting in a constant spinning rate. For the case shown in figure 6.1, the slope of the line fitted to the data points shown on the right plot is 0.07 deg/mm. Given the rod terminal velocity of 25.5 mm/s, the spinning rate is calculated as 1.78 deg/s.

6.2 Theoretical Analysis

In this section, a theoretical analysis is presented to predict how the spinning rate of an S-shaped rod changes with the rod geometric parameters, including the rod aspect ratio

(AR) and middle arm length ratio (α). This analysis focuses on calculating the total torque acting on the rod, which results in a constant spinning rate. The torque originates from the asymmetry in the pressure and shear stress distribution within the surrounding fluid and is counterbalanced by the resistive forces induced by the rod rotation. The velocity vectors of length elements for both the side and middle arms are shown in figure 6.2 (a), considering the direction of spinning and ω as the spinning rate. The force element exerted on the unit length of the rod side arm is decomposed into parallel ($\mathrm{d}F_{\parallel}$) and perpendicular ($\mathrm{d}F_{\perp}$) components as illustrated in figure 6.2 (b). The force element applied to the middle arm is parallel to the side arm and is shown as $\mathrm{d}F_2$ in this figure. As the side arm is inclined relative to the direction of the velocity, the assumptions considered by Khayat and Cox [100], Fintzi *et al.* [138] and Kharrouba *et al.* [41] are utilized to calculate $\mathrm{d}F_{\parallel}$ and $\mathrm{d}F_{\perp}$ within Stokes regime. Based on these assumptions, the equation of the fluid motion is linear with respect to the boundary conditions and the parallel and perpendicular components of the drag force can be linearly related to the flow direction. Moreover, the parallel and perpendicular components of the drag force can be scaled by the coefficients of $2\pi\mu L$ and $4\pi\mu L$ respectively, where μ is the fluid viscosity and L is the length of the cylinder [41, 100, 138]. Therefore, $\mathrm{d}F_{\perp}$, $\mathrm{d}F_{\parallel}$, and $\mathrm{d}F_2$ can be calculated from

$$\mathrm{d}F_{\parallel} = \mathrm{d}F cos\theta \approx 2\pi\mu L\omega\cos(\theta)\mathrm{d}y, \tag{6.1}$$

$$\mathrm{d}F_{\perp} = \mathrm{d}F sin\theta \approx 4\pi\mu L\omega\sin(\theta)\mathrm{d}y, \tag{6.2}$$

$$\mathrm{d}F_2 \approx 4\pi\mu\omega x\mathrm{d}x. \tag{6.3}$$

The total forces acting along the entire length of one side arm and half of the middle arm are given by:

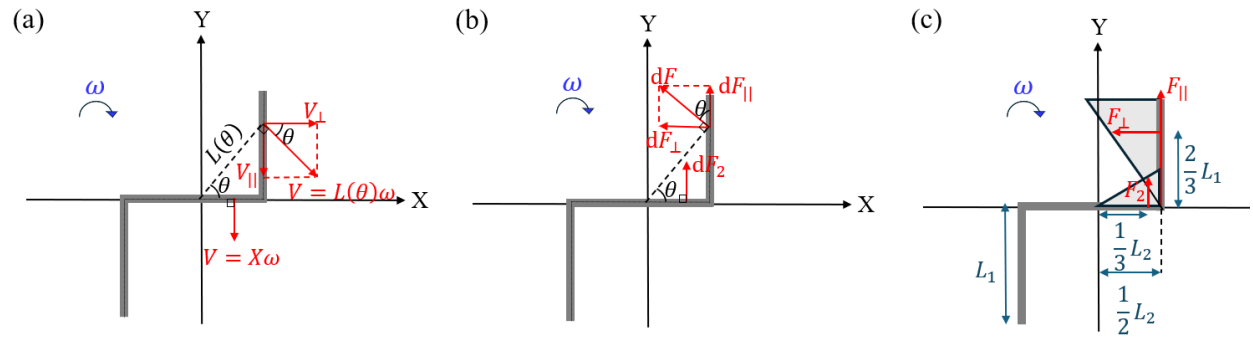

Figure 6.2: (a) Velocity vectors of two length elements, one located on the middle arm and the other on the side arm of an S-shaped rod spinning at an angular velocity ω. The vector on the side arm is decomposed into parallel ($V_{\parallel}$) and perpendicular ($V_{\perp}$) components; (b) Drag forces applied to the length elements of the side arm (dF) and middle arm (dF_2), (c) Total forces applied to the centroid of the force distributions along the side arm ($F_{\parallel}$ and $F_{\perp}$) and middle arm (F_2). The velocity vectors and force diagrams are shown for half of the rod geometry.

$$F_{\parallel} = \int_{y=0}^{y=L_1} \mathrm{d}F_{\parallel} \approx \pi\mu\omega L_1 L_2, \tag{6.4}$$

$$F_{\perp} = \int_{y=0}^{y=L_1} \mathrm{d}F_{\perp} \approx 2\pi\mu\omega L_1^2, \tag{6.5}$$

$$F_2 = \int_{x=0}^{x=L_2/2} \mathrm{d}F_2 \approx \pi\mu\omega L_2^2/2. \tag{6.6}$$

The $F_{\parallel}$, $F_{\perp}$, and F_2 are considered to be applied to the rod at the centroid of the load distributions, as shown in figure 6.2 (c). The total torque (T_{Total}) applied to the rod about the rod centroid is calculated as

$$T_{Total} = 2(F_{\parallel}L_2/2 + 2F_{\perp}L_1/3 + F_2L_2/3). \tag{6.7}$$

By substituting equations 6.4 to 6.6 into equation 6.7 and rewriting in terms of ω, we have

$$\omega = \frac{T_{Total}}{L_1L_2^2/4 + 2L_1^3/3 + L_2^3/12}. \tag{6.8}$$

L_1 and L_2 in equation 6.8 can be obtained from

$$L_1 = (1 - \alpha)L_C/2, \tag{6.9}$$

$$L_2 = \alpha L_C. \tag{6.10}$$

Equation 6.8 indicates that the spinning rate of the S-shaped rod is determined by a trade-off between the total torque (the numerator of the fraction) and rod dimensions (the denominator of the fraction). It is shown that the total torque applied to spinning particles depends on the particle Reynolds number [30, 124]. By substituting equations 6.9 and 6.10 into equation 6.8, it is demonstrated that the S-shaped rod spinning rate depends on Reynolds number, middle arm length ratio, and the total length of the rod. Equation 6.8 will be used in the following sections of this study to describe the rationale behind the variations in the spinning rate of an S-shaped rod with its aspect ratio and middle arm length ratio.

6.3 Spinning Rate and Terminal Velocity

The variations in the terminal velocity and spinning rate of the S-shaped rods with aspect ratio are shown in figure 6.3 for $D_C = 0.50,\ 0.81,$ and 1.0 mm, and $\alpha = 0.33$ in all cases. Additionally, this figure compares the terminal velocity between the S-shaped and straight rods with the same dimensions. Based on this figure, the S-shaped rod spinning rate depends on Reynolds number and aspect ratio. For $D_C = 0.50$ mm, associated with $0.25 < \mathrm{Re} < 0.44$, the rod spinning rate initially increases with aspect ratio, reaches a peak point, and then decreases with further increases in aspect ratio. However, for $D_C = 0.81$ and 1.0 mm, associated with $0.89 < \mathrm{Re} < 1.39$ and $1.44 < \mathrm{Re} < 2.14$, respectively, the spinning rate continuously decreases with the aspect ratio. The reason for these two different trends can be explained using equation 6.8. As mentioned in Section 6.2, Based on the findings of [124], we assume that the total torque (T_{Total}) depends only on the Reynolds number. For the

cases where α is constant but the aspect ratio changes, as the rod aspect ratio increases, both the numerator (T_{Total}) and the denominator in equation 6.8 increase. As a result, the ultimate change in ω results from the interplay between the mentioned numerator and denominator. For $D_C = 0.50$ mm, as the aspect ratio increases from 30 to 50, the increase in T_{Total} dominates the increase in the denominator, leading to an increase in ω. However, within $50 < AR < 120$ for $D_C = 0.50$ mm and $30 < AR < 90$ for both $D_C = 0.81$ and $D_C = 1.0$ mm, ω continuously decreases with aspect ratio, indicating the dominance of the denominator over T_{Total}. According to figure 6.3, as the S-shaped rod aspect ratio increases from 30 to 90, the terminal velocity of the rod with $D_C = 0.50$ mm increases by 14% (from 23.6 to 26.7 mm/s), while the terminal velocity of the rod with $D_C = 0.81$ and $D_C = 1.0$ mm increases by only 6% (from 51.4 to 54.6 mm/s) and 3.5% (from 67.2 to 69.6 mm/s), respectively. Given the dependence of T_{Total} on the rod terminal velocity and Reynolds number, this difference in the terminal velocity increase indicates that the numerator in equation 6.8 exerts greater influence over the denominator for the smaller diameter of $D_C = 0.5$ mm. This results in an increasing trend in ω within the range of $30 < AR < 50$ for $D_C = 0.50$ mm. Furthermore, figure 6.3 demonstrates that an S-shaped rod settles at the same rate as a straight rod with the same diameter and aspect ratio within an uncertainty of $\pm 2.9\%$. This suggests that, within the measurement uncertainty, the terminal velocity of an S-shaped rod is likely unaffected by the spinning motion and is determined solely by the balance between gravity and hydrodynamic forces within the ranges considered in this study. Therefore, the terminal velocity of an S-shaped rod within $30 < AR < 120$ and $\mathrm{Re} < 2.14$ can be predicted using the model developed in Section 4.4

Figure 6.4 illustrates how an S-shaped rod terminal velocity and spinning rate change with the rod middle arm length ratio (α). According to this figure, the terminal velocity of the S-shaped rods only depends on the rod diameter and aspect ratio and is independent of α. Moreover, the rod spinning rate depends on α besides the Reynolds number and aspect ratio. For all diameters of 0.50, 0.81, and 1.0 mm, associated with $\mathrm{Re} = 0.34, 1.19,$ and 1.88,

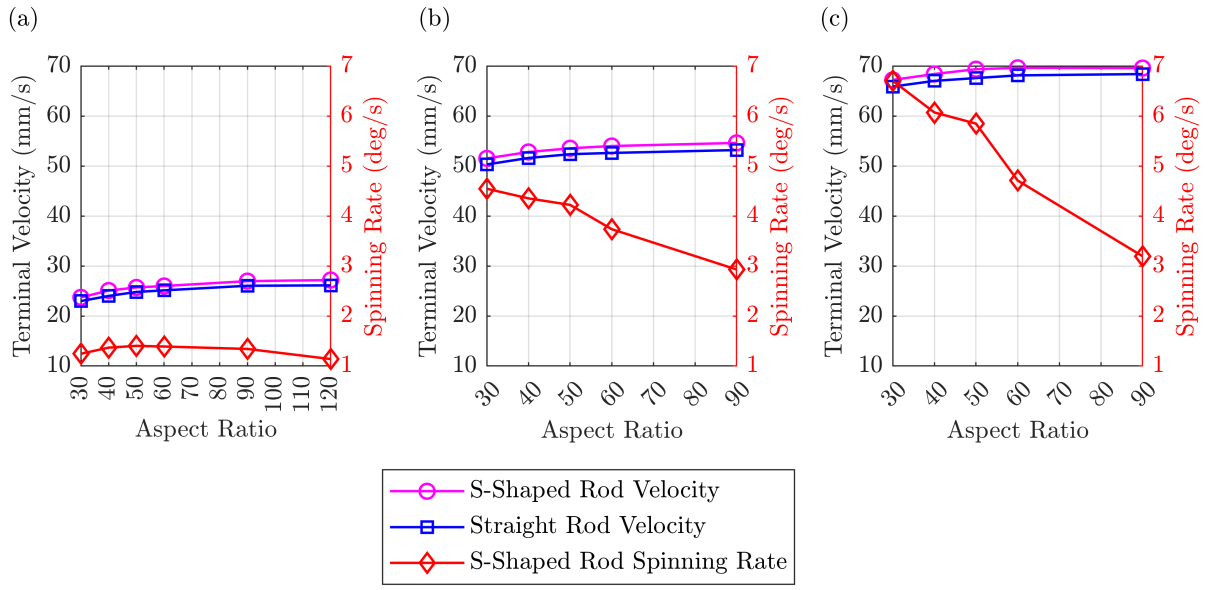

Figure 6.3: Variations of S-shaped rod terminal velocity and spinning rate with aspect ratio for $\alpha = 0.33$ and (a) $D_C = 0.50$ mm ($0.25 < \mathrm{Re} < 0.44$), (b) $D_C = 0.81$ mm ($0.89 < \mathrm{Re} < 1.39$), (c) $D_C = 1.0$ mm ($1.44 < \mathrm{Re} < 2.14$). The mentioned ranges of Reynolds numbers are calculated based on D_{eq}.

respectively, the spinning rate increases with α, reaches a peak at $\alpha = 0.5$, and then decreases with further increase in α. It is observed that this trend holds true for all rod diameters and aspect ratios. The reason for this trend can be explained based on equation 6.8. In the cases where the rod aspect ratio is constant and only the middle arm length ratio changes, as the terminal velocity and Reynolds number do not change with α, T_{Total} is assumed to remain constant over the whole range of α, whereas the denominator in equation 6.8 changes. By replacing L_1 and L_2 in the denominator of equation 6.8 with equations 6.9 and 6.10, the denominator becomes a function of L_C and α. Figure 6.5 shows the variation of ω with α as determined by equation 6.8. In this figure, κ is the result of the multiplication of all constants in the derivation of this equation and can be approximated from

$$\kappa = \frac{\pi \mu L_C^3}{T_{Total}}. \tag{6.11}$$

The values on the y-axis in figure 6.5 are dimensionless, and κ is measured in seconds. As

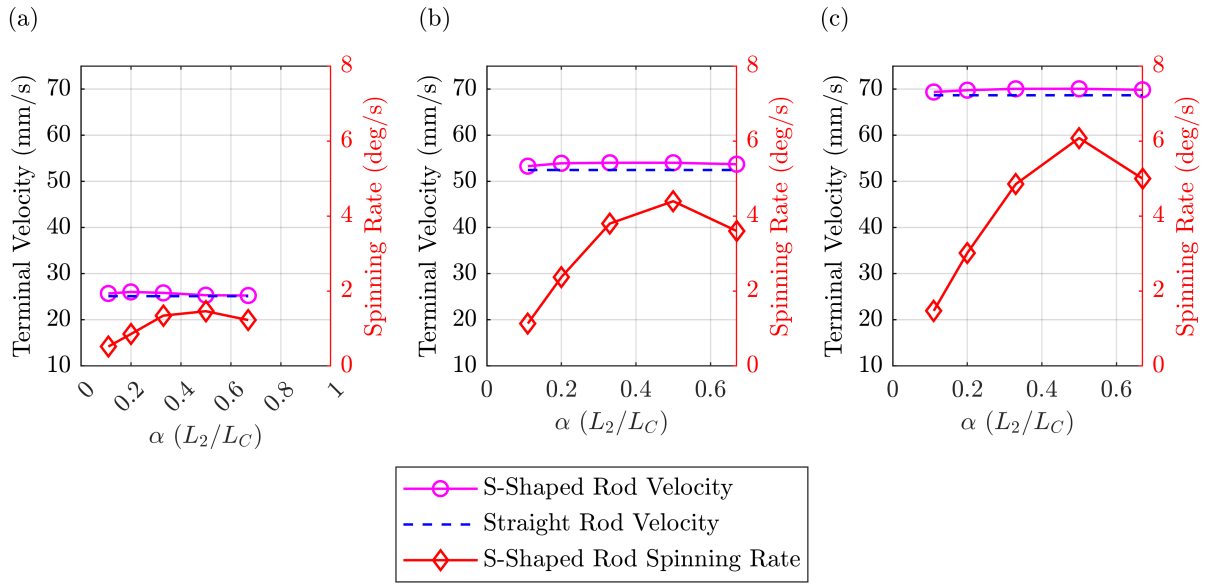

Figure 6.4: Variations of S-shaped rod terminal velocity and spinning rate with middle arm length ratio for $AR = 60$ and (a) $D_C = 0.50$ m (Re $= 0.34$), (b) $D_C = 0.81$ m (Re $= 1.19$), (c) $D_C = 1.0$ m (Re $= 1.88$). Reynolds numbers are calculated based on D_{eq}.

can be seen from this figure, the maximum spinning rate occurs at $\alpha = 0.42$, which is 16% smaller than our experimental results ($\alpha = 0.5$). Given the experimental resolution within $0.33 < \alpha < 0.67$ based on table 3.5, the adjacent measured data points are 0.5 ± 0.17, making a local maximum around $\alpha = 0.5$ reasonable in comparison with the theoretical analysis.

6.4 Tip Velocity Ratio

The ratio of a spinning object tip velocity to its settling velocity can influence the flow patterns around the object, potentially generating a lift force, modifying the wake structure, and affecting vortex shedding and stability at higher Reynolds numbers [124, 141, 142]. These effects can impact the settling behavior and trajectory of the object, underscoring the importance of studying the S-shaped rod tip velocity ratio in this research. The variations in the S-shaped rod tip velocity ratio (V_T/V_S), calculated from equation 6.12, with aspect ratio is shown in figure 6.6 for $\alpha = 0.33$.

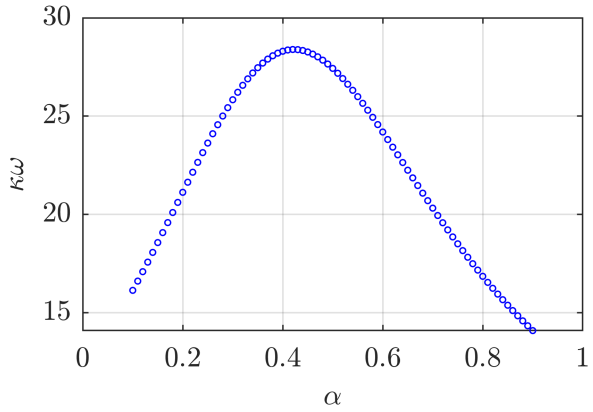

Figure 6.5: Variations of S-shaped rod spinning rate (ω) with middle arm length ratio (α) based on equation 6.8. κ is defined by equation 6.11.

$$V_T/V_S = \omega L/V_S. \tag{6.12}$$

In equation 6.12, V_T is the rod tip velocity, V_S is the rod terminal velocity, ω is the spinning rate, and L is the distance between the rod centroid and its tip point. As observed in figure 6.6, the tip velocity ratio consistently increases with aspect ratio for $D_C = 0.50$ and 0.81 mm at all aspect ratios. However, for $D_C = 1.0$ mm, the tip velocity ratio increases with aspect ratio within $30 < AR < 50$ and reaches a plateau within $50 < AR < 90$. As a result, for lower Reynolds numbers (Re < 1.75), the S-shaped rod tip velocity ratio is more influenced by the length of the arm (L) than the spinning rate or settling velocity, resulting in a continuous increase with aspect ratio. However, for higher Reynolds numbers (Re > 1.75), the decrease in the spinning rate becomes significant and causes the tip velocity ratio to remain constant as the aspect ratio increases. The variations of the tip velocity ratio with middle arm length ratio for $AR = 60$ are illustrated in figure 6.7. This figure shows that the tip velocity ratio peaks at $\alpha = 0.5$ for all rod diameters, indicating the dominance of spinning rate (ω) over arm length (L) in equation 6.12. Additionally, as the rod diameter and consequently Reynolds increases, the tip velocity ratio increases for a given α and AR.

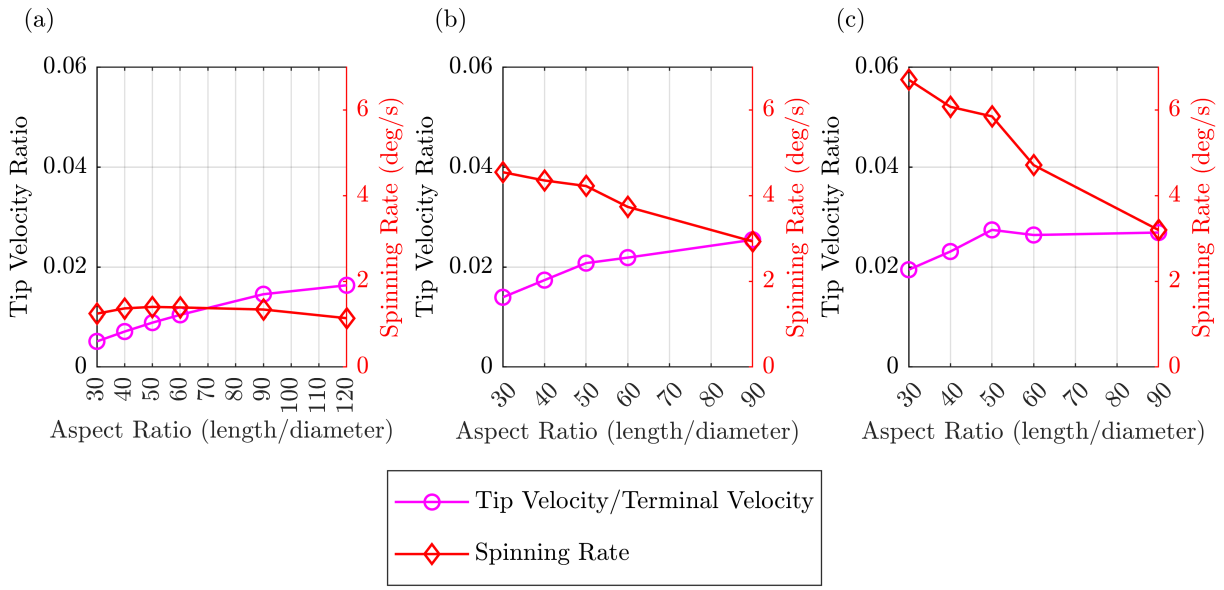

Figure 6.6: Variations of S-shaped rod tip velocity ratio and spinning rate with aspect ratio for $\alpha = 0.33$ and (a) $D_C = 0.50$ m, (b) $D_C = 0.81$ m, (c) $D_C = 1.0$ m.

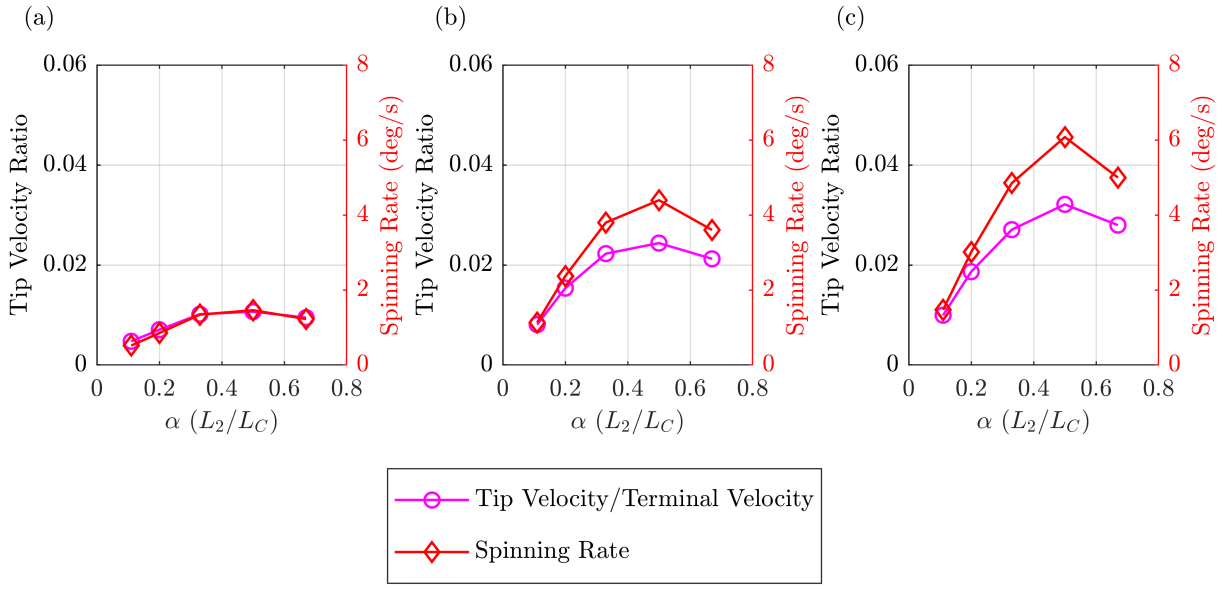

Figure 6.7: Variation of S-shaped rod tip velocity ratio and spinning rate with middle arm length ratio for $AR = 60$ and (a) $D_C = 0.50$ m, (b) $D_C = 0.81$ m, (c) $D_C = 1.0$ m.

6.5 Model Development

A new model to predict the ratio of the S-shaped rod tip velocity to its terminal velocity is developed based on the experimental results in this study. Our new model builds upon the model outlined by Pierson *et al.* [127], which is used to predict the tip velocity ratio of a falling straight rod as its orientation changes on a vertical plane during settling at low Reynolds numbers. In the model by Pierson *et al.* [127], the ratio of the straight rod tip velocity exhibits a power-law relationship with both the Reynolds number and the aspect ratio. In addition to these parameters, as shown in figure 6.6, the S-shaped rod tip velocity ratio depends on the middle arm length ratio and peaks at a certain value of this ratio, as depicted in figure 6.7. Hence, a second-order polynomial in terms of α has been incorporated into our model to account for the effects of the middle arm length ratio. The general form of our new model is

$$\frac{V_T}{V_S} = \frac{\omega L}{V_S} = \frac{\pi}{180}\frac{Re^a}{AR^b}(c\alpha^2 + d\alpha + e), \tag{6.13}$$

where V_T, V_S, and L are the S-shaped rod tip velocity, terminal velocity, and the distance between the rod centroid and one of its endpoints, respectively. This correlation is fitted to our experimental results, and the coefficients of a, b, c, d, and e are determined as 0.56, -0.22, -2.17, 2.20, and -0.045, respectively. This model is employed to predict the tip velocity ratio of the S-shaped rods used in this study, and the calculated results are compared with the experimental results in figure 6.8. The RMS error of the model is calculated as 8.6%. This model is valid within the ranges investigated in this study ($30 < AR < 120$, $0.11 < \alpha < 0.67$, and $0.25 < \mathrm{Re} < 2.14$)

As an example, the model proposed in this study is utilized to estimate the tip velocity ratio of a typical microfibre with a diameter of 20 μm at various aspect ratios and middle arm length ratios [12]. Figure 6.9 (a) shows the variations in the tip velocity ratio of the microfibre with aspect ratios ranging between 30 and 120, assuming $\alpha = 0.33$. The Reynolds

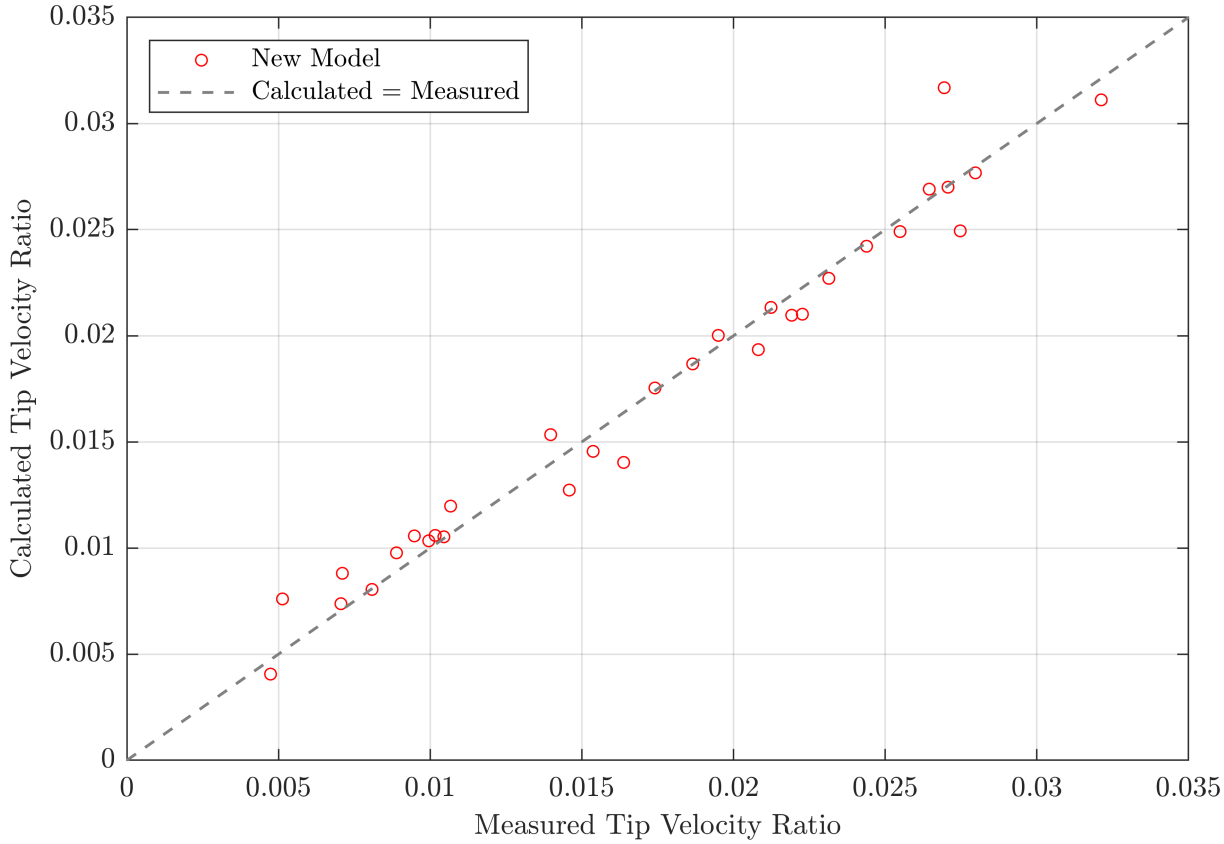

Figure 6.8: The ratio of S-shaped rod tip velocity to terminal velocity calculated from the new model proposed in this study versus the experimental results. The dashed line equates the measured and calculated data.

number associated with the settling of this microfibre is calculated via an iterative method utilizing the model proposed for straight rods in our recent study [50]. As seen in figure 6.9 (a), the tip velocity ratio of the microfibre continuously increases with aspect ratio, which is consistent with our experimental observations illustrated in figure 6.6. The Reynolds number in this example varies from 0.33 to 0.58. As discussed in Section 6.4, within this range of Reynolds number, the changes in the length of the S-shaped fibre arm are dominant over the changes in spinning rate and terminal velocity, leading to a consistent increase in the tip velocity ratio with aspect ratio. However, as observed in figure 6.9 (a), the higher the aspect ratio, the smaller the variations in the tip velocity ratio. For instance, as the microfibre

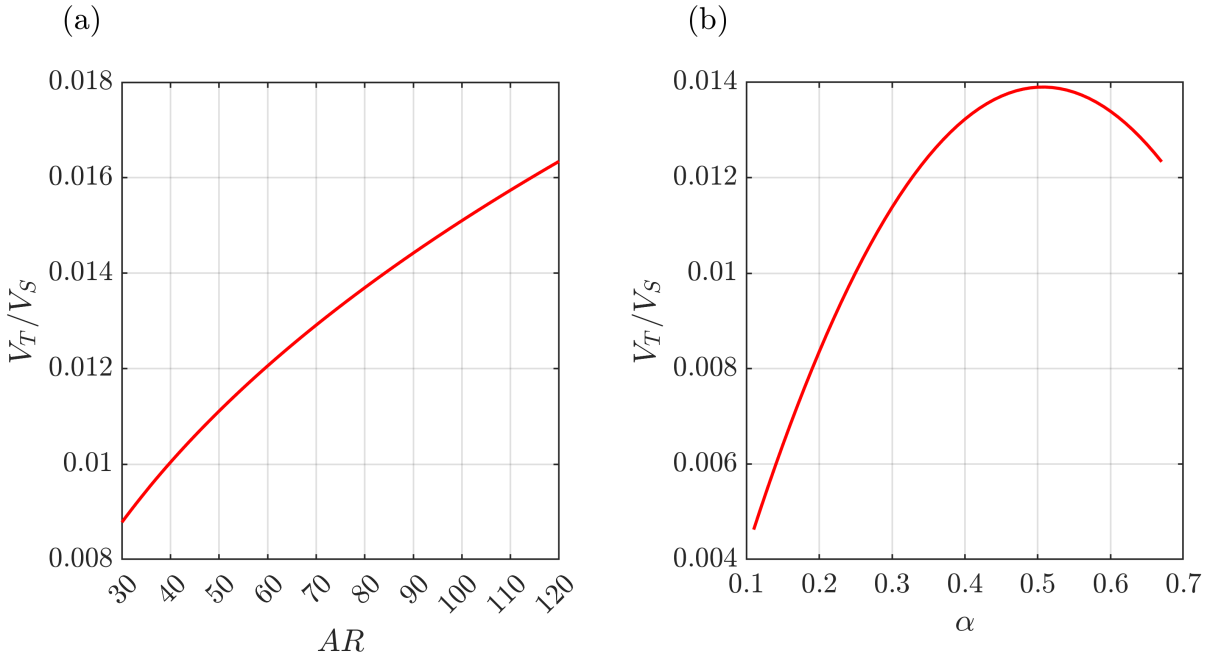

Figure 6.9: The tip velocity ratio of an S-shaped microfibre at (a) $\alpha = 0.33$ with varying AR and (b) $AR = 60$ with varying α, calculated using the new model proposed in this study.

aspect ratio increases from 30 to 60, the tip velocity ratio increases by 33% (from 0.009 to 0.012), while it increases by only 17% (from 0.012 to 0.014) as the aspect ratio increases from 60 to 90. Figure 6.9 (b) illustrates how the microfibre tip velocity ratio changes with the middle arm length ratio, assuming $AR = 60$. As discussed in Section 6.4, in this case, the microfibre tip velocity ratio follows the same trend as the spinning rate, meaning that it initially increases with α, peaks at $\alpha = 0.50$, and decreases with further increase in α. In this example, the microfibre tip velocity ratio reaches a maximum value of 0.014 at $\alpha = 0.50$.

6.6 Comparison of Fibre Velocity for Various Geometries

This section compares the estimated vertical terminal velocity of sample microfibres in quiescent air for all geometries studied in this research, including straight, curved, and bent shapes (V-, U-, and S-shapes), across a range of aspect ratios from 20 to 90. Two fibres made of polyacrylonitrile, with a density of 1184 kg/m^3 [12] and diameters of 20 μm and 30 μm,

were considered. The models developed for straight, curved, and V-shaped rods, as discussed in Section 4.4, along with the model developed for U-shaped rods, as presented in Section 5.4, were utilized to estimate the velocities of the fibres. The two microfibre diameters were chosen to ensure that the range of Reynolds numbers applicable to the models developed in this research is covered. The fibre with $D_C = 20$ μm spans a Reynolds number range from 0.27 to 0.70, while the fibre with $D_C = 30$ μm covers a range from 0.79 to 1.90. The results for $D_C = 20$ μm and $D_C = 30$ μm are shown in figure 6.10 (a) and (b), respectively. This figure indicates that the V-shaped microfibre with $\beta = 0.38$, corresponding to a bend angle (α_0) of 45°, exhibits the highest terminal velocity compared to other geometries for both fibre diameters. The terminal velocities of V-shaped fibres with $45° < \alpha_0 < 180°$ fall within the region bounded by the straight fibre curve and the V-shaped fibre curve with $\beta = 0.38$. Similarly, the region between the curved fibre with $\beta = 0.64$, associated with a semicircular shape, and the straight fibre encompasses the velocity range for curved fibres. For the U-shaped fibres, the variation in fibre velocity with aspect ratio for two values of α, corresponding to the minimum and maximum mean velocities over the range $20 < AR < 90$, is shown. These two values of α were selected from the range of $0.2 < \alpha < 0.8$. Based on this figure, the maximum mean velocity over the range $20 < AR < 90$ occurs at $\alpha = 0.4$ for $D_C = 20$ μm and at $\alpha = 0.55$ for $D_C = 30$ μm. The minimum mean velocity across the mentioned range of AR is achieved at $\alpha = 0.8$ and $\alpha = 0.2$ for $D_C = 20$ μm and $D_C = 30$ μm, respectively. The reason the fibres exhibit their minimum vertical velocities at the lower and upper bounds of the α range is the more horizontally aligned orientation of the side arms at the lower bound and the shorter side arms at the upper bound. However, at a medium value of α, the oblique orientation, along with a moderate side arm length, leads to the maximum velocity. This trend is also consistent with the observations described in Section 5.2. Likewise, due to the interplay between the opposing effects of side arm length and inclination angle on terminal velocity, the U-shaped fibres with $D_C = 20$ μm and $\alpha = 0.40$ peak at $AR = 45$, while the fibre with $D_C = 30$ μm and $\alpha = 0.55$ peaks at $AR = 26$. Additionally, the fibres

with $\alpha = 0.8$ and 0.2 do not exhibit any significant variations with aspect ratio. The range of U-shaped fibre vertical velocities falls between those of the straight fibres and the V-shaped fibres with $\beta = 0.38$ for both diameters.

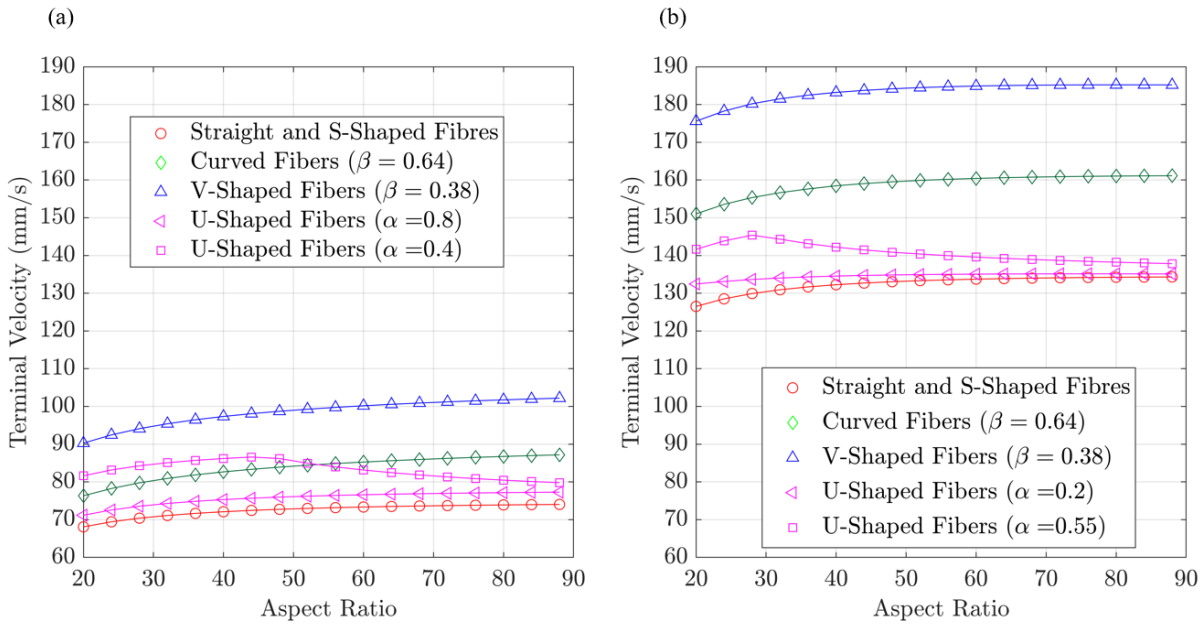

Figure 6.10: Comparison of the terminal velocity of a microfibre with a diameter of (a) 20 μm and (b) 30 μm and a density of 1184 kg/m^3 across various geometries and aspect ratios. Reynolds number ranges from 0.27 to 0.70 for panel (a) and from 0.79 to 1.90 for panel (b).

It should be noted that the aerodynamic models developed in this research are applicable to the transport of microfibres when atmospheric turbulence is neglected. In realistic situations, this assumption holds primarily within a stably stratified atmospheric boundary layer. Under such conditions, typically occurring at night under clear skies and light winds, there is minimal surface heating, and little to no mixing occurs between different layers of air above the ground. Turbulence is significantly weaker compared to daytime conditions, and the atmospheric boundary layer depth may be less than 100 meters [143]. Nevertheless, the results concerning microfibre terminal velocity in a quiescent fluid provide valuable insights into the impact of fibre morphology on long-range transport and can be utilized as a foundation for future studies investigating the influence of turbulence on fibre settling behavior.

6.7 Chapter Summary

In this chapter, the settling behavior of S-shaped cylindrical rods was experimentally investigated to replicate the range of Reynolds number associated with the atmospheric settling of microplastic fibres. The S-shaped rods were observed to spin at a constant rate on a horizontal plane with a zero inclination angle while settling. The results show that the terminal velocity of the S-shaped rods is the same as that of the straight rods with the same diameter and aspect ratio. Furthermore, The spinning rate of the S-shaped rods generally decreases with the rod aspect ratio and peaks at the middle arm length ratio of 0.5 and 0.42 based on our experimental results and theoretical analysis, respectively. The variations in the spinning rate of an S-shaped rod can be explained by the trade-off between the total torque applied to the rod due to the asymmetry in its geometry and the rod length. Based on the experimental results, a new model was developed to estimate the ratio of tip velocity to terminal velocity for the S-shaped rods with an RMS error of 8.6%. This model was applied to predict the tip velocity ratio of a microfibre with various aspect ratios and middle arm length ratios. The microfibre tip velocity ratio consistently increases with the aspect ratio, with smaller variations at higher aspect ratios. Furthermore, it showcases an initial increase with the middle arm length ratio, peaking at the middle arm length ratio of 0.50, followed by a decrease with a further increase in the middle arm length ratio. This model is valid within a range of Reynolds numbers between 0.25 and 2.14, fibre aspect ratio between 30 and 120, and middle arm length ratio between 0.11 and 0.67. The terminal velocities of microfibres with various geometries, estimated using the models developed in this research, were studied and compared across a range of fibre aspect ratios between 20 and 90. It was shown that V-shaped fibres with a bend angle of 45 degrees settle faster than other geometries, while the straight and S-shaped fibres have the smallest terminal velocities. The curved and U-shaped fibres settle within the range of terminal velocities between straight fibres and V-shaped fibres with a bend angle of 45 degrees. The U-shaped fibres either exhibit minimal changes

in terminal velocity with aspect ratio or peak at a certain aspect ratio, depending on the middle arm length ratio.

Chapter 7

Conclusions and Future Recommendations

7.1 Conclusions

In this research, the settling behavior of cylindrical rods with various geometries was experimentally studied at low Reynolds numbers. These experiments were motivated by the atmospheric settling of plastic microfibres, the most abundant type of microplastics, whose borderless dispersion across the globe has raised environmental concerns. Current models to predict settling velocities of microfibres in simulations of atmospheric transport and deposition often simplify their geometries, representing them as volume-equivalent spheres or straight cylinders. However, a closer examination of realistic microfibre samples reveals that they often adopt more complex geometries, incorporating elements of V-, U-, and S-shapes, as well as curves. To facilitate this study, millimeter-sized metal rods are used and their settling is tracked in a viscous mixture of glycerin and water. This scenario is used to replicate the Reynolds numbers expected for the settling of plastic microfibres in air ($\mathrm{Re} < 7$). The advantage of this method is that it facilitates tracking due to the large size of the rods and minimal uncertainties related to their dimensions. The investigation of a wide range of rod aspect ratios, spanning from short to long cylinders, as well as V-, U-, and S-shaped morphologies, constitutes the key novelties of the present research.

In the design of the experiments, the material and dimensions of the cylindrical rods, as well as the properties of the fluid, were selected such that the desired low Reynolds numbers could be replicated. Aluminum and brass rods with diameters ranging from 0.50 to 1.00 mm and aspect ratios between 10 and 120 were used in the experiments. The chosen aspect ratio range corresponds to those reported for microfibres collected from atmospheric depositions in the literature. A water-glycerin mixture with a glycerin weight ratio of 90% at a temperature of 21°C was selected as the working fluid. The settling behavior of the rods in the quiescent water-glycerin mixture was captured using a custom-designed camera system Additionally, a bottom-view camera was employed to provide a robust measurement of the potential spinning motions of the rods. The captured images were processed to identify the pixel locations of key geometric points on the rods. These pixel locations were then converted into real-world coordinates using a stereo calibration algorithm co-developed in part for this research.

It was demonstrated that V-shaped rods consistently settle faster than straight rods with the same diameters and aspect ratios due to the inclination of their arms and reduced projected area. However, existing models for predicting the terminal velocity of inclined cylinders fail to accurately estimate the velocities of V-shaped rods within the Reynolds number range studied in this research. When comparing V-shaped and curved rods, the terminal velocity difference is minor under identical conditions of diameter, aspect ratio, and projected area, with V-shaped rods settling slightly faster. This velocity difference increases with the curvature index, reaching a maximum of 4% for a semi-circle shape. The drag coefficient of V-shaped rods initially decreases as they transition from a straight to a bend angle of 90° due to the greater impact of terminal velocity changes over the projected area variations. Beyond 90°, however, further bending increases the drag coefficient as projected area changes became more significant. A new model was developed to predict the drag coefficient and terminal velocity of V-shaped, curved, and straight rods within the ranges of Reynolds number from 0.03 to 5, aspects ratio from 3 to 120, and projected length-to-total length ratio from 0.64 to 1. This model achieves an RMS error of 7.1% when compared with

the experimental data points. Notably, it expands the valid range for the curvature index of curved rods compared to our previous model developed for straight and curved rods [50]. The model was further applied to assess the vertical terminal velocity and horizontal travel distance of a typical atmospheric microfibre with a V-shaped geometry relative to a straight rod. It was shown that increasing the bend angle or projected area of a V-shaped fibre reduces its terminal velocity while increasing its horizontal travel distance, eventually approaching the behavior of a straight fibre with the same diameter and aspect ratio. For instance, bending a straight fibre into a V-shaped geometry with a bend angle of 45° decreases its horizontal travel distance by 27%, which significantly influences predictions of atmospheric deposition.

The results of U-shaped rods show that the orientation of U-shaped rods, whether vertical or oblique, depends on the Reynolds number and the middle arm length ratio, transitioning from vertical to oblique as the Reynolds number exceeds a critical value or the middle arm length ratio falls below a threshold. The vertical velocity of the U-shaped rods results from the interplay between the length and orientation of the side arms, either peaking at specific aspect and middle arm length ratios or remaining constant depending on the Reynolds number and inertial effects. For a given diameter, stronger inertial effects at larger aspect ratios shift the peak vertical velocity to higher middle arm length ratios. The horizontal velocity ratio of U-shaped rods is primarily influenced by the inclination angle, decreasing significantly as the rod orientation approaches vertical. This ratio generally increases with the aspect ratio due to consistent decreases in the inclination angle, peaking at 0.2 for middle arm length ratios between 0.2 and 0.3. Higher inertial effects at larger diameters and aspect ratios lead to more gradual changes in both inclination angle and horizontal velocity ratio. The drag coefficient of U-shaped rods, calculated based on their projected length, is higher than that of straight rods of the same dimensions in vertical orientations due to the greater influence of projected area compared to vertical velocity. Conversely, for oblique orientations, straight rods exhibit higher drag coefficients due to the dominance of vertical velocity over projected area. The drag coefficient of U-shaped rods is positively correlated with the middle

arm length ratio in oblique orientations and negatively correlated in vertical orientations, reflecting a trade-off between projected area and the square of vertical velocity. New models were developed to predict the inclination angle and drag coefficient of U-shaped rods with an RMS error of 7.2%. These models are valid for U-shaped rods and microfibres within the ranges of aspect ratio from 30 to 90, middle arm length ratio from 0.10 to 0.80, and Reynolds number from 0.43 to 1.78. The models were also applied to predict the vertical velocity of U-shaped microfibres with a diameter of 20 μm and aspect ratios of 30 and 60 over a range of middle arm length ratios. The findings show that U-shaped microfibres consistently have higher vertical velocities than straight microfibres with the same diameter and aspect ratio, with maximum differences of 28% and 15% for aspect ratios of 30 and 60, respectively. These differences in vertical velocity, along with the horizontal drift observed, highlight the significant impact of U-shaped geometries on the long-range atmospheric distribution of microfibres.

S-shaped rods were observed to spin at a constant rate on a horizontal plane with a zero inclination angle while settling. Their terminal velocity was found to be identical to that of straight rods with the same diameter and aspect ratio. The spinning rate of the S-shaped rods generally decreases with the rod aspect ratio. Moreover, it peaks at middle arm length ratios of 0.5 and 0.42, respectively, based on the experimental and theoretical analysis performed in this research. These variations in the spinning rate are attributed to a trade-off between the total torque generated by the asymmetry in the rod geometry and the rod length. Based on the experimental results, a new model was developed to estimate the ratio of tip velocity to terminal velocity for S-shaped rods, achieving an RMS error of 8.6%. This model was further applied to predict the tip velocity ratio of microfibres with various aspect ratios and middle arm length ratios, showing that the tip velocity ratio increases consistently with the aspect ratio and initially increases with the middle arm length ratio, peaking at 0.50 before decreasing at higher values. The model is valid within a Reynolds number range of 0.25 to 2.14, fibre aspect ratios between 30 and 120, and middle arm length ratios between 0.11 and

0.67.

The impact of fibre morphology on their terminal velocity was investigated using the models developed in this research for various rod geometries. It was shown that V-shaped fibres with a bend angle of 45 degrees settle faster than other geometries, while the straight and S-shaped fibres exhibit the smallest velocities. The velocity range covered by the U-shaped and curved fibres is larger than that of the straight fibres and smaller than that of the V-shaped fibres with a bend angle of 45 degrees. While the fibre terminal velocity consistently increases with aspect ratio for straight, S-shaped, curved, and V-shaped morphologies, it may peak at a particular aspect ratio or remain almost constant at different values of aspect ratio for U-shaped fibres, depending on the fibre middle arm length ratio. The results of this study underscore the significance that fibre morphology can have on the long-range distribution of microfibres in the atmosphere. Furthermore, the models developed in this study can be applied in atmospheric simulations to predict the terminal velocity of microfibres with the morphologies examined in this research, and consequently, to determine their trajectories and fate in the atmosphere.

7.2 Future Recommendations

This research provides valuable insights into the settling behavior of various geometries observed in microfibre samples collected from atmospheric depositions. Using the models developed in this study, the terminal velocities of microfibres with the studied geometries can be estimated, enabling more accurate predictions of their trajectories in atmospheric simulations. However, this study has certain limitations that can be addressed in future research in this field.

Turbulence in the atmosphere plays a pivotal role in the transport of microfibres. The effect of turbulence on the settling of rods can be investigated by generating turbulence within a chamber with zero mean velocity. Depending on the effective turbulence mechanism, the settling of rods with various geometries may either be enhanced or retarded. This impact

can be further explored in future studies using random jet array systems, such as the one already designed and built as part of my research activity at York University. This system has already been designed and built at York University and can be utilized in upcoming research.

The behavior of rods in a quiescent fluid during the transition period can provide deeper insights into their settling dynamics, as it significantly influences their terminal velocity and settling orientations. During this period, the rod has not yet reached its terminal velocity and experiences variations in velocity and orientation due to the effects of inertial torque. This transition phase has not been extensively studied in previous research, particularly for complex geometries such as U-shaped and S-shaped rods, making it a promising topic for future investigations.

Additionally, a different range of Reynolds numbers can be replicated in experiments by altering the material of the rods or the fluid. This approach enables the study of a lower range of Reynolds numbers corresponding to the settling of microfibres in aquatic environments. As the density of plastic microfibres is very close to that of water, they settle at very small Reynolds numbers in aquatic media, which offers a new direction for future research. The effects of fibre flexibility on its settling can also be studied by dropping realistic fibres in an air or water chamber, depending on the Reynolds number range of interest.

References

[1] A. A. Horton and S. J. Dixon, "Microplastics: An introduction to environmental transport processes," *Wiley Interdisciplinary Reviews: Water*, vol. 5, no. 2, p. e1268, 2018.

[2] J. M. Sipe, N. Bossa, W. Berger, N. von Windheim, K. Gall, and M. R. Wiesner, "From bottle to microplastics: Can we estimate how our plastic products are breaking down?," *Science of the Total Environment*, vol. 814, p. 152460, 2022.

[3] Y. Zhang, S. Kang, S. Allen, D. Allen, T. Gao, and M. Sillanpää, "Atmospheric microplastics: A review on current status and perspectives," *Earth-Science Reviews*, vol. 203, p. 103118, 2020.

[4] O. S. Alimi, D. Claveau-Mallet, M. Lapointe, T. Biu, L. Liu, L. M. Hernandez, S. Bayen, and N. Tufenkji, "Effects of weathering on the properties and fate of secondary microplastics from a polystyrene single-use cup," *Journal of Hazardous Materials*, vol. 459, p. 131855, 2023.

[5] B. Pinlova and B. Nowack, "From cracks to secondary microplastics-surface characterization of polyethylene terephthalate (PET) during weathering," *Chemosphere*, vol. 352, p. 141305, 2024.

[6] A. Zeb, W. Liu, N. Ali, R. Shi, Q. Wang, J. Wang, J. Li, C. Yin, J. Liu, M. Yu, *et al.*, "Microplastic pollution in terrestrial ecosystems: Global implications and sustainable solutions," *Journal of Hazardous Materials*, vol. 461, p. 132636, 2024.

[7] X. Dong, X. Liu, Q. Hou, and Z. Wang, "From natural environment to animal tissues: A review of microplastics (nanoplastics) translocation and hazards studies," *Science of the Total Environment*, vol. 855, p. 158686, 2023.

[8] G. Lamichhane, A. Acharya, R. Marahatha, B. Modi, R. Paudel, A. Adhikari, B. Raut, S. Aryal, and N. Parajuli, "Microplastics in environment: global concern, challenges, and

controlling measures," *International Journal of Environmental Science and Technology*, vol. 20, no. 4, pp. 4673–4694, 2023.

[9] S. Bucci, C. Richon, and L. Bakels, "Exploring the transport path of oceanic microplastics in the atmosphere," *Environmental Science & Technology*, vol. 58, no. 32, pp. 14338–14347, 2024.

[10] R. Arya, J. Rathore, A. K. Mishra, and A. Mondal, "Microplastics in the atmosphere: Identification, sources and transport pathways," in *Remediation of Plastic and Microplastic Waste*, pp. 71–88, CRC Press, 2024.

[11] S. Fox, H. Stefánsson, E. J. Ásbjörnsson, M. Peternell, P. Wanner, E. Sturkell, M. Konrad-Schmolke, and E. Zlotskiy, "Physical characteristics of microplastic particles and potential for global atmospheric transport: A meta-analysis," *Environmental Pollution*, p. 122938, 2023.

[12] S. L. Wright, J. Ulke, A. Font, K. L. A. Chan, and F. J. Kelly, "Atmospheric microplastic deposition in an urban environment and an evaluation of transport," *Environment International*, vol. 136, p. 105411, 2020.

[13] Y. Y. Hee, N. M. Hanif, K. Weston, M. T. Latif, S. Suratman, M. U. Rusli, and A. G. Mayes, "Atmospheric microplastic transport and deposition to urban and pristine tropical locations in Southeast Asia," *Science of the Total Environment*, vol. 902, p. 166153, 2023.

[14] M. Klein and E. K. Fischer, "Microplastic abundance in atmospheric deposition within the Metropolitan area of Hamburg, Germany," *Science of the Total Environment*, vol. 685, pp. 96–103, 2019.

[15] M. Bergmann, S. Mützel, S. Primpke, M. B. Tekman, J. Trachsel, and G. Gerdts, "White and wonderful? Microplastics prevail in snow from the Alps to the Arctic," *Science Advances*, vol. 5, no. 8, p. eaax1157, 2019.

[16] N. Evangeliou, H. Grythe, Z. Klimont, C. Heyes, S. Eckhardt, S. Lopez-Aparicio, and A. Stohl, "Atmospheric transport is a major pathway of microplastics to remote regions," *Nature Communications*, vol. 11, no. 1, pp. 1–11, 2020.

[17] Y. Zhang, T. Gao, S. Kang, D. Allen, Z. Wang, X. Luo, L. Yang, J. Chen, Z. Hu, P. Chen, *et al.*, "Cryosphere as a temporal sink and source of microplastics in the Arctic region," *Geoscience Frontiers*, vol. 14, no. 4, p. 101566, 2023.

[18] S. O'Brien, C. Rauert, F. Ribeiro, E. D. Okoffo, S. D. Burrows, J. W. O'Brien, X. Wang, S. L. Wright, and K. V. Thomas, "There's something in the air: a review of sources, prevalence and behaviour of microplastics in the atmosphere," *Science of the Total Environment*, vol. 874, p. 162193, 2023.

[19] C. Wang, M. Guo, B. Yan, J. Wei, F. Liu, Q. Li, and Y. Bo, "Characteristics of microplastics in the atmosphere of Anyang City," *Environmental Monitoring and Assessment*, vol. 196, no. 4, p. 350, 2024.

[20] I. E. Napper, F. N. F. Parker-Jurd, S. L. Wright, and R. C. Thompson, "Examining the release of synthetic microfibres to the environment via two major pathways: Atmospheric deposition and treated wastewater effluent," *Science of the Total Environment*, vol. 857, p. 159317, Jan. 2023.

[21] R. Dris, J. Gasperi, M. Saad, C. Mirande, and B. Tassin, "Synthetic fibers in atmospheric fallout: a source of microplastics in the environment?," *Marine Pollution Bulletin*, vol. 104, no. 1-2, pp. 290–293, 2016.

[22] S. Allen, D. Allen, F. Baladima, V. Phoenix, J. Thomas, G. Le Roux, and J. Sonke, "Evidence of free tropospheric and long-range transport of microplastic at Pic du Midi Observatory," *Nature Communications*, vol. 12, no. 1, p. 7242, 2021.

[23] Z. Liu, T. Liang, and X. Liu, "Characteristics, distribution patterns and sources of atmospheric microplastics in the Bohai and Yellow Seas, China," *Science of the Total Environment*, vol. 926, p. 171906, 2024.

[24] A. Martynova, L. Genchi, S. P. Laptenok, M. Cusack, G. L. Stenchikov, C. Liberale, and C. M. Duarte, "Atmospheric microfibrous deposition over the Eastern Red Sea coast," *Science of the Total Environment*, vol. 907, p. 167902, 2024.

[25] O. Mbachu, G. Jenkins, C. Pratt, and P. Kaparaju, "A new contaminant superhighway? A review of sources, measurement techniques and fate of atmospheric microplastics," *Water, Air, & Soil Pollution*, vol. 231, pp. 1–27, 2020.

[26] N. Evangeliou, O. Tichy, S. Eckhardt, C. G. Zwaaftink, and J. Brahney, "Sources and fate of atmospheric microplastics revealed from inverse and dispersion modelling: From global emissions to deposition," *Journal of Hazardous Materials*, vol. 432, p. 128585, 2022.

[27] X. Long, T.-M. Fu, X. Yang, Y. Tang, Y. Zheng, L. Zhu, H. Shen, J. Ye, C. Wang, T. Wang, *et al.*, "Efficient atmospheric transport of microplastics over Asia and adjacent oceans," *Environmental Science & Technology*, vol. 56, no. 10, pp. 6243–6252, 2022.

[28] D. Tatsii, S. Bucci, T. Bhowmick, J. Guettler, L. Bakels, G. Bagheri, and A. Stohl, "Shape matters: Long-range transport of microplastic fibers in the atmosphere," *Environmental Science & Technology*, vol. 58, no. 1, pp. 671–682, 2023.

[29] E. Ward, M. Gordon, R. Hanson, and L. M. Jantunen, "Modelling the effect of shape on atmospheric microplastic transport," *Atmospheric Environment*, p. 120458, 2024.

[30] S. Xiao, Y. Cui, J. Brahney, N. M. Mahowald, and Q. Li, "Long-distance atmospheric transport of microplastic fibres influenced by their shapes," *Nature Geoscience*, vol. 16, no. 10, pp. 863–870, 2023.

[31] G. Bagheri and C. Bonadonna, "On the drag of freely falling non-spherical particles," *Powder Technology*, vol. 301, pp. 526–544, 2016.

[32] L. Cai, J. Wang, J. Peng, Z. Tan, Z. Zhan, X. Tan, and Q. Chen, "Characteristic of microplastics in the atmospheric fallout from Dongguan city, China: Preliminary research and first evidence," *Environmental Science and Pollution Research*, vol. 24, no. 32, pp. 24928–24935, 2017.

[33] J. Gasperi, S. L. Wright, R. Dris, F. Collard, C. Mandin, M. Guerrouache, V. Langlois, F. J. Kelly, and B. Tassin, "Microplastics in air: Are we breathing it in?," *Current Opinion in Environmental Science & Health*, vol. 1, pp. 1–5, 2018.

[34] K. Bourzac, "Scientists race to study microplastic pollution in the atmosphere," *Chemical and Engineering News*, vol. 100, no. 7, 2022.

[35] T. H. Nguyen, T.-C. Kieu-Le, F. H. Tang, and F. Maggi, "Controlling factors of microplastic fibre settling through a water column," *Science of the Total Environment*, p. 156011, 2022.

[36] X. Rong, D. Qi, G. He, J. Zhu, and T. Scott, "Single curved fiber sedimentation under gravity," *Computers & Mathematics with Applications*, vol. 55, no. 7, pp. 1560–1567, 2008.

[37] X. Yang, Y. Wang, Y. Li, Y. Cao, Y. Zhou, and Y. Huang, "Experimental research on the settling property of slender fiber particles under the influence of multiple factors," *Powder Technology*, vol. 405, p. 117543, 2022.

[38] X. Song, Z. Xu, G. Li, Z. Pang, and Z. Zhu, "A new model for predicting drag coefficient and settling velocity of spherical and non-spherical particle in Newtonian fluid," *Powder Technology*, vol. 321, pp. 242–250, 2017.

[39] J. Zhang and C. E. Choi, "Improved settling velocity for microplastic fibers: A new shape-dependent drag model," *Environmental Science and Technology*, vol. 56, pp. 962–973, Jan. 2022.

[40] G. Ganser, "A rational approach to drag prediction of spherical and nonspherical particles," *Powder Technology*, vol. 77, no. 2, pp. 143–152, 1993.

[41] M. Kharrouba, J.-L. Pierson, and J. Magnaudet, "Flow structure and loads over inclined cylindrical rodlike particles and fibers," *Physical Review Fluids*, vol. 6, no. 4, p. 044308, 2021.

[42] K. D. Goral, H. Guler, B. E. Larsen, S. Carstensen, E. D. Christensen, N. B. Kerpen, T. Schlurmann, and D. R. Fuhrman, "Settling velocity of microplastic particles having regular and irregular shapes," *Environmental Research*, vol. 228, p. 115783, 2023.

[43] U. Makanga, M. Sepahi, C. Duprat, and B. Delmotte, "Obstacle-induced lateral dispersion and nontrivial trapping of flexible fibers settling in a viscous fluid," *Physical Review Fluids*, vol. 8, no. 4, p. 044303, 2023.

[44] D. Martinez, K. Buckley, S. Jivan, A. Lindstrom, R. Thiruvengadaswamy, J. Olson, T. Ruth, and R. Kerekes, "Characterizing the mobility of papermaking fibres during sedimentation," in *The Science of Papermaking: Transactions of the 12th Fundamental Research Symposium, Oxford. The Pulp and Paper Fundamental Research Society, Bury, UK*, pp. 225–254, 2001.

[45] A. R. Prajapati, H. K. Dave, and H. K. Raval, "Effect of fiber volume fraction on the impact strength of fiber reinforced polymer composites made by FDM process," *Materials Today: Proceedings*, vol. 44, pp. 2102–2106, 2021.

[46] T. Jirout and D. Jiroutová, "Hindered settling of fiber particles in viscous fluids," *Processes*, vol. 10, no. 9, p. 1701, 2022.

[47] B. Chan and K. Leong, "Scaffolding in tissue engineering: General approaches and tissue-specific considerations," *European Spine Journal*, vol. 17, pp. 467–479, 2008.

[48] S. Farhaj, B. R. Conway, and M. U. Ghori, "Nanofibres in drug delivery applications," *Fibers*, vol. 11, no. 2, p. 21, 2023.

[49] D. V. Daramsing, "Settling velocity of straight and curved rods at low Reynolds numbers in a quiescent fluid," 2023.

[50] A. Hamidi, D. Daramsing, M. D. Gordon, L. M. Jantunen, and R. E. Hanson, "Straight and curved cylindrical rods settling in quiescent fluid with application to atmospheric microplastics," *Experiments in Fluids*, vol. 65, no. 6, p. 81, 2024.

[51] A. Hamidi, M. D. Gordon, L. M. Jantunen, and R. E. Hanson, "Settling of u-shaped rods at low reynolds numbers," *Physics of Fluids*, vol. 37, no. 7, 2025.

[52] A. Hamidi, D. Daramsing, M. D. Gordon, L. M. Jantunen, and R. E. Hanson, "Terminal settling velocity of cylindrical rods of various shapes," *Journal of Fluid Flow, Heat and Mass Transfer (JFFHMT)*, vol. 11, no. 1, pp. 240–247, 2024.

[53] M. Lehtiniemi, S. Hartikainen, P. Näkki, J. Engström-Öst, A. Koistinen, and O. Setälä, "Size matters more than shape: Ingestion of primary and secondary microplastics by small predators," *Food Webs*, vol. 17, p. e00097, 2018.

[54] N. Laskar and U. Kumar, "Plastics and microplastics: A threat to environment," *Environmental Technology & Innovation*, vol. 14, p. 100352, 2019.

[55] L. An, Q. Liu, Y. Deng, W. Wu, Y. Gao, and W. Ling, "Sources of microplastic in the environment," *Microplastics in Terrestrial Environments: Emerging Contaminants and Major Challenges*, pp. 143–159, 2020.

[56] J. Brahney, M. Hallerud, E. Heim, M. Hahnenberger, and S. Sukumaran, "Plastic rain in protected areas of the United States," *Science*, vol. 368, no. 6496, pp. 1257–1260, 2020.

[57] N. Jones, "Microplastics are filling the skies. Will they affect the climate?," *Yale Environment 360*, 2023.

[58] S. Acharya, S. S. Rumi, Y. Hu, and N. Abidi, "Microfibers from synthetic textiles as a major source of microplastics in the environment: A review," *Textile Research Journal*, vol. 91, no. 17-18, pp. 2136–2156, 2021.

[59] C. Wang, J. Song, L. M. Nunes, H. Zhao, P. Wang, Z. Liang, H. P. H. Arp, G. Li, and B. Xing, "Global microplastic fiber pollution from domestic laundry," *Journal of Hazardous Materials*, vol. 477, p. 135290, 2024.

[60] A. P. A. López, J. Trilleras, V. A. Arana, L. S. Garcia-Alzate, and C. D. Grande-Tovar, "Atmospheric microplastics: exposure, toxicity, and detrimental health effects," *RSC Advances*, vol. 13, no. 11, pp. 7468–7489, 2023.

[61] Y. Geng, Z. Zhang, W. Zhou, X. Shao, Z. Li, and Y. Zhou, "Individual exposure to microplastics through the inhalation route: Comparison of microplastics in inhaled indoor aerosol and exhaled breath air," *Environmental Science & Technology Letters*, vol. 10, no. 6, pp. 464–470, 2023.

[62] G. Cao and Z. Cai, "Getting health hazards of inhaled nano/microplastics into focus: Expectations and challenges," *Environmental Science & Technology*, vol. 57, no. 9, pp. 3461–3463, 2023.

[63] B. Rosso, F. Scoto, I. G. Hallanger, C. Larose, J. C. Gallet, A. Spolaor, B. Bravo, C. Barbante, A. Gambaro, and F. Corami, "Characteristics and quantification of small microplastics (< 100 μm) in seasonal Svalbard snow on glaciers and lands," *Journal of Hazardous Materials*, p. 133723, 2024.

[64] A. Talukdar, S. Bhattacharya, A. Bandyopadhyay, and A. Dey, "Microplastic pollution in the Himalayas: Occurrence, distribution, accumulation and environmental impacts," *Science of the Total Environment*, vol. 874, p. 162495, 2023.

[65] Y. Zhang, T. Gao, S. Kang, H. Shi, L. Mai, D. Allen, and S. Allen, "Current status and future perspectives of microplastic pollution in typical cryospheric regions," *Earth-Science Reviews*, vol. 226, p. 103924, 2022.

[66] X. Ren, J. Tang, X. Liu, and Q. Liu, "Effects of microplastics on greenhouse gas emissions and the microbial community in fertilized soil," *Environmental Pollution*, vol. 256, p. 113347, 2020.

[67] E. Hood, T. J. Battin, J. Fellman, S. O'neel, and R. G. Spencer, "Storage and release of organic carbon from glaciers and ice sheets," *Nature Geoscience*, vol. 8, no. 2, pp. 91–96, 2015.

[68] C. S. Zender, H. Bian, and D. Newman, "Mineral dust entrainment and deposition (dead) model: Description and 1990s dust climatology," *Journal of Geophysical Research: Atmospheres*, vol. 108, no. D14, 2003.

[69] A. R. Henn, "Calculation of the stokes and aerodynamic equivalent diameters of a short reinforcing fiber," *Particle & Particle Systems Characterization*, vol. 13, no. 4, pp. 249–253, 1996.

[70] M. Martina and S. T. Castelli, "Modelling the potential long-range dispersion of atmospheric microplastics reaching a remote site," *Atmospheric Environment*, vol. 312, p. 120044, 2023.

[71] M. Trainic, J. M. Flores, I. Pinkas, M. L. Pedrotti, F. Lombard, G. Bourdin, G. Gorsky, E. Boss, Y. Rudich, A. Vardi, *et al.*, "Airborne microplastic particles detected in the remote marine atmosphere," *Communications Earth & Environment*, vol. 1, no. 1, p. 64, 2020.

[72] A. S. W. Reininger, D. Tatsii, T. Bhowmick, G. Bagheri, and A. Stohl, "The atmospheric settling of commercially sold microplastics," *EGUsphere*, vol. 2025, pp. 1–17, 2025.

[73] R. Dris, J. Gasperi, V. Rocher, M. Saad, N. Renault, and B. Tassin, "Microplastic contamination in an urban area: A case study in Greater Paris," *Environmental Chemistry*, vol. 12, no. 5, pp. 592–599, 2015.

[74] Z. Qian, T. ChongGuo, and L. YongMing, "Various forms and deposition fluxes of microplastics identified in the coastal urban atmosphere," *Chinese Science Bulletin*, vol. 62, no. 33, pp. 3902–3909, 2017.

[75] K. Liu, X. Wang, T. Fang, P. Xu, L. Zhu, and D. Li, "Source and potential risk assessment of suspended atmospheric microplastics in Shanghai," *Science of the Total Environment*, vol. 675, pp. 462–471, 2019.

[76] S. Abbasi, B. Keshavarzi, F. Moore, A. Turner, F. J. Kelly, A. O. Dominguez, and N. Jaafarzadeh, "Distribution and potential health impacts of microplastics and microrubbers in air and street dusts from Asaluyeh County, Iran," *Environmental Pollution*, vol. 244, pp. 153–164, 2019.

[77] T. Stanton, M. Johnson, P. Nathanail, W. MacNaughtan, and R. L. Gomes, "Freshwater and airborne textile fibre populations are dominated by 'natural', not microplastic, fibres," *Science of the Total Environment*, vol. 666, pp. 377–389, 2019.

[78] M. Klein and E. K. Fischer, "Microplastic abundance in atmospheric deposition within the Metropolitan area of Hamburg, Germany," *Science of the Total Environment*, vol. 685, pp. 96–103, 2019.

[79] Y. Huang, T. He, M. Yan, L. Yang, H. Gong, W. Wang, X. Qing, and J. Wang, "Atmospheric transport and deposition of microplastics in a subtropical urban environment," *Journal of Hazardous Materials*, vol. 416, p. 126168, 2021.

[80] H. Dong, L. Wang, X. Wang, L. Xu, M. Chen, P. Gong, and C. Wang, "Microplastics in a remote lake basin of the Tibetan Plateau: Impacts of atmospheric transport and glacial melting," *Environmental Science & Technology*, vol. 55, no. 19, pp. 12951–12960, 2021.

[81] B. Welsh, J. Aherne, A. M. Paterson, H. Yao, and C. McConnell, "Atmospheric deposition of anthropogenic particles and microplastics in south-central Ontario, Canada," *Science of the Total Environment*, vol. 835, p. 155426, 2022.

[82] V. Shruti, G. Kutralam-Muniasamy, F. Pérez-Guevara, P. D. Roy, and I. E. Martínez, "Occurrence and characteristics of atmospheric microplastics in Mexico City," *Science of the Total Environment*, vol. 847, p. 157601, 2022.

[83] S. Abbasi, N. Jaafarzadeh, A. Zahedi, M. Ravanbakhsh, S. Abbaszadeh, and A. Turner, "Microplastics in the atmosphere of Ahvaz City, Iran," *Journal of Environmental Sciences*, vol. 126, pp. 95–102, 2023.

[84] S. Kernchen, H. Schmalz, M. G. Löder, C. Georgi, A. Einhorn, A. Greiner, A. C. Nölscher, C. Laforsch, and A. Held, "Atmospheric deposition studies of microplastics in Central Germany," *Air Quality, Atmosphere & Health*, pp. 1–15, 2024.

[85] X. Wang, Z. Ouyang, Y. He, L. Ding, X. Liang, and X. Guo, "An important source of terrestrial microplastics-atmospheric deposition: A microplastics survey based on Shaanxi, China," *Land Degradation & Development*, vol. 35, no. 9, pp. 3191–3199, 2024.

[86] H. Kalman and E. Matana, "Terminal velocity and drag coefficient for spherical particles," *Powder Technology*, vol. 396, pp. 181–190, 2022.

[87] G. Stokes, "On the effect of the internal friction of fluids on the motion of pendulums," *Transaction of the Cambridge Philosophical Society*, vol. 9, pp. 8–106, 1851.

[88] R. Clift, J. R. Grace, and M. E. Weber, *Bubbles, Drops and Particles*. Academic Press, New York, 1978.

[89] N. Cheng, "Comparison of formulas for drag coefficient and settling velocity of spherical particles," *Powder Technology*, vol. 189, no. 3, pp. 395–398, 2009.

[90] M. Hartman, V. Havlin, O. Trnka, and M. C˘árskỳ, "Predicting the free-fall velocities of spheres," *Chemical Engineering Science*, vol. 44, no. 8, pp. 1743–1745, 1989.

[91] A. Terfous, A. Hazzab, and A. Ghenaim, "Predicting the drag coefficient and settling velocity of spherical particles," *Powder Technology*, vol. 239, pp. 12–20, 2013.

[92] R. Barati, S. A. A. S. Neyshabouri, and G. Ahmadi, "Development of empirical models with high accuracy for estimation of drag coefficient of flow around a smooth sphere: An evolutionary approach," *Powder Technology*, vol. 257, pp. 11–19, 2014.

[93] S. Dey, S. Z. Ali, and E. Padhi, "Terminal fall velocity: The legacy of Stokes from the perspective of fluvial hydraulics," *Proceedings of the Royal Society A*, vol. 475, no. 2228, p. 20190277, 2019.

[94] E. E. Michaelides and Z. Feng, "Review - Drag coefficients of non-spherical and irregularly shaped particles," *Journal of Fluids Engineering*, vol. 145, p. 060801, 03 2023.

[95] Z. Yu, G. Yang, and W. Zhang, "A new model for the terminal settling velocity of microplastics," *Marine Pollution Bulletin*, vol. 176, p. 113449, 2022.

[96] X. Cheng, Z. Cao, J. Li, and A. Borthwick, "A numerical study of the settling of non-spherical particles in quiescent water," *Physics of Fluids*, vol. 35, no. 9, 2023.

[97] H. Kalman and D. Portnikov, "Free falling of non-spherical particles in Newtonian fluids, A: Terminal velocity and drag coefficient," *Powder Technology*, vol. 434, p. 119357, 2024.

[98] S. Qian, X. Qiao, W. Zhang, Z. Yu, S. Dong, and J. Feng, "Machine learning-based prediction for settling velocity of microplastics with various shapes," *Water Research*, vol. 249, p. 121001, 2024.

[99] K. Jayaweera and B. Mason, "The behaviour of freely falling cylinders and cones in a viscous fluid," *Journal of Fluid Mechanics*, vol. 22, no. 4, pp. 709–720, 1965.

[100] R. Khayat and R. Cox, "Inertia effects on the motion of long slender bodies," *Journal of Fluid Mechanics*, vol. 209, pp. 435–462, 1989.

[101] J. S. McNown and J. Malaika, "Effects of particle shape on settling velocity at low Reynolds numbers," *Eos, Transactions American Geophysical Union*, vol. 31, no. 1, pp. 74–82, 1950.

[102] D. Lopez and E. Guazzelli, "Inertial effects on fibers settling in a vortical flow," *Physical Review Fluids*, vol. 2, no. 2, p. 024306, 2017.

[103] A. Khalili and B. Liu, "Stokes' paradox: Creeping flow past a two-dimensional cylinder in an infinite domain," *Journal of Fluid Mechanics*, vol. 817, pp. 374–387, 2017.

[104] B. Huner and R. Hussey, "Cylinder drag at low Reynolds number," *The Physics of Fluids*, vol. 20, no. 8, pp. 1211–1218, 1977.

[105] S. Sen, S. Mittal, and G. Biswas, "Steady separated flow past a circular cylinder at low Reynolds numbers," *Journal of Fluid Mechanics*, vol. 620, pp. 89–119, 2009.

[106] S. Dehghani, F. Moore, and R. Akhbarizadeh, "Microplastic pollution in deposited urban dust, Tehran metropolis, Iran," *Environmental Science and Pollution Research*, vol. 24, no. 25, pp. 20360–20371, 2017.

[107] R. Cox, "The motion of long slender bodies in a viscous fluid Part 1. General theory," *Journal of Fluid Mechanics*, vol. 44, no. 4, pp. 791–810, 1970.

[108] A. Chow and E. Adams, "Prediction of drag coefficient and secondary motion of free-falling rigid cylindrical particles with and without curvature at moderate Reynolds number," *Journal of Hydraulic Engineering*, vol. 137, no. 11, pp. 1406–1414, 2011.

[109] T. Huang, H. Zhao, S. Peng, J. Li, Y. Yao, and P. Yu, "A numerical study on free-fall of a torus with initial inclination angle at low Reynolds numbers," *Journal of Fluids and Structures*, vol. 107, p. 103389, 2021.

[110] F. Candelier, K. Gustavsson, P. Sharma, L. Sundberg, A. Pumir, G. Bagheri, and B. Mehlig, "Torques on curved atmospheric fibres," *arXiv preprint arXiv:2409.19004*, 2024.

[111] O. Du Roure, A. Lindner, E. N. Nazockdast, and M. J. Shelley, "Dynamics of flexible fibers in viscous flows and fluids," *Annual Review of Fluid Mechanics*, vol. 51, pp. 539–572, 2019.

[112] B. Marchetti, V. Raspa, A. Lindner, O. Du Roure, L. Bergougnoux, É. Guazzelli, and C. Duprat, "Deformation of a flexible fiber settling in a quiescent viscous fluid," *Physical Review Fluids*, vol. 3, no. 10, p. 104102, 2018.

[113] L. Li, H. Manikantan, D. Saintillan, and S. E. Spagnolie, "The sedimentation of flexible filaments," *Journal of Fluid Mechanics*, vol. 735, pp. 705–736, 2013.

[114] O. Du Roure, A. Lindner, E. N. Nazockdast, and M. J. Shelley, "Dynamics of flexible fibers in viscous flows and fluids," *Annual Review of Fluid Mechanics*, vol. 51, pp. 539–572, 2019.

[115] B. Delmotte, E. Climent, and F. Plouraboué, "A general formulation of bead models applied to flexible fibers and active filaments at low Reynolds number," *Journal of Computational Physics*, vol. 286, pp. 14–37, 2015.

[116] C. Dai, F. Yuan, D. Wang, X. Yang, J. Du, W. Yu, and C. Zhang, "Settling velocity of submillimeter microplastic fibers in still water," *Science of the Total Environment*, vol. 907, p. 168054, 2024.

[117] A. Roy, R. Hamati, L. Tierney, D. Koch, and G. Voth, "Inertial torques and a symmetry breaking orientational transition in the sedimentation of slender fibres," *Journal of Fluid Mechanics*, vol. 875, pp. 576–596, 2019.

[118] X. Jiang, C. Xu, and L. Zhao, "Settling and collision of spheroidal particles with an offset mass centre in a quiescent fluid," *Journal of Fluid Mechanics*, vol. 984, p. A40, 2024.

[119] B. R. Angle, M. J. Rau, and M. L. Byron, "Effect of mass distribution on falling cylindrical particles at intermediate Reynolds numbers," in *Fluids Engineering Division Summer Meeting*, vol. 59087, p. V005T05A065, American Society of Mechanical Engineers, 2019.

[120] S. Yasseri, "Experiment of free-falling cylinders in water," *Underwater Technology*, vol. 32, no. 3, pp. 177–191, 2014.

[121] F. Candelier and B. Mehlig, "Settling of an asymmetric dumbbell in a quiescent fluid," *Journal of Fluid Mechanics*, vol. 802, pp. 174–185, 2016.

[122] B. R. Angle, M. J. Rau, and M. L. Byron, "Settling of nonuniform cylinders at intermediate Reynolds numbers," *Physical Review Fluids*, vol. 9, no. 7, p. 070501, 2024.

[123] J.-L. Pierson, "Inertial settling of an arbitrarily oriented cylinder in a quiescent flow: From short-time to quasisteady motion," *Physical Review Fluids*, vol. 8, no. 10, p. 104301, 2023.

[124] P. Kry and R. List, "Aerodynamic torques on rotating oblate spheroids," *The Physics of Fluids*, vol. 17, no. 6, pp. 1087–1092, 1974.

[125] F. Candelier, J. Qiu, L. Zhao, G. Voth, and B. Mehlig, "Inertial torque on a squirmer," *Journal of Fluid Mechanics*, vol. 953, p. R1, 2022.

[126] R. Cox, "The steady motion of a particle of arbitrary shape at small Reynolds numbers," *Journal of Fluid Mechanics*, vol. 23, no. 4, pp. 625–643, 1965.

[127] J.-L. Pierson, M. Kharrouba, and J. Magnaudet, "Hydrodynamic torque on a slender cylinder rotating perpendicularly to its symmetry axis," *Physical Review Fluids*, vol. 6, no. 9, p. 094303, 2021.

[128] F. Cabrera, M. Sheikh, B. Mehlig, N. Plihon, M. Bourgoin, A. Pumir, and A. Naso, "Experimental validation of fluid inertia models for a cylinder settling in a quiescent flow," *Physical Review Fluids*, vol. 7, no. 2, p. 024301, 2022.

[129] A. Roy, S. Kramel, U. Menon, G. A. Voth, and D. L. Koch, "Orientation of finite Reynolds number anisotropic particles settling in turbulence," *Journal of Non-Newtonian Fluid Mechanics*, vol. 318, p. 105048, 2023.

[130] N.-S. Cheng, "Formula for the viscosity of a glycerol- water mixture," *Industrial & Engineering Chemistry Research*, vol. 47, no. 9, pp. 3285–3288, 2008.

[131] S. M. Soloff, R. J. Adrian, and Z.-C. Liu, "Distortion compensation for generalized stereoscopic particle image velocimetry," *Measurement Science and Technology*, vol. 8, pp. 1441–1454, dec 1997.

[132] B. Wieneke, "Volume self-calibration for 3D particle image velocimetry," *Experiments in Fluids*, vol. 45, no. 4, pp. 549–556, 2008.

[133] A. K. Prasad, "Stereoscopic particle image velocimetry," *Experiments in Fluids*, vol. 29, no. 2, pp. 103–116, 2000.

[134] H. Brenner, "Effect of finite boundaries on the Stokes resistance of an arbitrary particle," *Journal of Fluid Mechanics*, vol. 12, no. 1, pp. 35–48, 1962.

[135] J. R. Taylor, *An Introduction to Error Analysis: The Study of Uncertainties in Physical Measurements*. University Science Books, 2 sub ed., 1996.

[136] A. Hamidi, M. Oshaghi, H. Afshin, and B. Firoozabadi, "Experimental investigation of various regimes of bubble formation and growth - A theoretical view of double coalescence regime," *Journal of Fluids Engineering*, vol. 142, no. 4, p. 041403, 2020.

[137] X. Xu and A. Nadim, "Deformation and orientation of an elastic slender body sedimenting in a viscous liquid," *Physics of Fluids*, vol. 6, no. 9, pp. 2889–2893, 1994.

[138] N. Fintzi, L. Gamet, and J.-L. Pierson, "Inertial loads on a finite-length cylinder embedded in a steady uniform flow," *Physical Review Fluids*, vol. 8, no. 4, p. 044302, 2023.

[139] A. Haider and O. Levenspiel, "Drag coefficient and terminal velocity of spherical and nonspherical particles," *Powder Technology*, vol. 58, no. 1, pp. 63–70, 1989.

[140] F. Yuan, C. Dai, Y. Ying, D. Wang, X. Yang, J. Du, and W. Yu, "Prediction of the settlement of submillimeter microplastic fibers in still water," *Environmental Technology & Innovation*, vol. 37, p. 103951, 2025.

[141] S. Mittal and B. Kumar, "Flow past a rotating cylinder," *Journal of Fluid Mechanics*, vol. 476, pp. 303–334, 2003.

[142] J. Jiménez-Varona, "Numerical analysis of the magnus effect on the forces past an axisymmetric body at high incidence," *Aerospace*, vol. 10, no. 2, p. 163, 2023.

[143] J. R. Garratt, "The atmospheric boundary layer," *Earth-Science Reviews*, vol. 37, no. 1-2, pp. 89–134, 1994.